Grain Boundary Structure and Element Transport Processes Studied at the nm-Scale Using Transmission Electron Microscopy (TEM)

vorgelegt von

Dipl. Min. Katharina Marquardt (neé Hartmann)

aus Berlin

Von der Fakultät VI - Planen Bauen Umwelt - der

Technischen Universität Berlin

zur Erlangung des akademischen Grades

Doktor der Naturwissenschaften

Dr. rer. nat.

genehmigte Dissertation

Promotionsausschuss:

Vorsitzender: Prof. Dr. rer. nat. Gerhard Franz

Gutachter: Prof. Dr. rer. nat. Wilhelm Heinrich

Gutachter: Prof. Dr. rer. nat. Hans-Joachim Kleebe

Gutachter: Dr. rer. nat. Richard Wirth

Tag der wissenschaftlichen Aussprache: 19.07.2010

Berlin 2010

D 83

Contents

Summary

Grain boundaries cause markedly differing physical and chemical properties of polycrystalline materials in comparison to their constitutive single crystals. The understanding of grain boundary related processes and their relation to the grain boundaries' structural properties is a key challenge in various scientific disciplines, including geosciences, materials science, and chemistry. The quantification of element diffusion rates along grain boundaries is of particular interest, because it is often several orders of magnitude faster than its counterpart through the grain's volume and thus governs a number of physico-chemical processes.

Despite the pivotal role of grain boundaries, today's knowledge on grain boundary structure and its relation to numerous phenomena, including grain boundary diffusion, is only fragmentary. This work aims to provide a feasible and consistent approach to study the relation between structure and element diffusion in both the grain's volume and along well characterised single grain boundaries on the nm-scale.

In chapter 1.1, I provide a general introduction to the structure and properties of grain boundaries, I mention the commonly used geometrical model to describe grain boundaries, and I briefly introduce standard methods to synthesize grain boundaries. Chapter 1.2 treats some general aspects of element diffusion and introduces the most common analytical solutions to the diffusion equation, which are used to derive diffusion coefficients from laboratory experiments. This section ends with an overview of standard approaches to experimentally derive diffusion data.

The main results of my thesis are summarized and discussed in chapter 2, whereas chapter 3 contains the complete manuscripts, which emerged from my thesis.

In the first part of chapter 2 (2.1), I show that the wafer direct bonding method is ideally suited to synthesize well defined synthetic grain boundaries in yttrium aluminium garnet. I find that annealing temperatures higher than 60% of the melting temperature are needed to obtain a grain boundary with maximum stability. I thoroughly characterize the synthesized grain boundaries and discuss the influence of slight misorientations with regard to a perfect $\Sigma 5$ grain boundary on the grain boundary structure.

The second project of my thesis (chapter 2.2) aimed at showing that thin-film diffusion experiments can be coupled with transmission electron microscopy (TEM) as

the analytical tool to quantify diffusion rates in yttrium aluminium garnet. I evaluate the influence of crystallisation of the initially amorphous thin-film, the diffusant source, on the applicability of a commonly used analytical solution to the diffusion equation. A numerical model is developed to extract the diffusion coefficent that accounts for the observed time-dependent structural properties of the thin-film. I show that characterization of the diffusant source is of major importance to determine the volume diffusion coefficient, because the behaviour of the diffusant source defines the boundary conditions that need to be implemented in the modelling/fitting of the diffusion profile. I compare the results of this new approach to measurements that I performed using Rutherford Backscattering, which is an established technique to acquire diffusion profiles.

In the following section (chapter 2.3), I performed grain boundary diffusion experiments on the synthetic grain boundary, which I characterized in chapter 2.1, by using the same experimental procedures and analytical tools that I explored in the volume diffusion study (chapter 2.2). I show that this innovative combination of miniaturized experiments and small-scale analysis is outstandingly well suited to study both volume and grain boundary diffusion on the same sample. In addition, TEM provides valuable information on the time-dependent properties of the diffusant source and the grain boundary structure. These additional informations were used to tailor a numerical model that adequately describes our experimental setting.

Finally (chapter 2.4), I performed a TEM study at atomic resolution to directly determine and characterize the *effective* grain boundary width for diffusion, which is a key parameter in several equations describing diffusional or rheological processes. I used high resolution TEM focal series, in combination with multislice and chemically-sensitive Z-imaging, to image the narrow zone of enhanced Yb diffusion along the grain boundary. I conclude that these techniques are indeed capable to monitor the *effective* grain boundary width and find that it to be about 40 times larger than commonly assumed. This is a big step ahead towards a quantitative understanding of diffusion processes on the nanometer scale.

The four parts of my thesis show that the combination of bicrystal synthesis by

direct wafer bonding, thin-film production by pulsed laser deposition, and analysis with different TEM modes is exceptionally well suited to study both volume and grain boundary diffusion on the atomic scale and draw important conclusions about their relation to the material's structure. In future studies, this innovative approach can be applied to other materials, both in Earth sciences and materials' research.

At the end of my thesis (chapter 4), I discuss a promising innovative way to study crack healing processes, which is based on the findings of this thesis.

Zusammenfassung

Die chemisch-physikalischen Eigenschaften von polykristallinen Materialien unterscheiden sich deutlich von den Eigenschaften der Einkristalle, durch die sie aufgebaut sind; die Ursache sind Korngrenzen. Eine zentrale Herausforderung verschiedener wissenschaftlicher Disziplinen, darunter Chemie, Geo- und Materialwissenschaften, ist es, korngrenzbeeinflusste Prozesse und deren Zusammenhang mit den strukturellen Eigenschaften der Korngrenze zu verstehen. Die quantitative Bestimmung von Korngrenzdiffusion ist von besonderem Interesse, da sie um Größenordnungen schneller ist als ihr Gegenpart im Kristallvolumen und sie somit viele chemisch-physikalische Prozesse kontrolliert.

Trotz der zentralen Bedeutung von Korngrenzen ist unser heutiges Wissen über das Zusammenspiel von Korngrenzstruktur und Korngrenzphänomenen, einschließlich Korngrenzdiffusion, nur oberflächlich. Die hier präsentierte Arbeit stellt einen konsistenten Ansatz vor, der die Untersuchung des Zusammenhangs von Struktur und Diffusion, sowohl im Kristallvolumen, als auch in Korngrenzen, auf der nm-Ebene ermöglicht.

In Kapitel 1.1 gebe ich eine generelle Einführung in die Struktur und Eigenschaften von Korngrenzen. Ich diskutiere das allgemein gebräuchlichste Modell zur geometrischen Beschreibung von Korngrenzen und stelle die gängigsten Methoden zur Korngrenzsynthese vor. Kapitel 1.2 behandelt einige wichtige Aspekte der Elementdiffusion. Die gängigsten analytischen Lösungen der Diffusionsgleichung, die gewöhnlich zur Bestimmung von Diffusionskoeffizienten aus Laborexperimenten genutzt werden, werden vorgestellt. Ein Überblick über Standardverfahren, um Diffusionsdaten mit Laborexperimenten zu gewinnen, wird am Ende des Kapitels gegeben.

Die zentralen Ergebnisse meiner Arbeit sind in Kapitel 2 zusammengefasst. Die kompletten Manuskripte, die aus meiner Arbeit entstanden sind, enthält das Kapitel 3.

In meiner ersten Veröffentlichung (Kapitel 2.1) zeige ich, dass die 'wafer direct bonding'-Methode hervorragend zur Synthese definierter Korngrenzen in Yttrium-Aluminium-Granat geeignet ist. Eine Temperaturbehandlung bei mehr als 60% der Schmelztemperatur ist Voraussetzung, um Korngrenzen mit maximaler Stabilität zu erzeugen. Die synthetischen Korngrenzen habe ich anschließend genauestens cha-

rakterisiert. Der Einfluss kleiner Orientierungsabweichungen von einer perfekten $\Sigma 5$ Korngrenzorientierung auf die Korngrenzstruktur wird diskutiert.

Das Ziel des zweiten Projekts meiner Arbeit (Kapitel 2.2) ist es zu zeigen, dass Diffusionsexperimente in Dünnschichtgeometrie mit Transmissionselektronenmikroskopie (TEM) geeignet analysiert, und so Diffusionsraten in Yttrium-Aluminium-Granat quantifiziert werden können. Ich evaluiere mögliche Einflüsse der Kristallisation der ursprünglich amorphen Dünnschicht, der Diffusionsquelle, auf die Anwendbarkeit einer gewöhnlich verwendeten analytischen Lösung der Diffusionsgleichung. Ein numerisches Modell, welches die beobachteten zeitabhängigen Eigenschaftsänderungen der Diffusionsquelle berücksichtigt, wurde entwickelt und zur Bestimmung des Diffusionskoeffizienten verwendet. Die Eigenschaften der Diffusionsquelle definieren die Randbedingungen, die in der Auswertung/Modellierung der Diffusionsprofile berücksichtigt werden müssen. Daher ist die gewissenhafte Charakterisierung der Diffusionsquelle von großer Bedeutung. Die Resultate dieser neuen Vorgehensweise vergleiche ich mit Messdaten, die ich mit Rutherford-Rückstreuung, einer etablierten Technik zur Messung von Diffusionsprofilen, ermittelt habe.

Zur Durchführung der im folgenden Abschnitt (Kapitel 2.3) vorgestellten Kornzgrenzdiffusionsexperimente, verwendete ich die synthetische Korngrenze, welche ich zuvor charakterisiert habe (Kapitel 2.1). Ich habe dieselbe Versuchsdurchführung und die gleichen analytischen Methoden verwendet, die ich in der Volumendiffusionsstudie erkundet habe (Kapitel 2.2). Ich zeige, dass die innovative Kombination miniaturisierter Experimente und kleinmaßstäblicher Analyse hervorragend geeignet ist, um sowohl Volumen- als auch Korngrenzdiffusion an derselben Probe zu untersuchen. Wertvolle Informationen über die zeitabhängigen Eigenschaften der Diffusionsquelle und der Korngrenzstruktur können durch TEM gewonnen werden. Das numerische Modell aus Kapitel 2.2 wurde auf Grundlage der zusätzlichen Informationen weiterentwickelt, und die experimentellen Gegebenheiten und Beobachtungen werden angemessen und zweidimensional beschrieben.

Um die *effektive* Korngrenzweite für Diffusion direkt zu bestimmen und zu charakterisieren, habe ich schließlich (Kapitel 2.4) eine TEM-Studie bei atomarer Auflösung durchgeführt. Die *effektive* Korngrenzweite ist ein wichtiger Parameter in

vielen Gleichungen zur Beschreibung diffusiver und rheologischer Prozesse. Fokusserien, aufgenommen mit hochauflösender TEM, wurden zur Phasenrekonstruktion verwendet. Sie wurden mit Z-sensitiver Raster-TEM, bei der die Signalintensität mit der Ordnungszahl korreliert, kombiniert, um den schmalen Bereich mit erhöhter Yb-Diffusion entlang der Korngrenze abzubilden. Die verwendeten Techniken ermöglichen es tatsächlich, die *effektive* Korngrenzweite sichtbar zu machen. Meine Ergebnisse zeigen, dass sie etwa 40 mal so breit ist, wie gewöhnlich angenommen. Dies ist ein großer Schritt in Richtung eines quantitativen Verständnisses von Diffusionsprozessen auf der Nanometer-Skala.

Die vier Teile meiner Arbeit bauen strikt aufeinander auf und zeigen, dass die Kombination aus Bikristallsynthese mit der 'direct wafer bonding'-Methode, Dünnschichtherstellung mit 'Pulsed Laser Deposition' und Analyse mit verschiedenen TEM Techniken außerordentlich gut geeignet ist, um sowohl Volumen- als auch Korngrenzdiffusion auf atomarer Ebene zu untersuchen. Wichtige Erkenntnisse über den Zusammenhang von Diffusion und Struktur des Materials können so erzielt werden. In zukünftigen Arbeiten kann die beschriebene Kombination, sowohl in den Geo- als auch in den Materialwissenschaften, auf andere Materialien angewendet werden.

Am Schluss dieser Arbeit (Kapitel 4) gebe ich einen Ausblick, wie Rissheilungsprozesse erfolgreich untersucht werden könnten. Die Idee basiert auf den Beobachtungen, die ich während meiner Arbeit machte.

Chapter 1

Introduction

1.1 Grain Boundaries

The physical and chemical behaviour of polycrystalline materials, including rocks and ceramics, often differ from those observed on single-crystals. Phase or grain boundaries, which form foam-like three-dimensional networks (Fig. 1.1), largely impact the materials' properties (Gleiter & Chalmers, 1972; Chadwick & Smith, 1976; Carter & Föll, 1978; Föll & Ast, 1979; Carter et al., 1981; Cunningham et al., 1982; Sutton & Balluffi, 1995; Christophersen et al., 2001; Merkle et al., 2004; Randle, Rohrer & Hu, 2008). Grain and phase boundaries exhibit different characteristics and the terms should be carefully distinguished. Phase boundaries connect two different minerals or minerals of different composition. In contrast, grain boundaries separate two mineral grains with the same structure and composition, but different crystallographic orientation. Grain as well as phase boundaries are interfaces; both can contain an interphase (Fig. 1.2). For the sake of simplicity, I will only use the term grain boundary in the following treatise, even though the majority of the declarations below hold for phase boundaries as well.

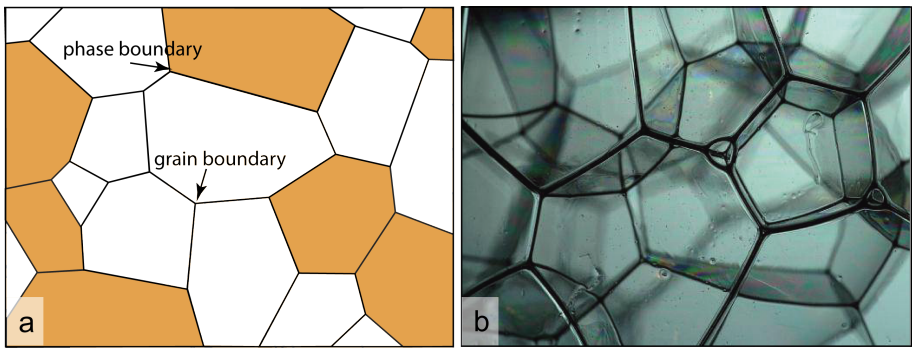

Figure 1.1: (a) Sketch of a structure close to equilibrium in a polycrystalline material, phase and grain boundaries are labeled. (b) The three-dimensional network in soap foam, which is built by the boundaries between bubbles, is comparable to the network found within rocks. The interfaces between individual bubbles are slightly curved and they are connected at triple junctions, where they form 120° angles with each other. The picture was kindly provided by B. Bossert.

1.1.1 Grain Boundary Structure

The study of grain boundaries is, unfortunately, hampered by the overwhelming variability of their appearances. They can be straight, stepped or facetted; some-

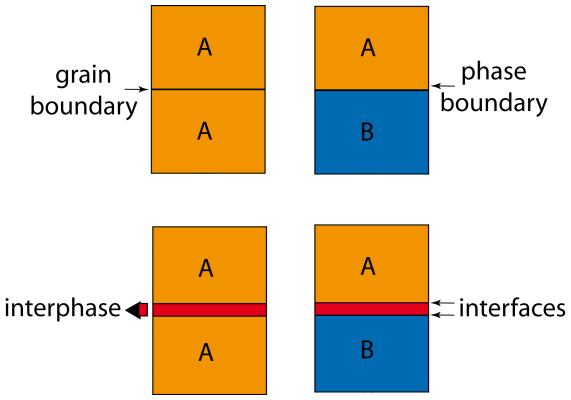

Figure 1.2: Schematic presentation of grain and phase boundaries. Grain boundaries separate two grains with distinct orientations, whereas phase boundaries separate two mineral grains with either different chemical composition or crystal structure. The interface of both boundary types might contain an interphase.

times even micrometer-wide zones are referred to as grain boundaries (Mistler & Coble, 1974; Fabris & Elsässer, 2001; Lartigue-Korinek et al., 2008; Sato et al., 2009). They may appear glassy, amorphous, fluid covered or crystalline (Sun & Balluffi, 1982; S. B. Lee et al., 2003; Lozovoi et al., 2006; Pennock et al., 2009). Accordingly, their properties vary widely as does their behavior under stress or at elevated temperatures, and physico-chemical processes, such as deformation or diffusion, are markedly influenced by the character of the grain boundaries involved (Haynes & Smoluchowski, 1955; Byerly & Vogel, 1973; Stöckhert & Duyster, 1999; Shan et al., 2004). This motivated many studies on the structure of grain boundaries, especially in the 1970ties. Nevertheless, investigations of the relation between grain boundary structure and its influence on the process of interest are still scarce and thus our understanding is humble (Mishin & Herzig, 1999). From a geoscientific point of view, our mostly qualitative knowledge is likewise annoying, because quantitative grain boundary diffusion data and their relation to structural properties are needed to understand several phenomena, including metamorphic and rheological processes. Grain boundaries are also omnipresent in our daily life, where they determine not only the performance of electronic devices or medical implants but also the reliability of car brakes and aircraft turbines, to name just a few examples. It is a fundamental challenge in material engineering to design polycrystalline materi-

als with desired properties, which requires a detailed knowledge of grain boundary structures and relies on a quantitative understanding of its influence on different processes, including element diffusion (Ikesue et al., 1995; Brown & Bonnell, 1998; Lu et al., 2002; Mah et al., 2004; C.-S. Kim et al., 2006; Randle, Hu & Coleman, 2008; D. Chen et al., 2009). The quantification of element diffusion rates along grain boundaries and their dependence on structure is a major goal of this thesis (chapters 3.1 and 3.3).

Commonly used methods only allow to derive a combination, either as product or as quotient, of the grain boundary diffusion coefficient and the *effective* grain boundary width δ for diffusion (e.g. Hondros, 1976). The *effective* grain boundary width includes the strained area resulting from misfit between the crystals plus the space-charge region (Lehovec, 1953; Kliewer & Koehler, 1965; Kingery, 1974) on either side in case of ionic materials. This results in a zone of enhanced diffusion parallel to the grain boundary (S. White, 1973). The *structural* (or physical) grain boundary width, in contrast, is the distance between two adjacent crystal lattices. Unfortunately, the *effective* grain boundary width can not be routinely measured. This adds considerable uncertainty to the derived diffusion coefficient in previous studies. This thesis aims at directly quantifying both element diffusion along a grain boundary (chapter 3.3) and the *effective* grain boundary width for diffusion (chapter 3.4).

I synthesized a specific grain boundary in yttrium aluminium garnet (YAG) using the direct wafer bonding method and investigated the resulting structure (chapter 3.1). This served as the fundament for successive grain boundary diffusion experiments along this grain boundary (chapter 3.3). A novel way to perform well defined diffusion experiments in miniaturized geometry and characterize diffusion at the nm-scale was explored and is discussed in the chapters 3.2 – 3.4. Furthermore, I examined experimentally how grain boundary diffusion chemically alters the lattice around the grain boundary and investigated its relation to strain (chapter 3.4).

1.1.2 Description of Grain Boundaries

Commonly, grain boundaries are divided in *general* (or *random*) grain boundaries and *special* grain boundaries (Chadwick & Smith, 1976; Balluffi & Sutton, 1996). *Special* grain boundaries exhibit a periodic structure, repeated every few nanometers, whereas *general* grain boundaries show no appearent periodicity. Their properties thus differ.

Grain boundary structure models have mostly been developed for metals, but they are largely applicable to oxides and silicates. The need for charge compensation along the grain boundary of oxides and silicates represents the main difference towards metals as illustrated in Fig. 1.3a (Lehovec, 1953; Kliewer & Koehler, 1965; Clarke & Wolf, 1986). The prevailing grain boundary structure models, which evolved over the last decades, are tightly interwoven and assume that specific grain boundary plane orientations with low energy configurations exist. Consequently, the interface tries to attain such a minimum energy configuration, if necessary by the introduction of additional defects (Chadwick & Smith, 1976). The structural rearrangement usually produces an excess free volume at the boundary and the physical and chemical properties of the grain-boundary are affected by the difference between the grain boundary structure and the crystal structure. The atoms in a grain boundary exhibit lower coordination numbers (Fig. 1.3b) and larger average bond lengths (e.g. Kaur et al., 1995; Heinemann et al., 2003). Interestingly, the strength of a grain boundary is similar to the one of a perfect single crystal lattice. This has been shown on different materials (e.g. Gleiter & Chalmers, 1972; Gösele et al., 1999) and indicates that 'atomic contact' between two crystals is of the same kind as within a crystal (Gifkins, 1976).

Mainly geometric models are used to describe grain boundaries. The 'dislocation model' is the fundament for geometrical considerations. Over the years, the different models merged to finally produce the most commonly used 'coincidence site model', which was often revised, modified and extended.

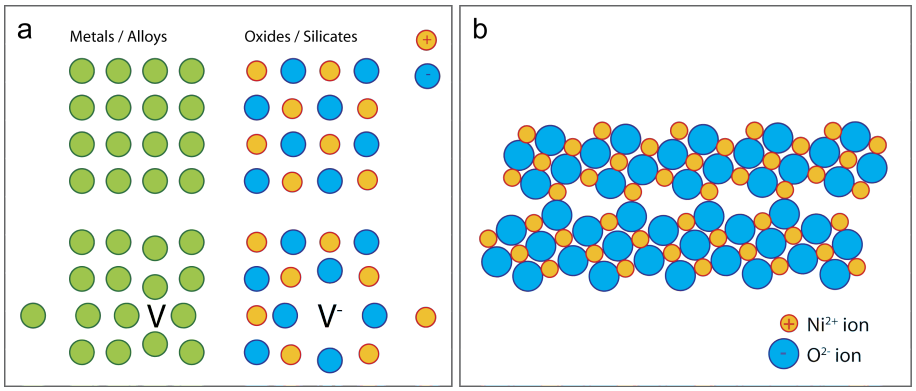

Figure 1.3: (a) Comparison between metals/alloys and oxides/silicates. If an atom is removed from a metallic structure, the 'electron gas' compensates for the resulting charge. In contrast, a charged vacancy (V^-) results if an ion is removed from an ionic structure. Charge compensation is even more important and more complex along planar defects such as grain boundaries (Kliewer & Koehler, 1965). (b) Relaxed structure of a $\Sigma 5$ 36.87° [001]/(310) tilt grain boundary in NiO represented with circles of radii proportional to Pauling values. The need for charge compensation induces a rigid body translation. Blue: oxygen ions; Red: nickel ions. Modified from Duffy and Tasker (1984).

Dislocation Model

The dislocation model is part of most other models and widely applied to describe low angle grain boundaries and distinguish them from high angle grain boundaries. A low angle grain boundary can be described as an array of edge dislocations. The angle between adjacent grains forming the grain boundary only depends on the number of dislocations in the boundary (Fig. 1.4). This has been described by Frank (1951), who formulated a law (eq. (1.1)) that relates the distance between the dislocations d in low angle grain boundaries to the misfit angle α and the length of the burgers circuit $\boldsymbol{b}$:

$$d = \frac{\boldsymbol{b}}{\left(2\sin\left(\frac{\alpha}{2}\right)\right)} \Rightarrow \frac{\boldsymbol{b}}{\alpha} \tag{1.1}$$

At some angle, the dislocation cores will overlap each other, making it impossible to distinguish individual dislocation lines. This angle defines the transition from low

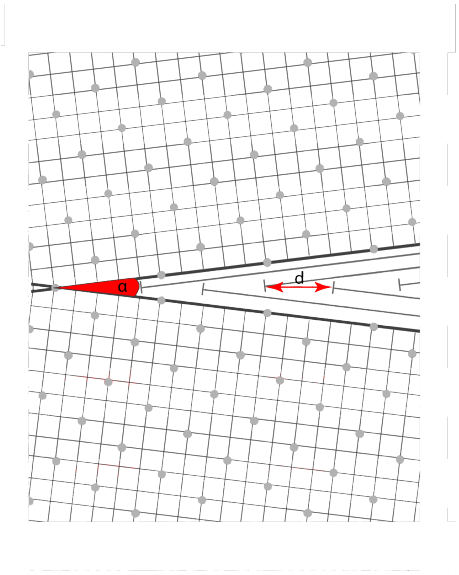

Figure 1.4: Relation between dislocation density d/$\boldsymbol{b}$ and misfit angle α of a grain boundary. Frank's formula relates α to the ratio of the distance d between individual dislocations and the Burgers vector $\boldsymbol{b}$ of these dislocations. Dislocations at the grain boundary plane can generate or compensate an additional misfit angle.

to high angle grain boundaries. For metals and alloys, the maximum angle where individual dislocation lines can be distinguished is between 10-15°, whereas in oxides angles as high as 21.5° can be reached (Heinemann et al., 2005). With increasing misorientation, grain boundary energies and transport properties are thought to increase. Both are generally larger for high-angle and *general* grain boundaries compared to low-angle grain boundaries, *special* grain boundaries exempt (Chadwick & Smith, 1976; Wolf & Yip, 1992; Sutton & Balluffi, 1995; Lojkowski & Fecht, 2000).

Coincidence Side Lattice Model

All atoms in the boundary are influenced by both crystal lattices. They try to occupy optimum positions, which would be positions where they belong to both crystal lattices. Those positions are referred to as coincidence sites. Atoms on other positions than coincidence sites have higher free energies. From a simple theoretical consideration it follows that the free energy of the grain boundary would be twice that of a free surface, if no contact between the atoms of the lattices existed (Wolf & Yip, 1992). Accordingly, the atoms in the boundary region adjust

their positions, which increases the strength by bond formation and decreases the energy of the boundary. The lattices of both crystals that influence the atoms of the grain boundary are strictly periodic, therefore the arrangement of the atoms in the boundary should also be periodic, presumably on a larger scale. Rigid body translations do not affect the periodicity, but can cause a relaxation along the grain boundary without rotation or atom displacement.

These considerations lead to the most commonly used grain boundary model, the coincidence side lattice model (CSL, Gleiter & Chalmers, 1972; Chadwick & Smith, 1976; Sutton & Balluffi, 1995). In this model, two three-dimensional lattices are super-imposed and translated until they coincide at lattice sites (see also chapter 3.1) and generate a super periodicity or 'super lattice', which is then referred to as the coincidence site lattice.

The Σ-nomenclature is commonly used to describe the relation between the number of lattice points in the unit cell of a CSL and the number of lattice points in the unit cells of the generating lattices. It is defined as $\Sigma = 1/n$, where n is the fraction of the lattice points of the two super-imposed lattices that coincide. A more detailed description of the CSL and the Σ-nomenclature is provided in chapter 3.1. Generally speaking, Σ-boundaries are energetically favorable over *general* boundaries and low Σ-boundaries are favourable over high Σ-boundaries.

1.1.3 Abundance of Grain Boundaries

Low Σ-grain boundaries, for instance twins, should be abundant in natural or synthetic polycrystalline aggregates and dominate the boundary network, and thus the bulk properties (C.-S. Kim et al., 2006; Z.-h. Chen et al., 2008; D. Chen et al., 2009). Different studies (Cho et al., 1998; Mao, 2001; Barmak et al., 2006; Vonlanthen & Grobety, 2008) show the correlation between misorientation and abundance of grain boundaries (Fig. 1.5). Misorientations, where more low Σ-grain boundaries occur, are more frequently observed.

The grain boundary plane orientation distribution, in contrast to the grain boundary misorientation distribution, is specified by a five parameter grain boundary character distribution (GBCD). The GBCD is defined as the relative areas of grain

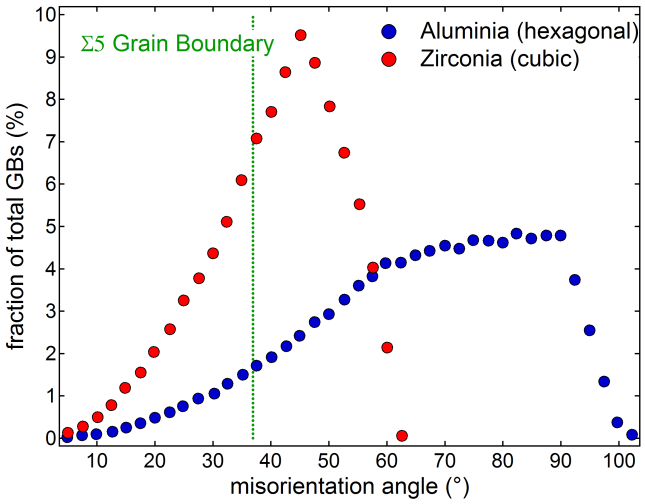

Figure 1.5: Abundance of grain boundaries with a certain misorientation in α-Al_2O_3 (hexagonal) and zirconia (cubic). Both materials are randomly oriented, thus they do not show a lattice preferred orientation (Vonlanthen & Grobety, 2008). The distributions are characteristic for the specific crystallographic systems. The misorientation of the $\Sigma 5$ grain boundary, indicated as green dashed line, that I studied in a cubic material (YAG) as part of this thesis is relatively abundant in cubic materials and its behaviour is thus important for the overall behaviour of grain boundaries in YAG.

boundaries of different types, distinguished by their lattice misorientation and grain boundary plane orientation. Even though the GBCD strongly influences materials properties, it has only rarely been studied (Cho et al., 1998; Mao, 2001; Schuh et al., 2005; Barmak et al., 2006; Randle, Rohrer & Hu, 2008; Vonlanthen & Grobety, 2008; Dillon & Rohrer, 2009; Li et al., 2009; Pennock et al., 2009). Only recently, the increased computing power, as well as new analytical methods (FIB-SEM), allowed for measuring all five grain boundary parameters in tolerable time (Rohrer et al., 2004; Rohrer, 2007; Randle, Rohrer & Hu, 2008; Dillon & Rohrer, 2009). The 'five-parameter analysis' demands for serial sectioning, where several parallel planar sections are EBSD mapped and used to reconstruct the 3D grain boundary network (Randle & Davies, 2002). The GBCD of different metals and alloys seems to be independent of composition, processing, substructure, and grain size. There is a clear tendency for grains to terminate on low index planes. These, in turn, dominate the grain boundary network (Saylor et al., 2004; Schuh et al., 2005).

In chapter 3.1 of this thesis, I synthesized a *near* Σ-grain boundary and analyzed

its structure and behavior during temperature annealing on the atomic scale. One goal of this specific experiment was to understand, if crystals in *near* Σ-orientations turn into Σ grain boundaries during temperature treatment.

1.1.4 Methods to Synthesize Grain Boundaries

Sintering is one of the earliest methods to prepare oriented bicrystals (Coble, 1961; Raj et al., 1975; Kimura et al., 1986; Kaiser et al., 1987). Today, there are numerous methods for the synthesis of bicrystals and a thorough overview is given by Tong and Gösele (1999). Here, I will only briefly introduce a few techniques that are widely used, including (1) ultra high-vacuum (UHV) diffusion bonding, (2) wafer direct bonding, (3) directional crystallization/solidification, and (4) the flux method. Growth techniques are generally not able to produce defined *general* grain boundaries, as during growth the grain boundary tries to achieve a minimum energy configuration und thus *special* grain boundaries result.

1. UHV diffusion bonding requires a special bonding chamber, where an UHV can be maintained during heating and pressurizing the bicrystal. Temperatures above 1300°C are usually maintained for about 6 h for bonding, the applied pressures are in the range of 4-5 MPa. (Gemming et al., 2003; S. B. Lee et al., 2003; Peters & Reimanis, 2003).

2. In direct wafer bonding, two highly polished and cleaned wafers are brought into contact at ambient conditions without applying force. The initial bond is weak and is formed by hydrogen bonds, thus only van der Waals forces are active. The bonding strength increases during high temperature annealing, typically above 1000°C (Maszara, 1991; Tong et al., 1995; Ljungberg et al., 1997; Gösele et al., 1999; Pössl & Kräuter, 1999; Heinemann et al., 2001).

3. Directional crystallisation/solidification is a method to grow oriented bicrystals from a melt. Bicrystals with desired orientation are used as seed to initiate growth of oriented bicrystals. However, the boundary in the growing crystal often exhibits a different orientation, as it tends to minimize its energy during growth (Mitzi et al., 1990; Surholt et al., 1998; Tsu et al., 1998; Schwarz et al.,

2002).

4. The flux method is an alternative technique to grow crystals in a melt, but the resulting orientation relation in the bicystals can not be influenced (Kaiser et al., 1987; Tsu et al., 1998).

These techniques yield bicrystals of different quality, quantity and size. In this work, I took advantage of the potential of the direct wafer bonding technique to produce well defined grain boundaries. The synthesised grain boundaries showed a minimum of defects as discussed in chapters 3.1 and 3.4 of this work. They are perfectly suited for element diffusion experiments with well known boundary conditions, in particular, they allow for simultaneously quantifying volume and grain boundary diffusion on the atomic scale as discussed in chapters 3.2 and 3.3.

1.2 Diffusion

Various solid-state phenomena, such as phase transformations and other microstructural changes, that occur in materials are largely diffusion controlled. Diffusional processes in turn are strongly influenced by the local defect structure of the specific material. Defects, in particular grain boundaries, are the most important short-circuiting paths for element diffusion (Okabe et al., 1981; Kaur et al., 1995; Mishin & Herzig, 1999; Jiménez-Melendo et al., 2001; Milke et al., 2007; Keller et al., 2008). Generally speaking, diffusion is the macroscopic result of random thermal motions on the atomic scale. The disordered two dimensional structure of the grain boundary generally provides a less dense medium for atomic movements, compared to the ordered structure of the perfect crystal lattice, and diffusion is significantly enhanced. Grain boundary diffusion is orders of magnitude faster compared to volume diffusion, especially at temperatures below $0.6 \times T_m$ (T_m = melting point of the matrix), and it plays a major role in processes that involve material rearrangement, such as Coble creep, sintering, diffusion-induced grain boundary migration, discontinuous-precipitation-dissolution-coarsening, recrystallization, grain growth, etc. (Kaur et al., 1995). Despite its importance, element diffusion is a research topic that is far from being understood.

1.2.1 Volume Diffusion

To balance chemical gradients in any material, there will generally be a net flux of atoms from the higher concentration towards the lower concentration. In a structurally isotropic material, the diffusant flux J is proportional to the gradient in concentration c in the direction of diffusion (Kaur et al., 1995; Ganguly et al., 1998; Mishin & Herzig, 1999).

$$J = -D\nabla c \tag{1.2}$$

where ∇ is the gradient vector operator defined as (in a rectangular coordinate system *(x, y, z)*

$$\nabla = \frac{\partial}{\partial x} + \frac{\partial}{\partial y} + \frac{\partial}{\partial z} \tag{1.3}$$

The diffusion coefficient D is a proportionality constant and a measure of the diffusion rate of the moving atoms. D is assumed to be concentration independent, which is true for most diffusion studies where small amounts of the diffusant are considered. A convenient expression for the experimental determination of D is given by the second law of Fick. At a given position, the concentration gradient is related to the change of concentration with time (Fick, 1855; Kaur et al., 1995):

$$\frac{\partial c}{\partial t} = -\nabla J \tag{1.4}$$

If the assumption of a position-independent (which also implies concentration- and time-independent) D is made and J is substituted by eq. (1.2), one derives

$$\frac{\partial c}{\partial t} = D\nabla^2 c \tag{1.5}$$

which is often referred to as the diffusion equation. The experiments that I carried out in the present work are designed in a way that diffusion is unidirectional (diffusion occurring only in the x-direction), which reduces the diffusion equation to

$$\frac{\partial c}{\partial t} = D\frac{\partial^2 c}{\partial x^2} \tag{1.6}$$

The concentration $c(x,t)$ of the diffusant that I measure in the one-dimensional diffusion experiments in this thesis (chapter 3.2) can be related to the diffusion coefficient D. The diffusant diffuses in an initially diffusant-free specimen. The thin-film corresponds to $h = x < 0$ and the crystal corresponds to the region $x > 0$. The corresponding solution is (Crank, 1975):

$$c(x,t) = \frac{c_0}{2}\left[erf\left(\frac{x+2h}{2\sqrt{Dt}}\right) - erf\left(\frac{x}{2\sqrt{Dt}}\right)\right] \tag{1.7}$$

In case of homogeneous volume diffusion in the x-direction, isoconcentration contours parallel to the x = 0 surface develop. This is a useful effect and can be used to evaluate if the volume affected by diffusion was homogeneous. The temperature dependence of the diffusion coefficient obeys an Arrhenius relationship:

$$D = D_0 \exp(-Q/RT) \tag{1.8}$$

Where the pre-exponential factor D_0 is a constant and independent of temperature, Q is the activation energy of the diffusion process, R is the molar gas constant, and T is the absolute temperature. D_0 and Q are referred to as the Arrhenius Parameters.

In the present work, I determined the volume diffusivity to a first approximation by fitting the experimentally derived diffusion profiles with the one-dimensional analytical solution to the diffusion equation (1.7). In order to evaluate the feasibility of this analytical solution and the associated simplifications, a numerical model was developed, based on the observations that I made in the specific diffusion experiment. I discuss the comparison between analytical solution and numerical model in chapter 3.2.

1.2.2 Grain Boundary Diffusion

Diffusion in grain boundaries is generally divided in three kinetic regimes, which are defined by the ratio between the characteristic diffusion length in the volume (L_v) and along the grain boundaries (L_{gb}). This classification was proposed for the first time by Harrison (1961). According to Harrison (1961), the diffusion flow in a polycrystal in kinetic regime 'C' is dominated by grain boundary diffusion, and volume diffusion can be neglected. In the kinetic regime 'B', volume and grain boundary diffusion are both important, but the diffusion from adjacent grain boundaries into the crystal volume do not overlap. In the 'A' regime, the diffusion length of the volume diffusion is comparable to the diffusion length of grain boundary diffusion. This is the case for nanocrystalline materials, very long diffusion anneals, high volume diffusion coefficients, or temperatures close to the temperature of melting. The three regimes are illustrated in figure 1.6.

Because both L_v and L_{gb} depend on temperature, grain size, and time, they are valid only for a certain set of these variables. To experimentally investigate grain boundary and volume diffusion simultaneously, the 'B' regime is most appropriate

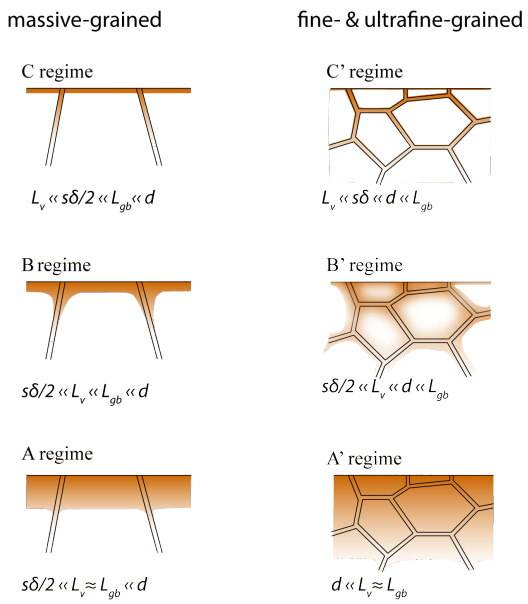

Figure 1.6: Schematic illustration of the distribution of the diffusant in different kinetic regimes according to Harrison (1961) (figure after Mishin and Herzig (1995)). The nomenclature is as follows: s = segregation factor; δ = effective grain boundary width; d = grain size; L_v = the characteristic diffusion length in the volume; L_{gb} = the characteristic diffusion length in the grain boundary.

and it is favourable to use bicrystals having the grain boundary normal to the diffusant source (Le Claire, 1963). A sketch of this experimental setup is shown in figure 1.7a, as it is the approach that I used to study diffusion (chapter 3.3).

Analytical solutions to the diffusion equation to describe this experimental situation are based on the following assumptions (Kaur et al., 1995):

1. Fick's laws of diffusion are valid in the crystal volume and the grain boundary.
2. D_v and D_{gb} are isotropic and independent of concentration, position, and time.
3. The diffusant flow is continuous at the grain boundary/crystal interface at $x = \pm\delta/2$.
4. The grain boundary width δ is small enough for the concentration variation across it to be ignored.

Fisher (1951) treated the grain boundary as a thin (thickness δ of atomic dimensions) uniform rectangular slab embedded in a semi-infinite crystal, the diffusion

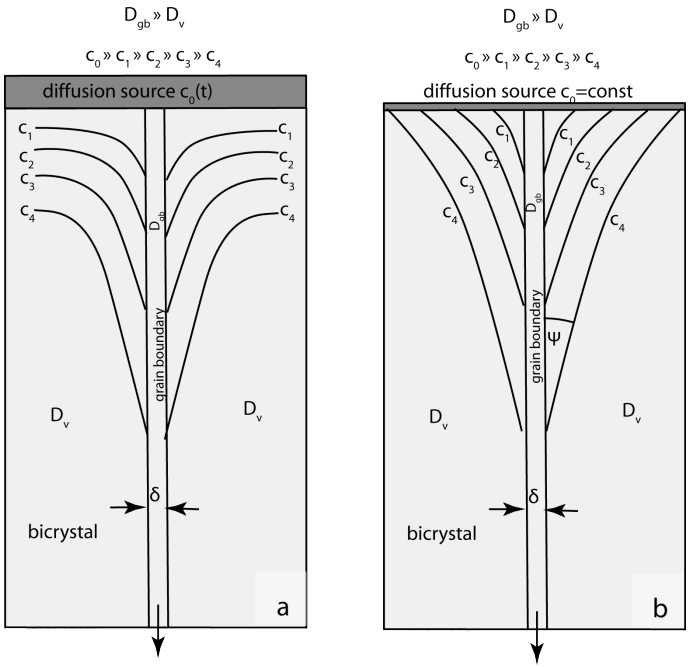

Figure 1.7: (a) Sketch of the experimental setup that I used for the diffusion experiments. A thin-film serves as diffusant source. (b) Isoconcentration contours typical for Fisher's approximate solution for diffusion from a constant source. Ψ refers to the angle between the diffusion contours and the grain boundary slab.

coefficient in the slab (D_{gb}) is much larger than that outside it (D_v). The diffusion source is assumed to have a constant concentration. He took the lateral leakage of the diffusant from the grain boundary into the semi-infinite crystal into account, but neglected the direct volume diffusion contribution from the source into the crystal (Fig. 1.7b).

Whipple (1954) formulated a more exact solution to the same homogenous slab model of Fisher for diffusion from a constant source. The work of Levine and MacCallum (1960), combined with the work of Le Claire (1951), made routine applications of the exact solutions to experimental measurements possible as the former expressions were too complicated to be applied to experiments. Their approach to the problem of grain boundary diffusion was completely different and based on a polycrystalline body in general. According to their model, log$D$ varies linearly with $x^{5/6}$ in the grain boundary diffusion region.

Suzuoka (1961) formulated an exact solution for diffusion from an instantaneous source. He assumed that the diffusion source is an infinitely thin layer with a no flux condition at the surface. This is valid only, if the diffusion rate at the surface is close to that in the volume, and in the region of the grain boundary that is close to the surface. Furthermore, the grain boundary must not act as a sink for the diffusant. During annealing, the concentration of the diffusant in the source decreases according to this solution.

In summary, Fisher's approximate solution and Whipple's and Suzuoka's exact solutions are the most important analytical solutions for the isolated grain boundary model.

However, they are based on various assumptions and the appropriate analytical solution must be chosen based on the individual experimental arrangements, thus the surface conditions. I find that none of the standard analytical models adequately describes the experimental setup that I used in this work (Fig. 1.7a). Therefore, a numerical model was developed that accounts for my specific experiment and the TEM observations that I made on the structure of the diffusant source and the grain boundary (chapter 3.3).

Influence of the grain boundary structure on grain boundary diffusion

None of the grain boundary diffusion models described above considers the influence of the grain boundary structure on grain boundary diffusion (Wuensch & Tuller, 1994). However, many experiments (Turnbull & Hoffman, 1954; Surholt et al., 1998; Budke et al., 1999; Klugkist et al., 2001) and computer simulations (Siegel & Hamilton, 2005; Suzuki & Mishin, 2005; Divinski et al., 2007; Divinski & Wilde, 2008) show that diffusion rates strongly vary with grain boundary orientation and hence structure.

Experiments have mainly been performed on metals and oxides (Chadwick & Smith, 1976), where polycrystals/bicrystals with tilt grain boundaries were the main investigative target (Turnbull & Hoffman, 1954; Herbeuval et al., 1973; Sommer et al., 1995). Twist grain boundaries in bicrystals were studied only rarely (Schwarz et al., 2002; Noort et al., 2007). Computer simulations to understand the influence of the grain boundary structure on diffusion were performed as early as the mid 80s (e.g. Metsch et al., 1986; Chung et al., 2000; Campbell et al., 2004; Suzuki & Mishin, 2005; Frolov & Mishin, 2009). Monte Carlo simulations of grain boundary diffusion showed that grain boundary diffusivities vary by 4 to 10 orders of magnitude depending on the grain boundary orientation and temperature (Suzuki & Mishin, 2005; Frolov & Mishin, 2009). Furthermore, the physical and chemical properties of diffuse and sharp grain boundaries are fundamentally different (Sutton & Balluffi, 1995).

This thesis contributes to our understanding of the relation between grain boundary structure and element diffusion along a specific boundary. Chapters 3.1 and 3.4 give detailed information about the structural properties of a synthetic grain boundary, whereas chapter 3.3 reports experimental results on element diffusion along the same grain boundary.

1.2.3 Methods to Study Diffusion

This chapter gives a brief overview of the techniques that are routinely used to study grain boundary diffusion in the crystal volume and along grain boundaries and discusses their advantages and disadvantages. In general, the methods to study

diffusion can be separated in direct and indirect methods. Direct methods are those, where the distribution of the diffusant is either measured directly during the diffusive treatment, or after such a treatment. Indirect methods study physical phenomena caused by diffusive processes, for instance diffusional creep, electro transport, sintering or phase transformations, and estimations on the diffusion coefficients are drawn from these observations. Direct methods are favorable as the rate-controlling mechanism does not have to be defined *a priori*.

Direct methods include (1) concentration contour imaging methods, (2) lateral spreading approaches, (3) surface accumulation techniques, and (4) sectioning experiments. Each method can be carried out in combination with different analytical methods. A nice overview of analytical techniques is given by Kaur et al. (1995).

1. Concentration contour imaging methods map iso-concentration contours of diffusion in the volume and along grain boundaries. The parameters of the contours can be related to the diffusion coefficients using standard equations.

2. Lateral spreading methods are mainly used to study diffusion in delicate thin-films. For such studies overlapping thin-films are produced and the movement of the diffusion front after annealing is monitored. Peak-like zones at the front are then attributed to grain boundary diffusion. As diffusion occurs at the plane of the sample, and not within the sample itself, it is influenced by surface diffusion, which complicates the interpretation of the lateral diffusion data. On the other hand, this technique does not require sectioning work.

3. In surface accumulation methods, measurements are carried out on the backside of the sample, which is the side not covered with the diffusant source. The accumulation of the diffusant is monitored during the diffusion experiment. These experiments are especially interesting for the investigation of diffusion in thin-film specimens, which are of particular interest in modern microelectronic devices. Generally, it is favorable to use a heavily emitting isotope as diffusant, which allows to reduce the detection limit.

4. Sectioning methods aim at depth profiling the average concentration. The average concentration is measured in short spatial intervals parallel to the diffusion

source. The slope of the obtained profile is evaluated using standard equations. A number of experimental techniques are available for different experimental conditions, for example the classical radio tracer method.

Even though, analytical TEM (ATEM) has been used to study low temperature volume diffusion as early as 1983 (Nicholls & Jones, 1983), its high demands on sample preparation prevented well defined diffusion studies on grain boundaries. This changed when FIB-sample preparation became available about a decade ago (Phaneuf, 1999; M. R. Lee et al., 2003; Wirth, 2004). In the present study, I use ATEM as a depth profiling method. In contrast to common depth profiling approaches, the averaging and the spatial intervals are minimized by cutting an oriented FIB lamella across the grain boundary and measuring the grain boundary diffusion at spots/windows of 20×40 nm^2; thus the influence of the crystal volumes is minor. The spatial resolution for the measurement is basically limited by the window size selected. Thus, it is possible to acquire an energy dispersive spectra (EDS) every 20 nm. I show in chapters 3.2 and 3.3 of this thesis that ATEM is well suited to study volume as well as grain boundary diffusion. The results can be complemented by simultaneously derived information about the structure of the sample and the grain boundary on the atomic scale (chapters 3.1 and 3.4). The combination of these capabilities makes TEM a very promising tool for the study of diffusion processes and their relation to structural properties.

Many of the above mentioned methods involve estimations of the *effective* grain boundary width to extract diffusivities, which is still debated and most probably varies from system to system, and depends on the exact processes and elements studied. One goal of this thesis is to enhance our understanding of the *effective* grain boundary width for diffusional processes on the atomic scale by using TEM-based analytical techniques (chapter 3.4).

Chapter 2

Results and Discussion (Synergy)

In this chapter, I summarize and discuss the main results of my PhD-research. The four major parts of this thesis, which are published or submitted for publication in international scientific journals, and their tight connection are outlined here. The complete manuscripts can be found in chapters 3.1 – 3.4.

2.1 Synthetic *near* Σ5 (210)/[100] Grain Boundary in YAG Fabricated by Direct Bonding – Structure and Stability

(this abstract is based on chapter 3.1)

To date, the most complete picture on grain boundary structures emerges from studies on metals and alloys, simple metal oxides, and few complex ionic compounds (Gleiter & Chalmers, 1972; Carter & Föll, 1978; Föll & Ast, 1979; Carter et al., 1981; Cunningham et al., 1982; Sutton & Balluffi, 1995; Ernst et al., 1999; Christophersen et al., 2001; S. B. Lee et al., 2003; Merkle et al., 2004; Randle, Rohrer & Hu, 2008). In contrast, studies on more complex oxides, including silicates, the most relevant compounds from an Earth sciences point of view, are rare. Systematic work on synthetic grain boundaries is a promising way to progress towards a better understanding of grain boundary structures in these materials. I explored the suitability of the wafer direct bonding method (Tong & Gösele, 1999) to produce well defined synthetic grain boundaries within a bicrystal of yttrium aluminium garnet (YAG). This method allows to join two well polished material slices without glue, force, or ultra high vacuum, instead, bonding is initiated at ambient conditions (Harendt et al., 1992; Pössl & Kräuter, 1999). However, several aspects of the wafer direct bonding method and the produced bicrystals are not fully understood, including the temperature needed to obtain strong bonds across the interface. For further processing, bonds with strength comparable to those in the crystal volume are desirable. This, for instance, is prerequisite for the subsequent grain boundary diffusion experiments that I performed as part of this thesis, because the bicrystal has to be cut in order to deposit a thin-film perpendicular to the grain boundary (see chapter 2.3).

Here, I used the wafer direct bonding method to produce several grain boundaries,

which I annealed at different temperatures, ranging from 673 to 1873 K. The resulting grain boundaries are not distinguishable based on their flatness and apparent cohesiveness in high resolution TEM (HRTEM) micrographs (Fig. 2.1). However, I observed a considerable step in their mechanical stability at around 1273 K, a temperature that corresponds to about 60% of the melting temperature of YAG. Below this specific annealing temperature, the wafers can easily be separated at the interface. In contrast, separation attempts on samples, which were annealed at higher temperatures, resulted in fractures through the volume of the crystals. Based on these observations, I conclude that temperatures of at least ∼60% of the melting temperature are required to reach bonding strengths that are comparable to the bonds in the volume of a single crystal.

The synthesized grain boundary is a *near* Σ5 (210)/[100] grain boundary, as shown in the HRTEM image in figure 2.2. The diffraction pattern (inset in Fig. 2.2) confirms the rotation of ∼36.9° of the two crystals with respect to each other.

Along this grain boundary, I observed a long-range strain contrast with a periodicity of roughly 40 nm (Fig. 2.3a). Even though long-range strain contrasts have been observed for low-angle grain boundaries, they have not been reported for high-angle grain boundaries so far. I show that these strain fields are associated with steps along the interface (Fig. 2.3b). I find that these periodic extended strain fields are an intrinsic property of the grain boundary and conclude that they are caused by faceting along the grain boundary plane. This is needed to achieve a minimum energy configuration of the grain boundary plane.

Here, I demonstrate that the direct wafer bonding method allows for producing well defined grain boundaries with any desired orientation. These synthetic bicrystals are perfectly suited as starting materials for element diffusion experiments that could enhance our understanding of grain boundary diffusion in relation to the atomic structure of the specific grain boundary. The associated experiments that I performed as part of this thesis and their findings are discussed in the chapters 2.2 and 2.3.

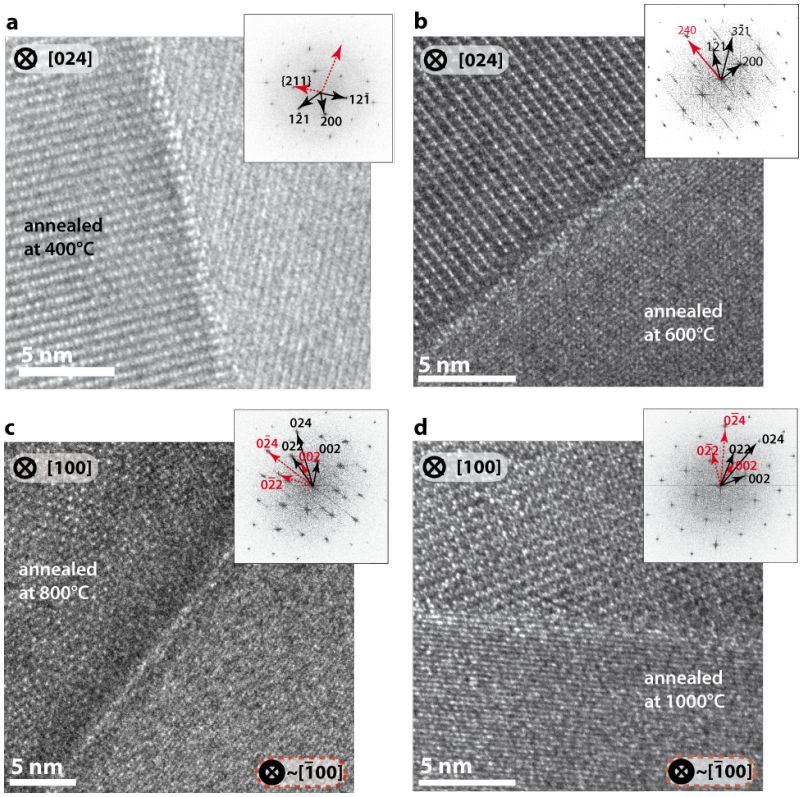

Figure 2.1: HRTEM images of grain boundaries synthesized at 673, 873, 1073 and 1273 K (a-d). At all stages, the lattice fringes of the opposing crystals touch each other at the interface and no amorphous material or material with different structure is observed. The varying image quality results from the differing thicknesses of the respective TEM lamellae.

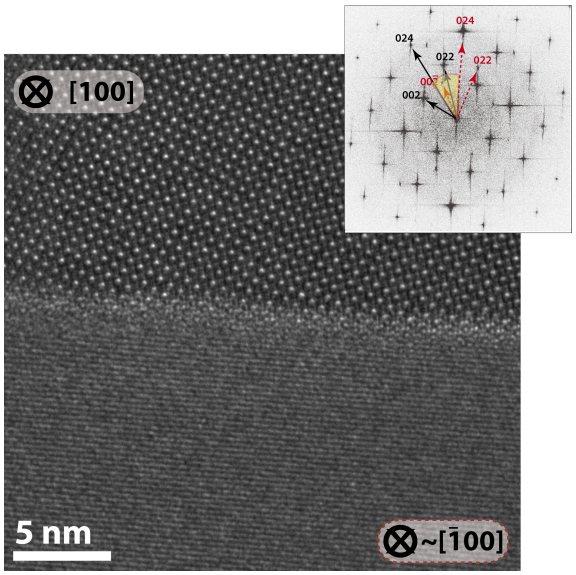

Figure 2.2: HRTEM image of the *near* Σ5 (210)/[100] grain boundary. The [100] direction of the upper crystal is parallel to the incident beam. [100] is the common axis of a perfect Σ5 twin boundary. As the misorientation with respect to this orientation is small, each crystal shows a diffraction pattern of a <100> zone axis. They are rotated by ∼36.9° towards each other around this axis (illustrated by yellow angle). The lower crystal is not perfectly aligned in [1̄00] and thus only one set of lattice fringes can be seen in the image.

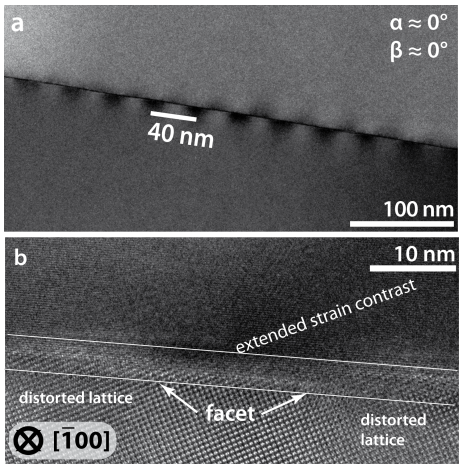

Figure 2.3: (a) TEM bright field image of the bicrystal grain boundary. The sample thickness decreases towards the left margin. The periodicity of the dark contrast along the grain boundary is about 40 nm. (b) Lattice fringe image of the bicystal at a relatively thick part of the sample, where the zone axis of the lower crystal is oriented parallel to the incident beam. Most of the grain boundary plane area lies in the (042) plane except for the steps of the facet, which is spatially related to the extended strain contrast, represented by the dark contrast. Furthermore, the lattice on both sides of the facet is distorted, causing a slightly blurred image.

2.2 Volume Diffusion of Ytterbium in YAG: Thin-film Experiments and Combined TEM – RBS Analysis

(this abstract is based on chapter 3.2)

Rocks that are exposed to changing physical and chemical conditions tend to re-equilibrate, frequently by element diffusion. Laboratory experiments play a major role to develop a quantitative understanding of diffusional processes. They often performed in so-called thin-film geometry, where a thin layer that contains the diffusant is deposited onto a substrate. After annealing the sample at a certain temperature for a definite time, the element exchange between thin-film and substrate can be measured and this information is used to derive the particular diffusion coefficient. However, these laboratory studies demand for well defined sample geometries and precise knowledge of the specimens' microstructures.

Here, I used the pulsed laser deposition (PLD) technique to deposit a thin-film of defined thickness and chemical composition onto a substrate of YAG. After a diffusion anneal, both analytical TEM (ATEM) and Rutherford backscattering (RBS) were used to measure the diffusion profile from the thin-film into the substrate. The results show that reliable diffusion data can be determined by TEM (Fig. 2.4). Furthermore, TEM allows to derive complementary information about the local defect structure of the thin-film and the substrate. This additional capability was used to study if the initial geometry and microstructure of the thin-film was maintained during temperature annealing, and if any disturbing effects such as reaction between source and substrate took place. Knowledge of the condition of the thin-film is of fundamental importance to validate the chosen analytical solutions to the diffusion equation (see chapter 1.2).

During the diffusion experiments, progressive crystallisation of the initial amorphous thin-film (Fig. 2.5) took place. The complex behavior of the diffusant source can not be described using existing analytical solutions to the diffusion equation. To test the potential effects of the thin-film's transient state on the derived diffusion coefficients, a numerical model was developed that accounts for the successive

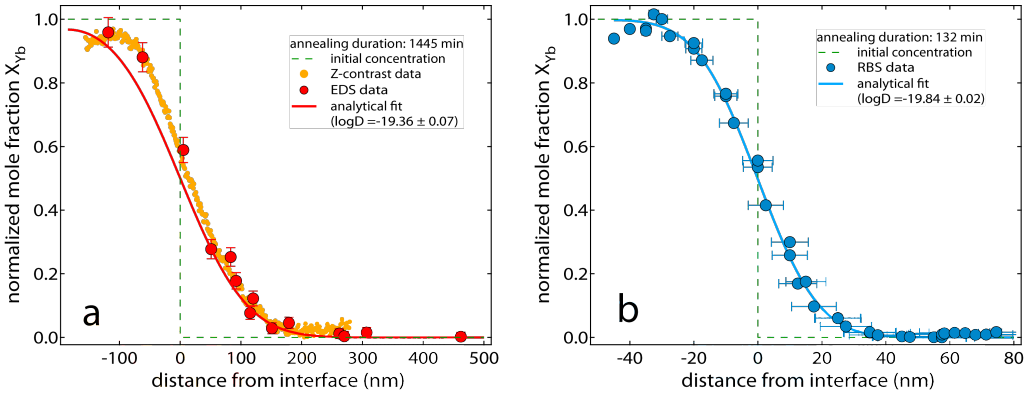

Figure 2.4: Yb diffusion profile in YAG measured by ATEM (a) and RBS (b). The annealing temperature is constant (1723 K), but the time and the thin-film thickness were chosen differently. Note that the abscissas are scaled differently. The interface between thin-film and substrate is at zero. The Yb mole fraction is normalized over c_0 (the initial value in the thin-film). The lines are least square fits to the experimental data using an analytical solution (Crank, 1975), where the only parameter adjusted was the diffusion coefficient D. The uncertainty in log$D$ is the least square error from fitting. Additionally, scanning TEM (STEM) Z-contrast data are shown as yellow dots in (a).

crystallization of the thin-film and the associated change of its transport properties. The effect of a finite thin-film crystallization time t_c is illustrated in Fig. 2.6. The analytical and numerical diffusion profiles are significantly different, when the annealing time t is comparable to t_c. In that case, adjusting the analytical solution to the numerical curve (Fig. 2.6) would lead to an overestimation of the diffusion coefficient in the substrate. In our experiments, $t >> t_c$, which implies that the differences between the analytical and numerical solutions are less pronounced and the analytical solution (equation (1.7), chapter 1) serves as an acceptable model for data reduction (Fig. 2.4).

Although the change in thin-film transport properties, associated with successive crystallization during the diffusion anneal, does not play a major role for our specific experimental setup, this effect cannot generally be ignored. Reliable diffusion coefficients can only be extracted when the diffusion experiments are complemented by a detailed analysis of the boundary conditions, and a careful assessment of the applied solution to the diffusion equation.

This work is the fundament for the subsequent grain boundary diffusion exper-

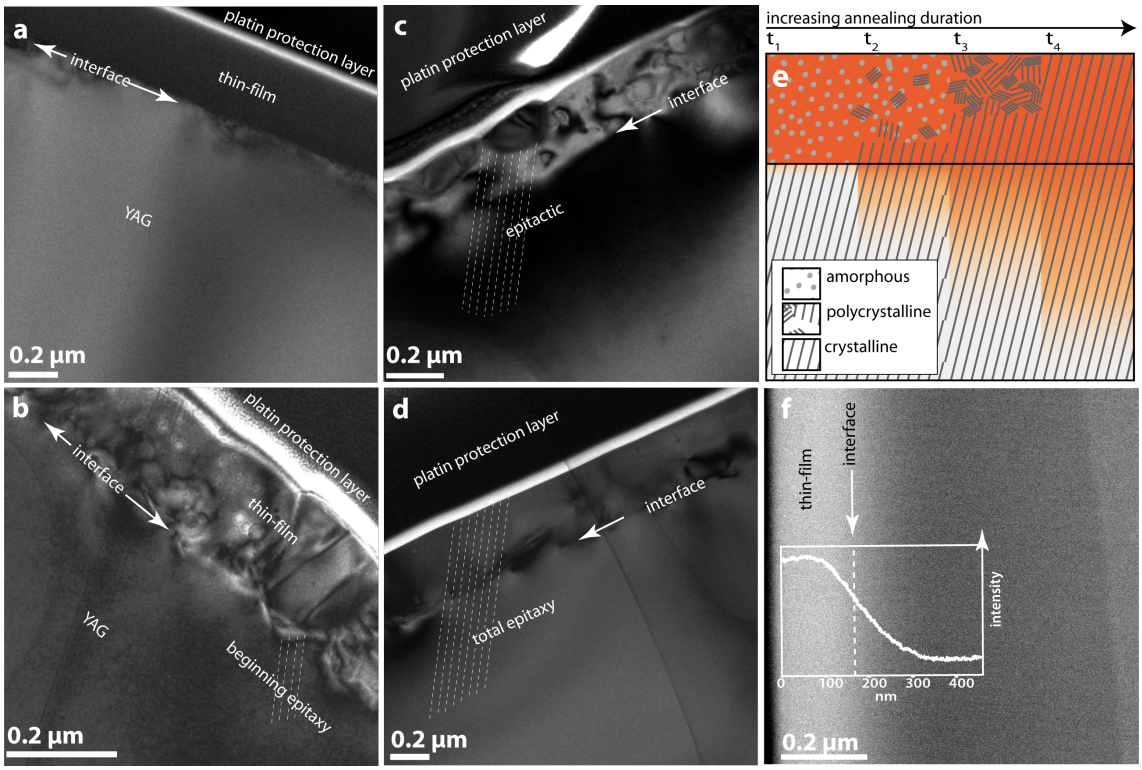

Figure 2.5: (a-d) Bright field (BF) images of the thin-film after different annealing periods at 1723 K. The platinum layer deposited on the surface of the sample limits gallium-ion damage during FIB lamella preparation. Broken lines depict the continuing crystal structure over the initial thin-film/substrate interface. (a) Prior to annealing. The thin-film is amorphous and the interface with the substrate is extremely flat. (b) After 20 minutes. The thin-film became polycrystalline, with crystal diameters ranging from tens to hundreds of nm in diameter. Epitaxy can be observed at the former interface with the substrate, further away no preferential orientation is visible. (c) After 40 minutes. The thin-film starts to copy the orientation of the substrate, but is still polycrystalline at its surface. (d) After 2 hours. The thin-film displays epitaxial growth. The varying diffraction contrast results from small distortions in the crystal lattices. (e) Schematic of the evolution of the thin-film and the diffusion profile with time. (f) STEM Z-contrast image. The brightness, which positively correlates with atomic mass, decreases from the thin-film towards the crystal volume at constant sample thickness, indicating Yb-Y diffusive exchange. At the right side of the image the brightness is compromised by the underlying holy carbon grid which serves as lamellae holder.

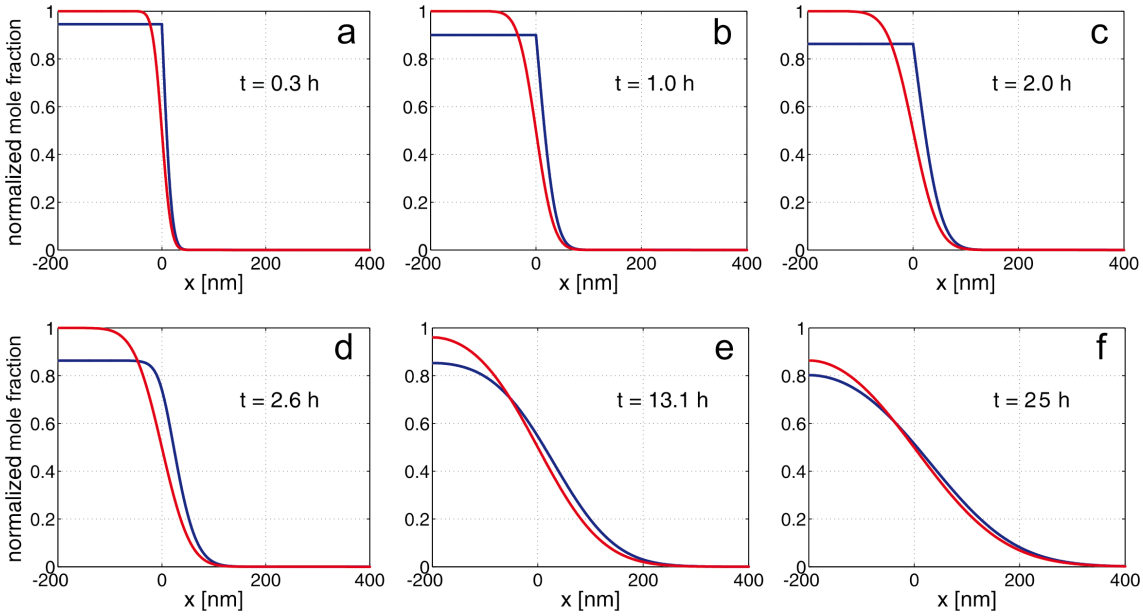

Figure 2.6: Several illustrative numerical solutions to the diffusion equation (blue lines) are shown together with the predictions of the approximate analytical solution (red lines). The thin-film's crystallisation time was set to 2 h. Successive snapshots of the concentration profiles' evolution with time are shown. The two solutions are considerably different for $t \sim t_c$, but the difference decreases for $t >> t_c$.

iments, which I describe in the following chapter 2.3, as it shows the validity of using TEM to quantify diffusion profiles and simultaneously characterize the local structure of the sample.

2.3 Grain Boundary and Volume Diffusion Experiments in Yttrium Aluminium Garnet at 1723 K: A Miniaturized Study

(this abstract is based on chapter 3.3)

Grain boundary diffusion is the dominating element transport mechanism at low temperatures where volume diffusion is slow. Even if the rates of grain boundary and volume diffusion approach with increasing temperature, it is commonly assumed that grain boundary diffusion is prevailing over volume diffusion during most small-scale transport processes of elements in large portions of the solid Earth.

Here, the previously synthesized and characterised bicrystal (chapter 2.1) is used for grain boundary diffusion experiments. The experiments are performed and analysed following the approach that was successfully explored for the volume diffusion study (chapter 2.2). I show that the combination of the used methods is outstandingly well suited to overcome difficulties of previous investigations of grain boundary diffusion, including the following:

1. Grain boundary diffusion studies are mostly performed on polycrystals with randomly shaped grain boundaries and undefined orientation distribution. Thus, the diffusion geometry is very complex and often impossible to characterize adequately.

2. Commonly used methods to measure grain boundary diffusion profiles mostly yield bulk analyses over large areas, which results in a mixed analyses of both grain boundary and volume diffusion. Furthermore, the diffusivity can change by orders of magnitude with varying grain boundary orientation (Herbeuval et al., 1973; Klugkist et al., 2001; Guan, 2003) and, therefore, analysing several grain boundaries at once adds an additional uncertainty to the extracted diffusion coefficient.

3. Solutions to the grain boundary diffusion problem are often oversimplified, or they are not well adapted to the experimental setup, often simply because the

samples cannot be adequately characterized.

Specifically, I took advantage of the following methods to overcome these problems:

1. Simple geometry: Bicrystal synthesis by direct wafer bonding allowed to produce a straight and exactly oriented grain boundary over a length of several μm (see chapter 2.1). As diffusant source, a thin-film is deposited perpendicular to the grain boundary using pulsed laser deposition (see chapter 2.2). The resulting experimental geometry is simple and well defined (Fig. 2.7a).

2. High resolution analytics: Site specific preparation of an oriented sample by the FIB technique (Fig. 2.7a) makes analyses with TEM at the grain boundary possible. The high spatial resolution of TEM allows for the measurement of volume and grain boundary diffusion, even though the profile lengths vary considerably (Fig. 2.8).

3. Numerical modeling: A numerical model was developed that accounts for all experimental observations. Information on the local changes of the thin-film defect structure that occurred during annealing (Fig. 2.7b and c, see also chapter 2.2) helped to design the numerical model accordingly. It allows for a quantitative evaluation of the diffusion coefficients in our specific system (Figs. 2.8 and 2.9). This cannot be achieved using existing analytical solutions, because none meets the present experimental configuration and our observations on the nm-scale.

Using this innovative combination of techniques, I find the grain boundary diffusion coefficient ($D_{gb} = 3 \cdot 10^{-15}$ m^2/s) to be 4.85 orders of magnitude higher than the determined volume diffusion coefficient ($D_v = 4.3 \cdot 10^{-20}$ m^2/s) at the present experimental conditions (1723 K, ambient oxygen fugacity). This difference is likely situated at the lower end of differences between volume and grain boundary diffusion, considering that the studied grain boundary is a *near* Σ5 grain boundary and Σ and low-angle grain boundaries are expected to have the lowest grain boundary diffusivities (Chadwick & Smith, 1976; Kaur et al., 1995; Mishin & Herzig, 1999).

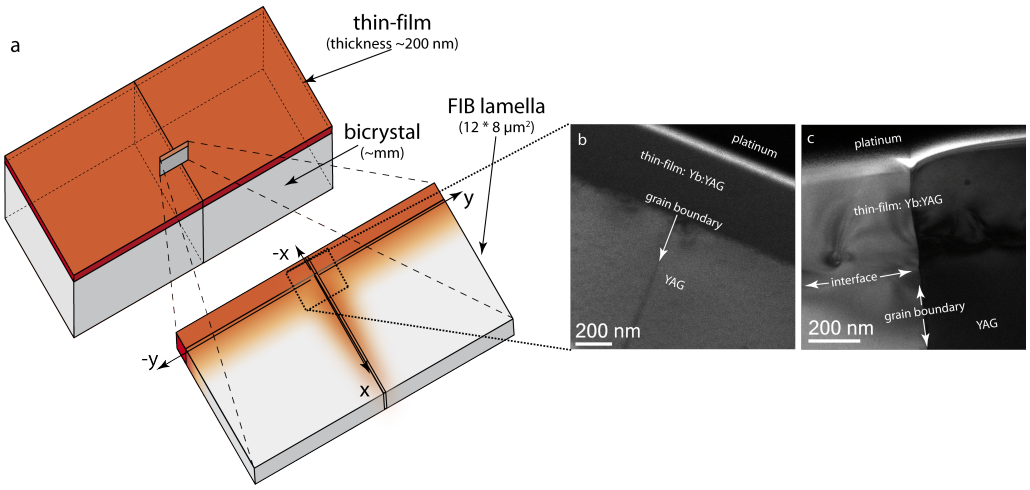

Figure 2.7: (a) Sketch of the sample geometry. The grain boundary of the bicystal is perpendicular to the thin-film (red). The thickness of the thin-film is about 200 nm, whereas the bicrystal's size is in the mm-range. The blow-up shows a draft of the TEM lamella prepared with the FIB technique, its dimensions are usually $15{\times}8$ μm^2, with a thickness between 40 and 150 nm. (b) and (c) are bright field (BF) images of the bicrystal with the thin-film prior to and after annealing, respectively. For FIB sample preparation, a protection layer of platinum was deposited on the surface of the sample, which is visible in the upper part of the images. (b) The thin-film is amorphous and has an excellent contact with the bicystal. (c) Diffraction contrast causes the different grey tones of the opposing crystals. The thin-film grew epitaxially on the bicrystal, thus the grain boundary continues in the thin-film.

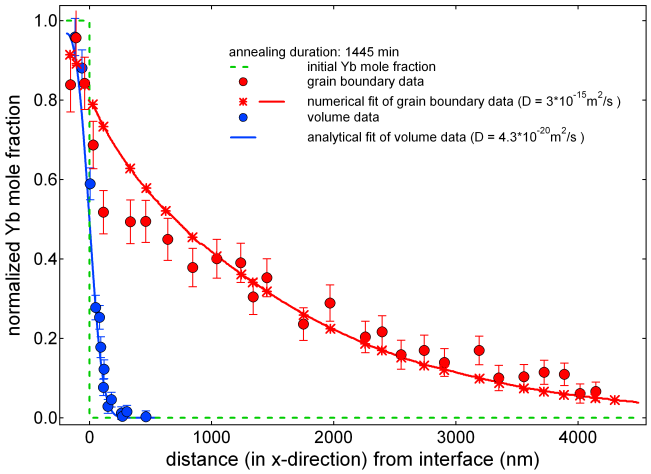

Figure 2.8: Comparison of volume diffusion (blue points) and grain boundary diffusion (red points). Both profiles were measured on the same TEM-lamella. The interface between thin-film and substrate is at zero. The grain boundary diffusion coefficient is 4.85 orders of magnitude higher than that of the volume diffusion. The red stars are the mean values of the calculated mole fraction (averaged over 20×40 nm^2 boxes along the grain boundary of the numerical model).

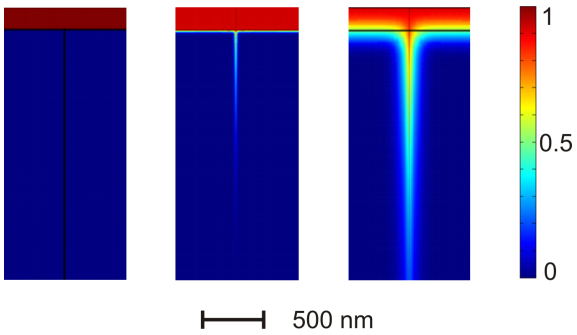

Figure 2.9: Density plots for the mole fraction of Yb $c(x, y, t)$ normalized over the initial value in the thin-film c_0 at different times. Left: the initial distribution, $t = 0$; middle: the distribution at the time of crystallization, $t = t_c$, right: the final distribution at $t = T$.

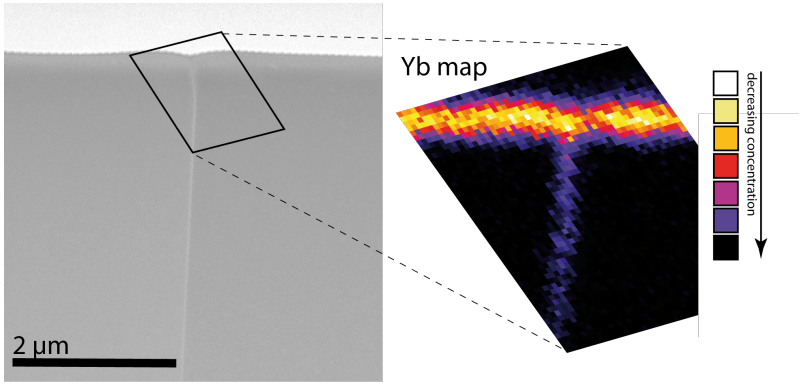

Figure 2.10: STEM image of the sample investigated with nano x-ray fluorescence (left). The camera length is chosen to probe a mixture of Z-contrast and diffraction contrast; it can be seen, that the thin-film is fully epitactic. The platinum layer corresponds to the brightest grey in the image, the thin-film appears in light grey, and the two parts of the bicrystal are dark grey. The region mapped using the Yb-L_α peak from synchrotron x-ray fluorescence is shown in the enlargement.

As part of this study, a diffusion map was also acquired using nano x-ray fluorescence at the European Synchrotron Radiation Facility (Fig. 2.10). Even though the resolution is still relatively poor compared to TEM, the findings are consistent with the numerical simulations (compare Figs. 2.9 and 2.10). This method is a promising tool to obtain quantitative diffusion maps and may soon be advanced enough to bridge the scale-gap between electron microprobe and ATEM.

Most studies, including the present one, use the *structural* grain boundary width to derive the diffusion coefficient from the diffusion experiments. It is known that this approach is a strong simplification, and it might bias the extracted diffusion coefficient as the *effective* grain boundary width for diffusion is the relevant parameter instead. Unfortunately, this parameter is not quantified. This motivated my attempt to directly measure the *effective* grain boundary width by using state-of-the-art atomic-resolution TEM at the National Center for Electron Microscopy in Berkeley. The results are presented in chapter 2.4.

2.4 Insights into the Effective Grain Boundary Width for Diffusion

(this abstract is based on chapter 3.4)

Grain boundaries impact the bulk properties of polycristalline materials and thus play a pivotal role in numerous geological disciplines and in materials science. The *effective* (or chemical) grain boundary width δ (Farver & Yund, 1991) is an imperative parameter in many equations describing diffusional or rheological processes. Despite its importance, it can not routinely be measured. Instead, it is usually determined in combination with the grain boundary diffusion coefficient (either as product or as quotient).

Here, I used the thin-film/bicrystal diffusion assembly, as described in chapter 2.3, and took advantage of the recent developments in abberation corrected HRTEM (Bosman et al., 2007; Kimoto et al., 2007; Urban, 2008) to study the *effective* grain boundary width at the atomic scale.

First, I reconstructed the exit wave from a negative C_s focal series of sub-Ångstrom phase-contrast high resolution transmission electron micrographs (Fig 2.11a). Then, a bicrystal 'unit cell', which represents the orientation of the two crystals forming the grain boundary, was built starting from the rotation of 36.9° around the common <100> direction of the bicrystal that was obtained from the diffraction pattern (Fig. 2.11d). A 'super unit cell' of the grain boundary structure was generated (Fig. 2.11 inset) and used for image simulation with the parameters obtained from the exit wave reconstruction. Iterative adjustments of the 'super unit cell' lead to a match of the simulated images (Fig. 2.11b) with the phase images of the exit wave (Fig. 2.11c). I found that one crystal is rotated by about 12° (counter clockwise) around the <210> direction and about 6.5° perpendicular to this direction with respect to the second crystal.

Electron energy loss spectroscopy (EELS) elemental maps of Yb show higher intensities along the grain boundary compared to the crystal volumes (Fig. 2.12a). The FWHM of Gaussian fits to the Yb-intensity profiles across the grain boundary

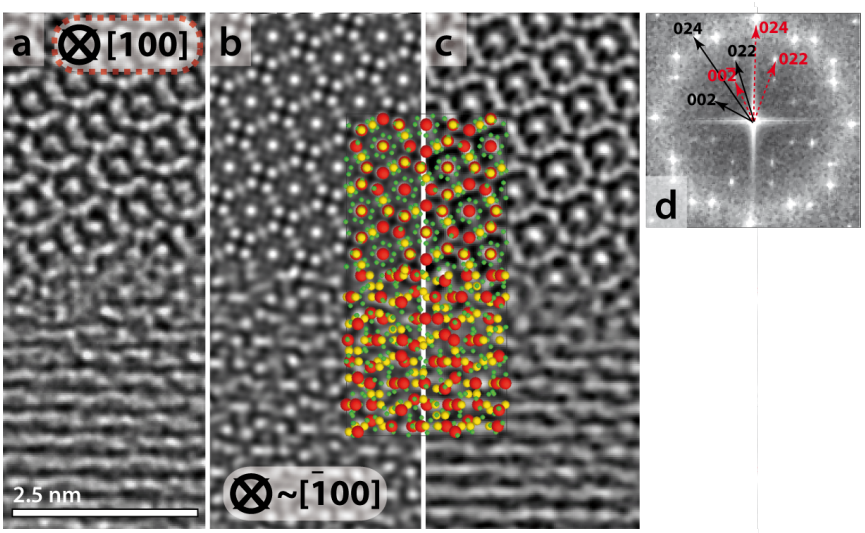

Figure 2.11: (a) HRTEM image at Scherzer defocus. The *structural* grain boundary width is less than 1 nm. (b) Simulated image, the bicrystal structure used for simulation is shown as inset. Y atoms are coloured red, Al atoms are yellow and oxygen atoms are green. The oxygen atoms are drawn to a smaller scale for clarity. A *near* $\Sigma 5$ (210)/[100] grain boundary was simulated; from the diffraction pattern in (d), the rotation of $\sim 36.9°$ around the <100> direction was obtained. Two additional misorientations were needed to simulate the image correctly. First, a rotation of about 12° around the y-axis of the image (corresponding to the <210> direction of both crystals), and second a 6.5° rotation around the x-axis of the image. (c) Imaginary part of the reconstructed electron exit wave. (d) Diffraction pattern of the experimental image (a). The red arrows indicate the diffraction spots that correspond to the upper crystal, whereas the black arrows point at diffraction spots from the lower crystal.

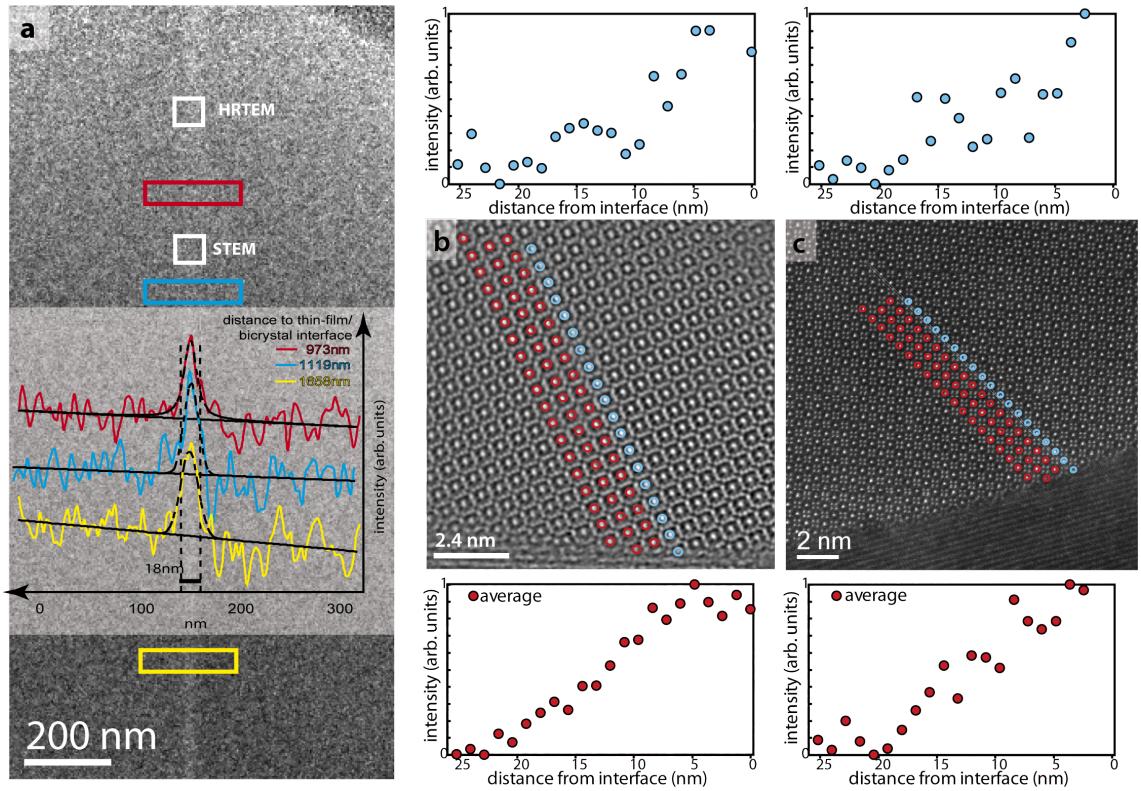

Figure 2.12: (a) Jump ratio map obtained with EELS by using the Yb M_5 1528 eV and M_4 1576 eV edges. A relatively constant zone of increased Yb concentration around the grain boundary compared to the crystal volumes is observed. This becomes evident in the profiles across the grain boundary, which monitor the Yb concentration perpendicular to the grain boundary with increasing distance from the diffusant source (which is located ~100 nm above the top of the figure). The profiles are shifted in intensity with respect to each other for clarity. The white boxes denote the position of the HRTEM (at ~780 nm) and STEM (at ~1050 nm) measurements shown in (b) and (c). (b) shows the imaginary part of the reconstructed electron exit wave. (c) is the STEM Z-contrast image of the same grain boundary about 400 nm further away from the initial thin-film. The strong Z-contrast makes heavier atoms appear brighter. The aligned red circles refer to example profiles taken at the atom columns of interest with an integration width of about 0.1 nm. The profiles run along the [010] direction. The profiles above the images are single profiles, whereas the profiles below the images are averages over ten profiles. The intensity increases towards the grain boundary.

show that the width of the chemically altered region is homogenous over several μm. The concentration of Yb along this slab of constant thickness decreases as shown in an EDS profile (chapter 2.3). Intensity profiles, which were measured by both HRTEM and STEM, two atomic imaging methods complementary in contrast formation, show the same extent of the chemically altered region (Fig. 2.12b, c).

The average profile of the phase image of the exit wave has a FWHM of 21.2 nm perpendicular to the grain boundary and the intensity profile corresponding to the STEM Z-contrast image shows a FWHM of 19.7 nm perpendicular to the grain boundary. The FWHM measured in the two profiles correlate amazingly well, considering that the data were acquired at different positions of the specimen (∼400 nm apart) using different techniques. Furthermore, both are in good agreement with the FWHM obtained from profiles in the elemental map of Yb (17.9 nm). Therefore, I infer that the chemically altered region has a constant width of ∼20 nm within the experimental uncertainty (±3 nm).

In the previous grain boundary diffusion study, I observed blurred parts in the crystal lattices parallel to the grain boundary, which extend over 8 to 12 nm, corresponding to about 20 nm on both sides of the grain boundary (see Fig. 3.14). I concluded that these parts are distorted due to lattice misfit at the grain boundary (chapter 2.1). Based on the findings of this study, I further conclude that this regional strain facilitates the local chemical alteration of similar extent (∼20 nm).

In summary, I observed a slab around the grain boundary with a constant width of ∼20 nm over a length of a few μm, which is strained and chemically altered. I interpret this altered region as the *effective* grain boundary width for diffusion.

This part of my work results in three major findings. First, I show that the *effective* grain boundary width can experimentally be determined. Second, the *effective* grain boundary width in YAG at the present conditions is 20±3 nm, which is ∼40 times larger than standard assumptions of 0.5 nm (Kaur et al., 1995). Third, I illustrate directly that the chemically altered grain boundary region corresponds to the strained/distorted region around the structural grain boundary, which is expected based on theoretical considerations (S. White, 1973; Kingery, 1974; Pond & Vlachavas, 1983). Furthermore, I think that the *effective* grain boundary width

depends on the extension of the strain field around the grain boundary and is thus related to the misorientation angle. Consequently, this would imply that grain boundary diffusivities D_{gb}, are less variable than previously proposed, because the change in the product of D_{gb} and δ could, at least partially, arise from the proposed large variations in δ.

In a nutshell, the four parts of my thesis show the enormous potential of miniaturized sample geometries in combination with TEM analyis to study grain boundary structure and element transport properties at the nm-scale.

Chapter 3

Complete Manuscripts

Synthetic *near* Σ5 (210)/[100] Grain Boundary in YAG Fabricated by Direct Bonding – Structure and Stability

by K. Hartmann, R. Wirth, and W. Heinrich

published in *Physics and Chemistry of Minerals*, 37(5), 291-300 (2010), DOI: 10.1007/s00269-009-0333-z

3.1 Synthetic *near* Σ5 (210)/[100] Grain Boundary in YAG Fabricated by Direct Bonding – Structure and Stability

K. Hartmann, R. Wirth, W. Heinrich

German Research Centre for Geosciences GFZ, Section 3.3, 14473 Potsdam, Germany

3.1.1 Abstract

Several macroscopic physical and chemical properties, such as rheology, elasticity, or transport properties are governed by grain boundary processes. An improved understanding of the structure and evolution of grain boundaries has thus become a key challenge in geosciences and material sciences. Here, we report the structure of *near* Σ5 (210)/[100] grain boundaries in $Y_3Al_5O_{12}$ (YAG), which were synthesised by the wafer direct bonding method. The produced grain boundaries were annealed at different temperatures, ranging from 673 to 1873 K. The grain boundaries annealed at different temperatures are not distinguishable based on their flatness and apparent cohesiveness in high resolution TEM (HRTEM) micrographs, but show a considerable step in their mechanical stability at around 1273 K, a temperature that corresponds to roughly half the melting temperature of YAG. This study further focuses on the effect of a slight misorientation of the two crystals on the grain boundary structure and we discuss if the boundary can reach a state of minimum energy configuration during annealing. Along the grain boundaries, we observed a long-range strain contrast with a periodicity of 40 nm, which has not been reported for high-angle grain boundaries so far. We conclude that this contrast is caused by faceting along the grain boundary plane, which is needed to achieve minimum energy configuration of the grain boundary plane.

3.1.2 Introduction

Our current understanding of grain boundaries mainly emerged from studies on metals and alloys (Gleiter & Chalmers, 1972; Carter & Föll, 1978; Föll & Ast, 1979; Carter et al., 1981; Cunningham et al., 1982; Sutton & Balluffi, 1995; Christophersen et al., 2001; Merkle et al., 2004; Randle, Rohrer & Hu, 2008). Beyond

that, grain boundaries in complex ionic compounds, such as ceramics, have been studied extensively starting in the early 80is till now (Ernst et al., 1999; S. B. Lee et al., 2003). Despite their importance for our understanding of several physical and chemical properties, for instance rheology, elasticity, or transport properties, grain boundary studies are still rare in earth sciences (e.g. Bons et al., 1990; Keller et al., 2008). During the last decades, element transport in natural materials has been brought in the focus of mineral and geosciences (Jaoul et al., 1991; Joesten, 1991; Abart et al., 2004; Abart et al., 2009; Milke et al., 2009; Schmid et al., 2009). Understanding and measuring element diffusion along single grain boundaries has become a key challenge. This increasing interest motivates our aim to produce well characteriseable grain boundaries over mm ranges.

It can be an expensive and time-consuming challenge to produce long-range interfaces with constant characteristics, for example using ultra high vacuum (UHV) bonding (Ganguly et al., 1998; M. J. Kim & Carpenter, 2002; Gemming et al., 2003). However, wafer direct bonding, also termed 'direct bonding' or 'fusion bonding', is a method to join two well polished material slices without glue, force, or ultra high vacuum at ambient conditions (Harendt et al., 1992; Pössl & Kräuter, 1999). The method is relatively simple and does not require sophisticated or expensive machines. It can be applied to most materials (Haisma et al., 1994; Tong et al., 1995) and allows for the production of any desired grain boundary orientation with an accuracy of about 0.5°. The bonding that is achieved at ambient conditions is relatively weak in comparison to metallic, covalent or ionic interactions in the volume of the crystals, but it strengthens during heating. Therefore, annealing at elevated temperatures is favourable for many applications. The interface strength depends on the surface energies and the bond strengths and it is generally quantified by crack-opening (Gösele et al., 1999).

In the past, the direct wafer bonding method was mainly applied to semiconductors or electronic devices (Maszara, 1991; Harendt et al., 1992), but has recently been adopted to geomaterials (Haisma et al., 1994; Heinemann et al., 2001; Heinemann et al., 2003; Heinemann et al., 2005). Heinemann et al. (2005) observed that synthetic grain boundaries in forsterite (Mg_2SiO_4) bicrystals formed after annealing

for 7 days at 673 K. At the scale of HRTEM, the grain boundary region was fully crystalline and no evidence for amorphous material at the grain boundary was reported. Further annealing for 48 h at 1923 K did not significantly change the grain boundary structure. So far, it is not fully understood at which temperatures the grain boundary achieves its maximum stability and if a random grain boundary is able to reach a minimum energy configuration during long annealing periods.

To address these questions, we synthesised a *near* $\Sigma 5$ (210)/[100] grain boundary in yttrium aluminium garnet (YAG) by using the direct wafer bonding method at different annealing temperatures. YAG bicrystals with a perfect $\Sigma 5$ (210)/[100] grain boundary have previously been synthesised using the UHV method (Campbell, 1996), which serves as a useful reference for this study.

Garnets crystallize in the highest symmetric space group $Ia3d$ of the cubic crystal system (bcc). In $Y_3Al_2Al_3O_{12}$ (YAG), yttrium occupies the large dodecahedral positions exclusively, whereas the aluminium is distributed between the octahedral and tetrahedral sites. The unit cell consists of 160 atoms corresponding to eight formula units (Kuklja & Pandey, 1999; Dobrzycki et al., 2004). It has an extremely high melting point of 2213 K (Caslavsky & Viechnicki, 1980) and is perfectly suited for this study because large stoichiometric crystals of high quality can be synthesised and polishing techniques have been adapted to YAG as it is used for many technological applications, such as solid state lasers. Furthermore, YAG is highly stable under the electron beam, which is prerequisite for extended exposure times to the electron beam during zone axis alignment to obtain high quality HRTEM images.

In this study, we monitor the relation between final boundary strength and annealing temperature in order to better constrain the required minimum annealing temperature that leads to a stable interface. Furthermore, we address the effect of a slight misorientation of the two crystals on the grain boundary structure and we test if the boundary reaches a state of minimum energy configuration during annealing.

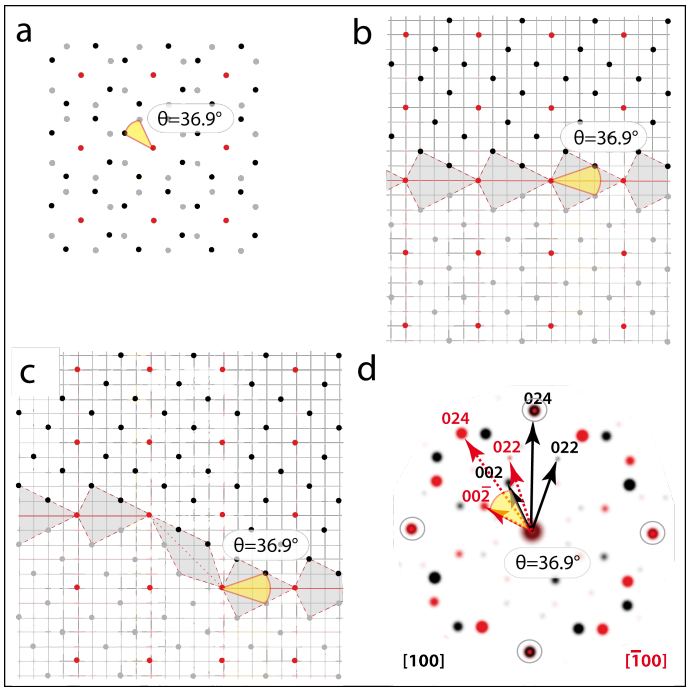

Figure 3.1: Sketch of the Coincidence Site Lattice (CSL). (a) The example shows the CSL (red) of a Σ5 coincidence site lattice that is produced by superimposing two lattices (grey and black) with a misorientation angle θ of 36.9°. (b) Sketch of a geometrical Σ5(210)/[100] grain boundary, which is a twin about the (210) plane. The tilt of $\theta = 36.9°$ about the common [100] direction is structurally equal to a twist boundary of 180° parallel to the (210) plane. (c) Same grain boundary plane as in (b), but faceted. No strain is generated as the step is between coincidence sites of the CSL. Additionally, the displacement shift complex (DSC) is indicated (square lattice in grey colour, see text for explanation). (d) Simulated diffraction pattern of the Σ5 (210)/[100] grain boundary. The coinciding diffraction spots are circled.

Grain boundary models

A minimum of five parameters, consisting of three Miller indices for the grain boundary plane <hkl> in the reference crystal and two rotational angles to describe the orientations of the respective grains, is required to fully describe a grain boundary. Alternatively, one angle and two sets of Miller indices (one that represents the grain boundary plane and one that gives the direction of the axis of the rotation) can be used. Most commonly, grain boundaries and crystal to crystal orientations are described by the coincidence site model (Gleiter & Chalmers, 1972; Chadwick & Smith, 1976; Sutton & Balluffi, 1995). In this model, two three-dimensional lattices are super-imposed and translated until they coincide at lattice sites (Fig. 3.1) and thereby generate a super periodicity or 'super lattice', which is referred to as the coincidence site lattice (CSL). The Σ-nomenclature is commonly used to describe the relation between the number of lattice points in the unit cell of a CSL and the number of lattice points in the unit cells of the generating lattices and is defined as:

$$\Sigma = 1/\mathrm{n}$$

where n is the fraction of the lattice points of the two super-imposed lattices that coincide. We emphasize that the Σ relation does exclusively define the crystal to crystal orientation. But two grains displaying a Σ-relation may be joined by a grain boundary plane with high energy. For each specific CSL, high interface coincidences and thus energetic minima only exist for certain grain boundary plane orientations which are likely to occur at the closest packed planes of the corresponding CSL (Rohrer et al., 2004; Rohrer, 2007).

A grain boundary that is not exactly at the plane of highest coincidence site density can reduce its energy by faceting. This can be achieved with or without inserting secondary grain boundary dislocations, but in both cases the total boundary area increases (Fig. 3.1c, see also Brandon et al. 1964). Faceting requires movements of atoms over short distances and thus sufficiently high temperatures. For the total free energy of a polycrystal, the grain boundary plane is of minor importance compared to the relative orientation of all the crystals towards each other.

Based on theoretical arguments, it is expected that two crystals that are close to a low energy crystal orientation relation will minimize their grain boundary energy by turning into a Σ-relation, which generally has low energy. However, this would require a movement of all the atoms inside one grain. Alternatively, the small misorientation could be overcome by superimposing a network of secondary dislocations to the present boundary, which is comparable to dislocations added to achieve the minimum energy grain boundary plane.

3.1.3 Methods

Bicrystal synthesis by direct bonding

YAG single crystal plates were mistilted by 3° parallel to the (210), which results in an angle of 93° degree between the [001] and our desired plane close to (210). Plates were cut and chemo-mechanically polished (CMP) with silica slurry. A KUGLER (KMS) interferometer was used for surface roughness measurements by determining the roughness average (Ra) values from the topography data of the computer-supported interference microscope. The final roughness of the crystal plates was about 0.34 nm.

The crystals were wet-chemically cleaned using a five step cleaning procedure in a clean room environment. In step one, a hydrogen per-oxide cleaning solution (pH∼6.5) at 353 K was applied, the second step was a per-iodic acid cleaning to decompose organic adsorbants. In steps three and four, the crystal surfaces were cleaned with acetone and isopropanol, respectively. Finally, the surface is saturated with pure adsorbed water. In order to synthesize a bicrystal, an initial contact between two clean crystals was established by applying a slight pressure with tweezers. The initial bonding was further strengthened by heating in a vacuum furnace at 673 K and 10 Pa for 1 week. However, the achieved bond is mechanically easily separable. To increase the bonding strength additional annealing runs at 873 K, 1073 K, 1273 K, 1473 K, 1723 K and 1923 K for 48 hours each were performed. A detailed description of the bonding method is given by Heinemann et al. (2001).

The Σ5 (210)/[100] grain boundary in cubic materials, is a tilt boundary of 36.9° about the bicrystals' common [100] direction, which is structurally equal to

a twist boundary of 180° parallel to the (210) plane. The exact Σ5 (210)/[100] grain boundary has previously been synthesised in YAG using the UHV-technique (Campbell, 1996). In contrast, we produced a *near* Σ5 (210)/[100] grain boundary with direct bonding. We rotated the crystal wafers by 185° with a misfit of 3° to the (210) plane, thereby inducing an additional tilt of 6° between the [100] and the [$\bar{1}$00] direction. The results are shown in the lattice fringe images of figure 3.2. The optical isotropy of garnet prohibits a quantification of the orientation relation of the two crystals with optical microscopy. The misorientation of the two crystals with respect to the Σ5 (210)/[100] grain boundary is measured with an accuracy of about 0.1 degree with the TEM by using the alpha and beta tilts of the stage. First, the [100] direction of one crystal is aligned with the incident beam, followed by the [$\bar{1}$00] direction of the second crystal. The measured angle set is α = -2.86°, β = 1.43° and α = -2.52°, β = 8.08°. The total misalignement between [100] and [$\bar{1}$00] direction is calculated by a rotational matrix conversion to be 6.5° (±0.1°). Already short low temperature anneals bring the grain boundary plane parallel to the (210) plane.

Finally, we can fully describe the grain boundary as a *near* Σ5 (210)/[100] grain boundary, where the boundary plane lies in the (210) plane of both crystals. The rotation about the [100] direction is 36.9°, additionally, a rotation of 6.5° about the [210] direction is present.

Sample preparation

Lamellae for TEM (15×8×0.1μm^3) were prepared using the Focused Ion Beam (FIB) technique (Overwijk et al., 1993; Phaneuf, 1999; M. R. Lee et al., 2003; Wirth, 2004). To obtain high quality HRTEM images, one sample was prepared at the application laboratory FEI Company, Eindhoven, Netherlands by using an in-situ lift out method in the Helios Nanolab 600. A chunk of the material was removed from the bulk sample by using the FIB to remove material around it. The chunk was then transferred to the grid by attaching an Omniprobe to the lamella using FIB induced Pt deposition. Once attached to the grid, final thinning was performed on the lamella, initially at an acceleration voltage of 30 kV, and finally at 2 kV. Another lamella was prepared using a two-beam focused ion beam (ZEISS NVision40 Argon)

instrument with an implemented low energy Ar-ion gun (Penning Ion Gauge, PIG). This method overcomes the problem of the amorphous layer forming during FIB sample preparation by Ga-ion implantation into the sample. Low voltage Ar-ion polishing with an acceleration voltage of 500 eV is suitable to remove the amorphous layer together with the implanted Ga from the FIB-lamellae surfaces.

TEM

A Tecnai F20 X-Twin TEM was operated at 200 kV acceleration voltage with a field emission gun (FEG) as electron source. The TEM is equipped with a post-column Gatan imaging filter (GIF Tridiem). All of the TEM images presented here are energy-filtered images applying a 10 eV window to the zero loss peak. The Gatan Digital Micrograph software was used for the analyses of the energy filtered transmission electron micrographs (EFTEM). The ring mask method was used for fast Fourier transform (FFT) analysis to prevent lattice fringe extrapolations (Pradère et al., 1988; Pradère & Thomas, 1990).

3.1.4 Results

Bicrystal synthesis

The grain boundary formed by direct bonding is homogenous over a length of at least 10 μm. This minimum length is derived from TEM investigations of FIB-milled lamellae with the dimensions 15×10 μm^2. The grain boundaries that we annealed at different temperatures (673 – 1873 K, tab. 3.1) are not distinguishable based on their flatness and apparent cohesiveness (Fig. 3.2). However, the grain boundaries synthesized below 1273 K are mechanically separable (compare tab. 3.1, Fig. 3.1 to Fig. 3.3). After annealing at 1273 K or at higher temperature, bonding is strong enough that upon stress the bicrystals fracture at other locations than the interface. We also observed that the forsterite bicrystals synthesized at 673 K by Heinemann et al. (Heinemann et al., 2005), which show comparable lattice fringe images, are mechanically separable as well.

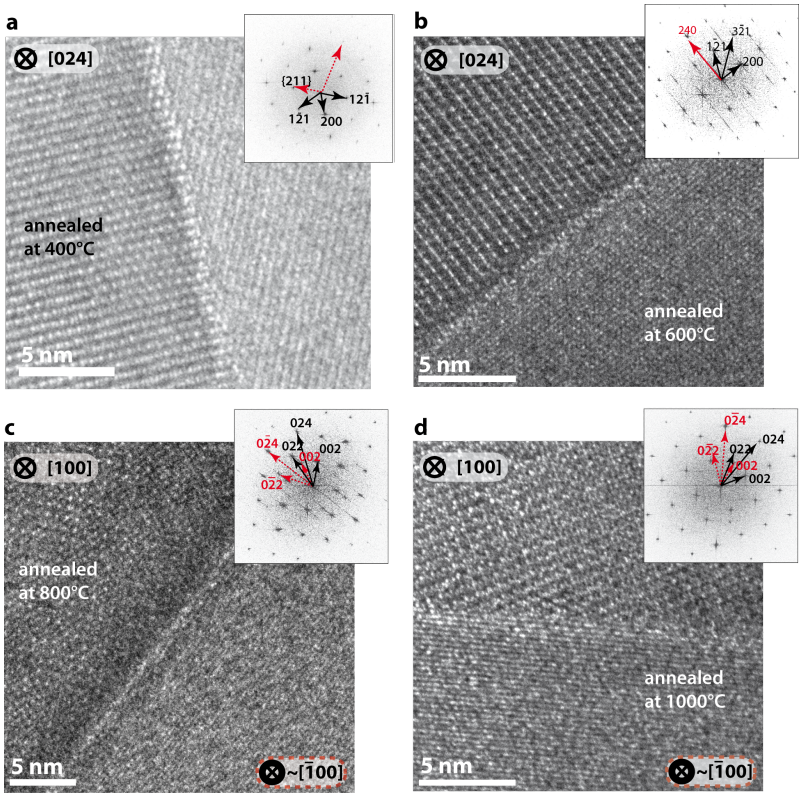

Figure 3.2: Lattice fringe images of grain boundaries synthesized at 673, 873, 1073 and 1273 K (a-d). The grain boundaries bonded at 673, 873 and 1073 K (a, b, c) can be easily separated mechanically, even though no apparent differences can be observed between their lattice fringe images and the one corresponding to the grain boundary synthesized at 1273 K (d). At all stages, the lattice fringes of the opposing crystals touch each other at the interface and no amorphous material or material with different structures was observed. Images (a) and (c), with a misorientation angle θ relative to the exact $\Sigma 5$ (210)/[100] of $\sim 8°$, as well as (b) and (d) (θ $\sim 6.5°$) have been taken along different zone axes because the bicrystals have slightly deviant orientations. The varying image quality results from the strongly differing thicknesses of the respective TEM lamellae.

annealing hours at K							
	673 K	873 K	1073 K	1273 K	1723 K	1873 K	Separable
2 Garnet	168						Yes
3 Garnet	168	48					Yes
4 Garnet	168		48				Yes
5 Garnet	168			48			No
6 Garnet	168				48		No
7 Garnet	168					48	No
1 Olivine	168						Yes

Table 3.1: Samples and corresponding bonding conditions.The primary annealing time was one week at 673 K. Additionally, some crystals were annealed for 48 hours at varying temperatures. All anneals were done in air. The olivine has previously been synthesized (Heinemann et al., 2005).

Microstructure and orientation relation of the grain boundary

In the following, only the bicrystal synthesized at 1273 K with a misorientation of 6.5° with respect to the perfect Σ5 (210)/[100] will be discussed. The grain boundary synthesized is thus a *near* Σ5 (210)/[100] grain boundary, as shown in the lattice fringe image of Fig. 3.3. The diffraction pattern (inset in Fig. 3.3) confirms the rotation of ∼36.9° of the two crystals with respect to each other. The thinnest parts of the studied lamella showed a relative thickness of less than 0.3 times the inelastic mean free paths, which was extracted with electron energy loss spectroscopy (EELS) using the Log-Ratio method.

Grain boundary topography

This section describes TEM observations on the 10-100 nm length scale. TEM images and high resolution images show a long-range periodic diffraction contrast where dark and white contrasts alternate along the grain boundary (Fig. 3.4, Fig. 3.5; we will henceforth speak of extended strain contrast to use the terms common in literature (Vargas et al., 1997; Tsu et al., 1998)). The image of the boundary plane is sharp and very narrow indicating that it is edge-on throughout the whole lamella thickness (up to ∼80 nm, Fig. 3.4a). The long-range strain contrast has a periodicity of 40 nm and extends approximately 40 nm into the opposing grains.

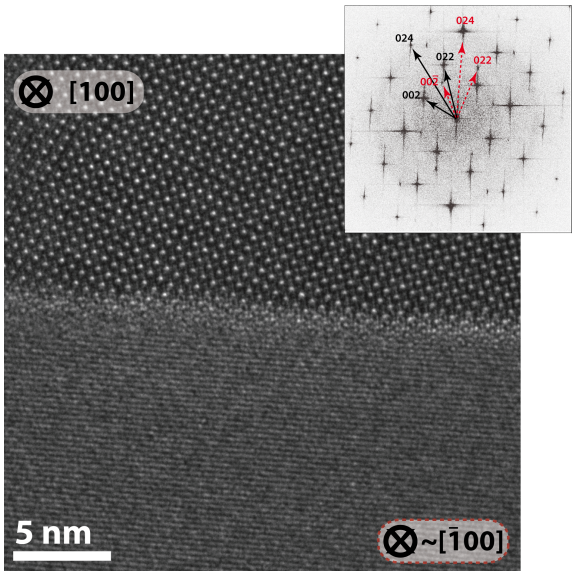

Figure 3.3: HRTEM image of the *near* Σ5 (210)/[100] grain boundary. The [100] direction of the upper crystal is parallel to the incident beam. [100] is the common axis of a perfect Σ5 twin boundary. As the misorientation with respect to this orientation is small, both crystals show the diffraction pattern of the [100] zone axis rotated by 36.9°. Nevertheless, the lower crystal is not perfectly aligned in [100]. The TEM-lamella is very thin (see text) and the diffraction spots, with their relatively large deviation vector $\mathbf{s}$ ($\mathbf{g} = \Delta\mathbf{k} + \mathbf{s}$), are still visible in the diffraction pattern, but with reduced intensities (compare to simulated diffraction pattern in Fig. 3.1). In the lattice fringe image only the (240) planes of the lower crystal are visible.

The periodicity is insensitive to tilting (Fig. 3.4a-d), whereas, tilting gives rise to an additional moiré pattern, i.e. an interference pattern which is created, in the specific case, by overlaying two grids at an angle. It changes its periodicity depending on the inclination of the boundary plane towards the incident beam (Fig. 3.4b-d). The moiré pattern interferes with thickness fringes arising from the wedge-shaped projection of the inclined grain boundary plain.

Lattice fringe micrographs reveal steps at the interface. Steps along the grain boundary plane ((042), equivalent to (210)) are observed (Fig. 3.5a). They extend over at least two d-spacings of the (042) plane, corresponding to 0.536 nm. They are of minor height and occur accumulated, thereby forming facets with shallow slopes with a length of about 20 nm. No dislocations were identified. Comparable structures are observed at thicker parts of the sample (Fig. 3.5b), where most of the grain boundary area lies in the (042) plane, except for some facets. These facets are spatially related to the extended strain contrast (dark contrast in the image). Furthermore, the lattice left and right of the facet structure is distorted, causing a slightly blurred image. The step-high is approx. 1.1 nm ($4\times d_{(042)}$) on the left and approx. 2.1 nm ($8\times d_{(042)}$) on the right site of the facet in Fig. 3.5. The jump from one platform of the grain boundary plane to the next is indefinite and blurred.

3.1.5 Discussion

Direct bonding – atomic bond formation

In our experiments, the grain boundary in YAG reaches maximum stability only at temperatures T above about 1273 K, which corresponds to a homologous temperature $T_H = T/T_M$ of 0.58 (the melting temperature T_M of YAG is ~2213 K). This also holds true for crystalline silicon with a melting temperature of 1687 K, where complete bonding via surface diffusion of Si atoms occurs above 973 K (Tong & Gösele, 1999), which also translates to $T_H = 0.58$. Heinemann et al. (2005) observed using HRTEM that the grain boundary structure in synthetic olivine bicrystals did not differ between annealing temperatures of 673 and 1923 K. The fact that the olivine bicrystals synthesised at 673 K are mechanically easily separable (as reported in this study) is in good agreement with our observations for YAG. Consequently, we

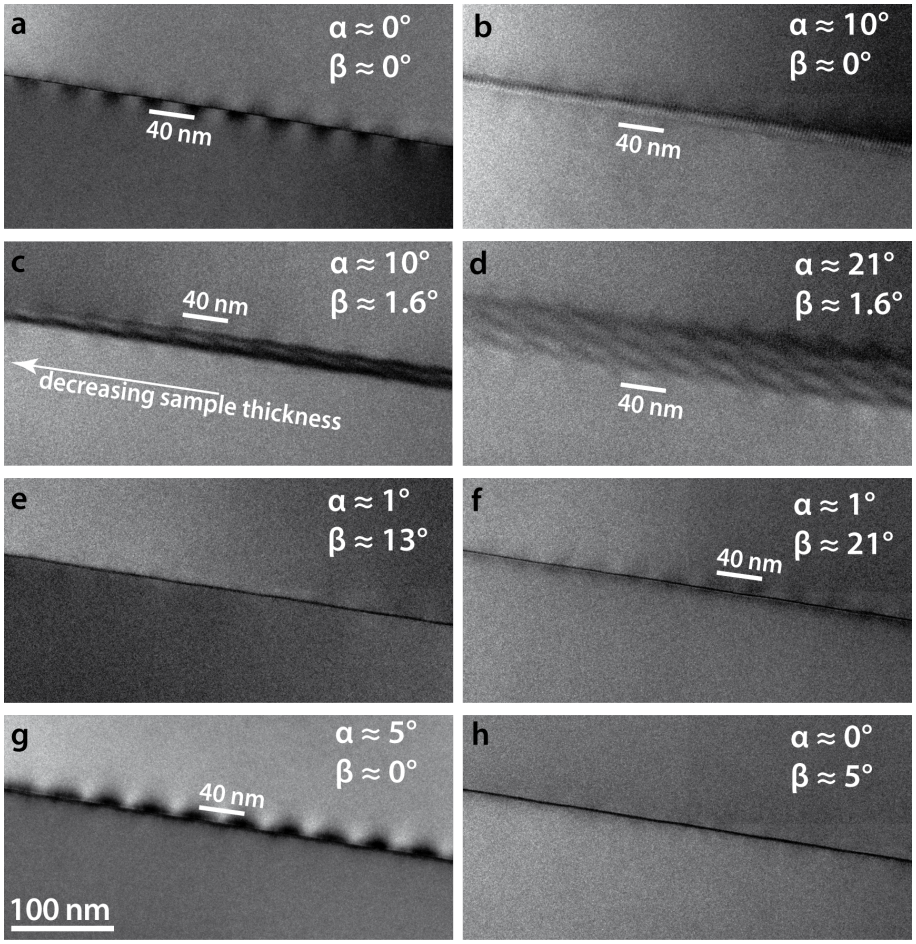

Figure 3.4: TEM bright field images of the bicrystal grain boundary. The sample thickness decreases towards the left margin of all the images. (a) The orientation is the same as in figure 3.4 (α and β tilt close to 0°). The periodicity of the dark contrast along the grain boundary is about 40 nm. The distance from a dark contrast maximum in one crystal to a dark contrast maximum in the other crystal is about 20 nm. (b) The same sample, but tilted by $\alpha = 0°$ $\beta = 10°$. The periodicity observed in (a) is still visible, but now interferes with a moiré pattern that is formed by the two superimposed crystal lattices of the bicrystal. To illustrate this effect, the sample is further tilted as shown in (c) and (d). (c) The sample is tilted by $\alpha = 10°$ and $\beta = 1.6°$. (d) The sample is tilted by $\alpha = 21°$ and $\beta = 1.6°$. Note that the pattern in (d) could be misinterpreted as a network of secondary interface dislocations. (e) The sample is tilted by $\alpha = 1°$ and $\beta = 13°$. The periodic contrast completely disappears. (f) The sample is tilted by $\alpha = 1°$ and $\beta = 21°$. The periodic strain contrast is again visible in both crystals. (g) The sample is tilted by $\alpha = 5°$ and $\beta = 0°$. The periodic strain contrast is visible only in the upper crystal, but very pronounced. (h) The sample is tilted by $\alpha = 0°$ and $\beta = 5°$. The contrast of the extended strain fields is again absent.

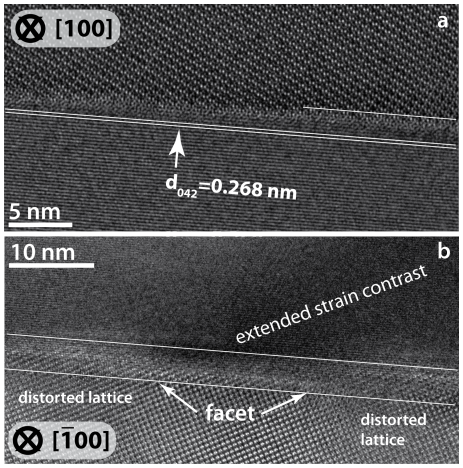

Figure 3.5: (a) The same sample as in figure 3.3, but with a different defocus. The actual location is very close to the edge and has relative thickness of less than 0.3 inelastic mean free paths (details above). A step/facet is present along the grain boundary. Lines parallel to the (042) planes, shifted downwards and upwards to prevent coverage of the real structure, are shown for illustration. The step extends over at least two d-spacings of the (042) plane, corresponding to 0.536 nm. (b) Lattice fringe image of the bicystal at a thicker part of the sample, where the zone axis of the lower crystal is oriented parallel to the incident beam. Most of the grain boundary plane area lies in the (042) plane except for a facet which is spatially related to the extended strain contrast represented by the dark contrast. Furthermore, the lattice on both sides of the facet is distorted, causing a slightly blurred image.

suggest that direct bonded samples should be annealed at temperatures of about 60% of T_M in order to obtain a grain boundary with maximum stability.

Periodic strain fields

A possible relation between the primary surface properties of the educt-materials and the periodic strain fields must be evaluated. Wafers are typically affected by non periodic mm-scale surface morphology (Maszara et al., 1991). Additionally, our wafers had a surface roughness of about 0.34 nm as determined by interferometry. Both surface unevenness deviate from the observed strain field periodicity of 40 nm by several orders of magnitude and do not have any periodicity. A relation between the periodic strain fields and the primary surface properties of the wafers used for direct bonding is thus unlikely. This conclusion is supported by previous studies that report comparable extended periodic strain fields in different materials; the grain boundaries were synthesized by different methods, including direct bonding (Heinemann et al., 2005), directional solidification (Tsu et al., 1998) or they were grown from a flux (Vargas et al., 1997). The wavelengths of the observed periodic strain fields range from 35 to 180 nm. They are not correlated to the misorientation angles as shown for tilt angles ranging from 2 to 31° (Tsu et al., 1998). Tsu et al. (1998) observed a spatial relation between the periodic strain fields and the facets, whereas Heinemann et al. (2005) did not. However, it appears that they are often related to saw-tooth like facet structures (e.g. Tsu et al., 1998; Phaneuf, 1999). Nano-scale waviness has also been observed in olivine (Johnson et al., 2004). All those observations have been obtained from low angle tilt grain boundaries, and have not been reported for perfect or near Σ-orientations (Campbell, 1996; S. B. Lee et al., 2003).

Our tilt experiments prove that the measured 40 nm periodicity of the strain contrast (Fig. 3.4) is an intrinsic property of the grain boundary. The observed contrast pattern in figure 3.4d can be assigned to a rotational moiré pattern and is not caused by a network of secondary grain boundary dislocations because the horizontal and vertical distances between dark and bright contrast change with sample tilt due to projection. Additionally, the pattern interferes with thickness fringes arising from

the wedge-shaped projection of the inclined grain boundary plane. If the contrast of the periodic strain fields is visible depends on the sample orientation relative to the incident electron beam (Fig. 3.4). During tilting, the imaging vector **g** and the deviation parameters change, thus modifying the amplitude of the diffracted beam and the direct beam. If dislocations were present, their dislocation line u would be parallel to the imaging vector **g** in figure 3.4e, h. However, the absence or presence of dislocations is hard to prove because of limitations in the α and β ($\pm 30°$) tilts. In addition, the orientation of our FIB lamella might be unfavourable. It is impossible to follow a Burgers circuit in the HRTEM images, because one crystal is always out of the ideal zone axis. The observed strain fields are large compared to usual dislocation strain fields and it is unlikely that single dislocations account for such large strain fields. Nevertheless, dislocations with delocalized cores, smeared out in the plane of the grain boundary, could cause extended strain fields.

However, steps are directly observed (Fig. 3.5) in the grain boundary plane area, which mainly lies in the (210) plane. Their heights range from ~0.5 nm to ~2.1 nm, which are multiples of $d_{(042)}$ = 0.268 nm. They correlate spatially with the periodic contrast of the extended strain fields (Fig. 3.5b). The association between steps and strain contrast becomes only visible in thicker parts of the sample (Fig. 3.5b), whereas the strain contrast decreases drastically as the sample thickness drops below a thickness of about one extinction length (Fig. 3.5a). The change in contrast formation with decreasing sample thickness can be described applying the dynamical theory in thicker parts of the lamella and the kinematic theory for contrast formation in very thin parts. The central point is that as the sample thickness decreases the jump from one platform of the grain boundary plane to the next is much sharper. Hence, a component of the facet structure extends in the third dimension and could be responsible for the extended strain fields. The facet structure could also include dislocations, discontinuities or disconnections to a small extend in the plane of the boundary (Pond, 1989; Lartigue-Korinek et al., 2008). But as the additional misfit is tilt in character we would expect them to be mainly out of the plane of the grain boundary. Using two beam imaging with the {240} coincidence diffraction spots, we did not detect dislocations with a Burgers vector belonging to the CSL.

The facets seem to generate a wavy interface (Fig. 3.4e, h; Fig. 3.5b), similar to a low amplitude saw-tooth structure. The observed facets and the orientation of the grain boundary plane strengthen the argument that small misorientations of the grain boundary plane relative to a low Σ-plane orientation are adjusted by inserting steps, which is energetically favoured over facet-free boundaries with random grain boundary plane orientations. A superimposed dislocation network, during relaxation, could then accommodate the stress generated by the overall misorientation.

Based on theoretical considerations (e.g. Brandon, 1966), a bicrystal with an orientation relation close to a Σ-orientation should decrease its total free energy by introducing grain boundary dislocations with a Burgers vector of the DSC lattice that belongs to the Σ-orientation. The dislocation-free parts would then be in Σ-orientation and the mismatch would be compensated by the grain boundary dislocations (sketch in Fig. 3.6). In our case, the $[\bar{1}00]$ zone axis should then be tilted parallel to the [100] of the second crystal; necessarily the grain boundary dislocations must than have a Burgers vector perpendicular to the boundary plane. However, this was not observed. Similarly, Randle, Rohrer and Hu (2008) used Electron Backscattering Diffraction (EBSD) and observed subtle changes in the plane distribution as a consequence of a long low temperature anneal in hexagonal titanium alloy, but the pure CSL relation also stayed nearly unchanged. Further studies are needed to find out if the pure CSL relation can change at all.

3.1.6 Conclusion

For the first time, periodic extended strain fields in relation with a *near* Σ grain boundary have been observed. They are an intrinsic property of the grain boundary. We interpret them to arise from facets at the grain boundary plane, which compensate a slight off-plane component of the (210) grain boundary plane. Another interpretation is that the bicrystal started to adjust for its off-Σ relation by introducing secondary grain boundary dislocations in order to compensate the misfit rotation of $\theta \sim 6.5^\circ$ about the [210] direction.

This well characterized grain boundary provides an excellent starting material for further studies, for example diffusion experiments along single grain boundaries

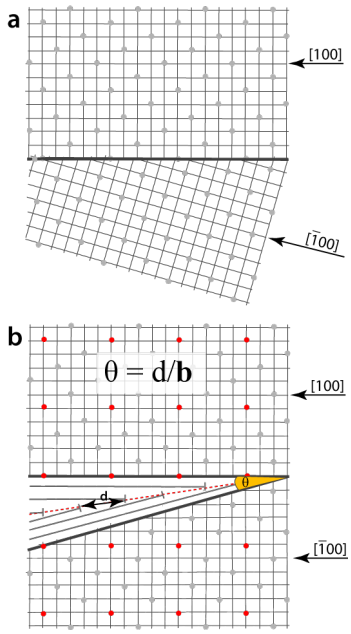

Figure 3.6: (a) The tilting which is needed to turn a near Σ-crystal orientation to a low Σ-orientation can be achieved by introducing dislocations similar to those of a low angle boundary to the present boundary. (b) The additional misorientation angle for small angles is given by θ = d/**b** with dislocations spacing of the DSC lattice d, and the Burgers vector of the DSC lattice dislocations **b**. The dislocations in (b) could be distributed between the lower and the upper crystal, thereby generating a smoothly waved interface. The different contrasts that we observe for the two crystals in our experimental TEM images are caused by the fact that the atom columns of the upper crystal are parallel to the incident beam, whereas the atom columns of the lower crystal are not.

(Hartmann et al., 2008; K. Marquardt et al., submitted).

Acknowledgements

The authors would like to thank FEI Company in Eindhoven for preparing a FIB sample which was used for the HREM image of figure 3.4 as well as for figures 3.5 and 3.6. We thank Carl ZEISS NTS GmbH in Oberkochen, Germany, for sample preparation with low energy Ar-ion polishing. Furthermore, KH highly appreciates the hours of in-depth discussion with Hauke Marquardt and likes to thank him for his critical opinion of the manuscript.

Volume Diffusion of Ytterbium in YAG: Thin-film Experiments and Combined TEM – RBS Analysis

by K. Marquardt (née Hartmann), E. Petrishcheva, R. Abart, E. Gardés, R. Wirth, R. Dohmen, H.-W. Becker, and W. Heinrich

accepted for *Physics and Chemistry of Minerals*, DOI: 10.1007/s00269-010-0373-4

3.2 Volume Diffusion of Ytterbium in YAG: Thin-film Experiments and Combined TEM – RBS Analysis

K. Marquardt (geb. Hartmann)[1], E. Petrishcheva[2], R. Abart[2,3], E. Gardés[1], R. Wirth[1], R. Dohmen[4,5], H.-W. Becker[6], W. Heinrich[1]

[1]*German Research Centre for Geosciences GFZ, Section 3.3, 14473 Potsdam, Germany*

[2]*Freie Universität Berlin, Institute for Geological Sciences, 12249 Berlin, Germany*

[3]*Department for Lithosphere Research, University of Vienna, Vienna, Austria*

[4]*Institut für Geologie, Mineralogie und Geophysik, Ruhr-Universität, 44780 Bochum, Germany.*

[5]*now at: University of Bristol, Dept. of Earth Sciences, Queen's Road, Bristol, UK*

[6]*Fakultät für Physik und Astronomie, Ruhr-Universität Bochum, 44780, Germany*

3.2.1 Abstract

In this study, we address volume diffusion of ytterbium in yttrium aluminium garnet (YAG) using thin-film single crystal diffusion couples. We employ analytical transmission electron microscopy (ATEM) as a tool for combined microstructural and microchemical analysis and compare the results to Rutherford backscattering (RBS) analysis. Given the high spatial resolution of the method, we focus on microstructural changes of the thin-film diffusant source during the diffusion anneal. We evaluate the potential influence of the associated changes in its transport properties on the evolution of concentration profiles in the single crystal substrate. This approach allows us to test the reliability of determination of volume diffusion coefficients from thin-film diffusion experiments. We find that for the chosen experimental setting the influence of thin-film re-crystallization is small compared to the experimental uncertainty and good estimates for the volume diffusion coefficients of Yb in YAG can be obtained using standard assumptions. Both Yb-concentration profiles analyzed with ATEM and with RBS give similar results. At 1450°C and 1 bar, we infer $\log D_{Yb}$ (m^2/s) values of -19.37 ± 0.07 (TEM) and -19.84 ± 0.02 (RBS). Although the change in thin-film transport properties associated with successive crystallization during the diffusion anneal does not play a major role for our experimental setup, this effect cannot generally be ignored.

3.2.2 Introduction

A large part of the Earth's Interior is comprised of solid materials with a wide range of chemical compositions. Element partitioning between coexisting phases is pressure and temperature dependent. If rocks are exposed to changing physical and chemical conditions, they tend to adapt their compositions to achieve new equilibrium states. Chemical equilibrium can be achieved by element diffusion between or within the solid phases. A quantitative understanding of diffusion processes can thus improve our apprehension of the petrogenetic memory of natural rocks, including disequilibrium phenomena such as chemical zoning or reaction textures (Ganguly et al., 1998; Béjina et al., 2003; Abart et al., 2004; Gardés et al., 2006; Gardés et al., 2007; Abart et al., 2009; Gardés & Montel, 2009; Milke et al., 2009; Schmid et al., 2009). Furthermore, diffusion rates in minerals are related to a number of physical properties, such as electrical conductivity (e.g. Constable & Duba, 2002; Dobson et al., 2008), and may have an important influence on geological processes, including mantle rheology (e.g. Jaoul et al., 1991; Jaoul & Béjina, 2005). Diffusion in solids is rather slow and the accurate determination of diffusion coefficients has posed an experimental and analytical challenge over years. Several experimental studies used bulk exchange between a fluid or a melt as diffusant source and solid grains and analyzed shifts in bulk composition of the fluid/melt and of the solid particles to study diffusion. In this case, no information on the time evolution of concentration profiles is attained and the extraction of diffusion coefficients from bulk measurements necessarily relies on a number of idealizing assumptions.

Another approach has been to analyze concentration profiles of a diffusant, for example the radio-tracer method. The major problem with this method has been the need for sufficiently long diffusion profiles that allow for accurate concentration determinations with the required spatial resolution. Long diffusion profiles, in turn, require long annealing times, which is often not practical on laboratory time scales.

For refractory materials such as YAG, where the diffusion coefficients are very small (on the order of 10^{-19} – 10^{-23} m^2/s at temperatures around 1500°C), this approach can only be applied, if the diffusant concentrations can be analyzed at very high spatial resolution (Jiménez-Melendo et al., 2001). To produce diffusion

couples in miniaturized geometry, thin-films are usually used as diffusant source and the short (< 5 μm) diffusion profiles produced in thin-film experiments are commonly measured by Rutherford backscattering (RBS) or secondary ion mass spectrometry (SIMS) (Feldman & Mayer, 1986; Jaoul et al., 1991; Young Chul et al., 2006). However, in many of these diffusion studies the thin-film has a different composition and is comprised of a different phase than the substrate. Due to the small spatial extent, potential reaction between the thin-film and the substrate are difficult to identify with RBS or SIMS.

A recently established approach is to analyze diffusion from thin-film diffusant sources, which were deposited by pulsed laser deposition (PLD) onto a single crystal substrate. Analytical transmission electron microscopy (ATEM) was applied for elemental analyses (Dohmen et al., 2002). This method allows for analyzing concentration profiles and simultaneously provides information on sample structure and texture at a high spatial resolution. The production of thin-film/substrate diffusion couples with simple, time invariant geometry and microstructure is a prerequisite for 'clean' diffusion experiments. To maintain the initial geometry and microstructure, the thin-film must be thermodynamically stable together with the substrate at the conditions of the diffusion anneal. By the use of TEM, this can be tested efficiently and any disturbing effects such as reaction between source and substrate can readily be detected.

If net transfer reactions or microstructural changes at the substrate/thin-film interface can be excluded, diffusion coefficients can be extracted by fitting a diffusion model to the measured concentration-depth profiles. The choice of the appropriate diffusion model depends, among others, on the diffusion characteristics of the thin-film. Due to the minute spatial extension of the thin-film, it is difficult to obtain diffusion profiles from within the thin-film. Many studies therefore rely on simplifying assumptions regarding its transport properties. Some authors used a constant diffusion coefficient for the thin-film D_{film}, which was chosen to be 1-2 orders of magnitude higher than the diffusivity of the substrate D_{sub}, this was in accordance with the polycrystalline nature of the film (Dohmen et al., 2002; Dohmen et al., 2007). Others assumed that D_{film} and D_{sub} are equal and constant throughout the

experiment (Gardés et al., 2006; Gardés et al., 2007). None of these studies addressed, however, the potential influence of structural changes within the thin-film on its transport properties. Temperature-induced structural changes in the thin-film may occur during the diffusion anneals and may continuously change its transport properties. Such transient behavior of the diffusant source may potentially influence the resulting concentration profiles and needs to be accounted for when extracting diffusion coefficients from measured diffusion profiles.

In this study, we determined diffusion profiles by both ATEM and by RBS and find good agreement between the two methods. In addition to the concentration-depth profiles, TEM simultaneously provided information on sample structure and texture as well as an excellent 'depth' resolution (2-D resolution on an electron transparent lamella cut perpendicular to the sample surface) using focused ion beam (FIB). We used this additional capability to monitor the change in thin-film internal microstructure at the nanometer-scale in temperature-time-space. The derived information is included in numerical models and the results are compared to simple analytical solutions. This allows us to evaluate the influence of the changing thin-film properties on the calculated diffusion coefficients.

3.2.3 Materials and Methods

Sample material

Experiments were carried out using well-studied $Y_3Al_5O_{12}$ (YAG) single crystals (Yin et al., 1998; Lupei et al., 2001; Weber & Abadie, 2001; Dobrzycki et al., 2004; Hartmann et al., 2010), where Yb-Y interdiffusion data have already been acquired by different methods such as RBS and SIMS (Cherniak, 1998; Jiménez-Melendo et al., 2001; Peters & Reimanis, 2003).

Since the pioneering work of Geusic et al. (1964), neodymium-doped yttrium aluminum garnet (Nd:YAG) has become a well-known high-performance laser material. Since then, many other rare earth elements (REE) have been used as dopants to achieve the desired lasing characteristics, including Yb (Ikesue et al., 1996; Yin et al., 1998; Lu et al., 2000; Lupei et al., 2001; Lu et al., 2002; Ikesue & Aung, 2006; Pavel et al., 2006). YAG single crystals are generally grown using the Czochralski

method (Czochralski, 1918). In YAG, Y occupies the large dodecahedral positions exclusively, whereas the Al is distributed between the octahedral and tetrahedral sites. Thus the formula is $Y_3Al_2Al_3O_{12}$, which is commonly written as $Y_3Al_5O_{12}$. The unit cell contains 160 atoms corresponding to eight formula units (Kuklja & Pandey, 1999). Yb in the garnet structure has the same valence (3+) as Al and Y and its ionic radius is close to that of Y (∼3% difference) (Shannon, 1976). A complete solid solution exists between YAG and $Yb_3Al_5O_{12}$ (YbAG). However, the incorporation mechanism is not fully understood (Lupei et al., 2001). Besides its importance in materials sciences, the structural similarities between aluminate and aluminosilicate garnets may provide a key for a better understanding of diffusion in natural garnets where a major investigation problem is the difficulty in controlling their purity and stoichiometry.

Diffusion Experiments

Diffusion experiments were performed in thin-film geometry (Fig. 3.7). PLD was used to deposit Yb doped YAG thin-films on a pure YAG-crystal. The principle of the method and the detailed experimental setup for the deposition have been published elsewhere (Dohmen et al., 2002; Chrisey & Hubler, 2003). We used a Czochralski grown Yb:YAG single crystal ($Yb_{1.149}Y_{1.736}Al_{5.115}O_{12}$) as source material (target) for the deposition, see H. Marquardt et al. (2009) for details on the synthesis and characteristics. The samples were heated in vacuum (up to 620°C) prior to deposition to degas volatile adsorbents from the polished surface. The employed laser operated at a wavelength of 193 nm and it was pulsed at a frequency of 10 Hz, the laser flux was about 1 J/cm^2. The thin-film thicknesses varied between 30 and 100 nm for RBS measurements and 150 and 400 nm for TEM experiments. To prevent chemical exchange between the thin-film diffusant source and the substrate during thin-film preparation, the thin-film was deposited on a 'cold' substrate, i.e. the substrate was kept at room temperature. As a consequence an amorphous thin-film was produced.

Diffusion anneals were carried out in a high temperature furnace at temperatures in the range of 1720 to 1730 K and ambient atmosphere (table 3.2). The

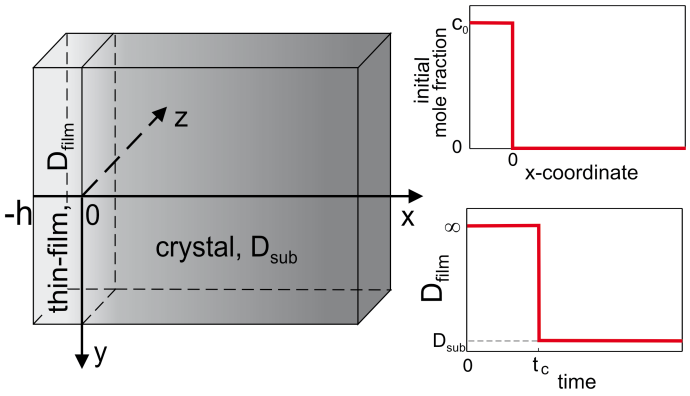

Figure 3.7: Left: system geometry. Right: initial mole fraction of Yb atoms versus coordinate (upper figure) and the Yb diffusion coefficient in the thin-film versus time (lower figure), where crystallization occurs at $t = t_c$.

temperature was measured with three thermocouples in different positions, where one thermocouple was next to the sample to monitor thermal gradients within the furnace.

Transmission Electron Microscopy (TEM)

TEM lamellae ($15\times8\times0.1$ μm^3) were prepared using the FIB technique (Overwijk et al., 1993; Phaneuf, 1999; M. R. Lee et al., 2003; Wirth, 2004). This method is capable of preparing samples with constant thickness, which is required to calculate element ratios directly from energy dispersive x-ray spectroscopy (EDS) data. We used analytical and energy-filtered high resolution TEM (ATEM, HRTEM) on a Tecnai F20 X-Twin TEM operated at 200 kV with a field emission gun (FEG) as electron source. The TEM is equipped with a post-column Gatan imaging filter (GIF Tridiem). All of the TEM images presented are energy-filtered images, where a 10 eV window was applied to the zero loss peak. The Gatan Digital Micrograph software was used for the analyses of the energy filtered transmission electron micrographs (EFTEM).

ATEM was performed with an EDAX X-ray analyzer equipped with an ultra thin window. The intensities were measured during a counting time of 100 s in scanning transmission mode (STEM). The incident electron beam was focused to a diameter of 3.8 nm. To reduce the effective current density and minimize mass loss and

Exp. No	Thin-film thickness [nm]	annealing time [min]	temperature [K]	investigation method	log D (m^2/s)
1	185	1445	1723	TEM	-19.37 ± 0.07
2	45	132	1723	RBS	-19.84 ± 0.02
3	185	5	1723	TEM	*a
4	185	10	1723	TEM	*a
5	200	20	1729	TEM	*a
6	225	40	1723	TEM	*a
7	350	120	1720	TEM	*a

Table 3.2: Experimental details and extracted diffusivities. Diffusion profiles produced in experiments number 1 and 2 are shown and compared in figure 3.10. *a: Profiles were too short to extract diffusivities. All experiments were useful to determine the changes in thin-film texture and crystallinity. The crystallisation progress is depicted in figure 3.8, where experiments 1, 5, 6 and 7 are shown.

irradiation damage during data acquisition, the electron beam was scanned over a pre-selected window of 20×40 nm^2. The sample was inclined towards the detector by an angle of 15-20°. The thin-film/substrate interface of the sample was oriented approximately parallel (within 2-5°) to the detector axis and the incident beam direction to avoid artefacts that might arise from analytical mixing information along planar defects (Williams & Carter, 1996). The diffusion distance perpendicular to the interface was measured with respect to the surface or purposely 'burned' holes fabricated prior to profile measurements, because contamination which could elsewise be used (Meissner et al., 1998) was minor. We avoided crystal orientations where strong diffraction occurs such as two-beam (Bragg) or in-zone-axis orientations to circumvent potential bias of EDS analysis due to electron channelling.

The background was subtracted from each TEM-EDS spectrum using a 2nd order polynomial, where the parameters were adjusted to obtain the best least-square fit to the background before and after each relevant peak. Furthermore, we measured zero-Yb spectra to obtain an average value for the background noise in our EDS measurements. The noise was then subtracted from each spectrum. Integrated X-ray intensities of Yb ($L_{\alpha,\beta}$) and Y ($L_{\alpha,\beta}$) were used to calculate the intensity ratio I_{Yb}/I_Y.

To integrate the intensities of the Y-$L_{\alpha,\beta}$ line, the background windows ranged from 1700 to 1800 and from 2150 to 2460 eV, our peak window was defined from 1800 to 2100 eV. For the Yb-$L_{\alpha,\beta}$ lines, the background was calculated from 3 background windows ranging from 3000 to 4200, 5800 to 6200 and from 11500 to 13000 eV. The peak windows had the following settings: The Yb-$L_{\alpha 1,2}$ peak was integrated from 7220 to 7580 eV, the Yb-$L_{\beta 1,3,4}$ from 8240 to 8640 eV; the Yb-$L_{\beta 2}$ was excluded due to potential bias by the presence of signal corresponding to Cu-$K_{\beta 1}$. The intensity ratios were translated to concentration ratios using the Cliff-Lorimer equation (Cliff & Lorimer, 1975):

$$\frac{c_a}{c_b} = k_{ab} \cdot \frac{I_a}{I_b},$$

where I_a/I_b and c_a/c_b are intensity- and concentration ratios, respectively, and the Cliff-Lorimer factor k_{ab} is determined from the intensity ratios obtained from TEM-EDX on a thin film prior to thermal annealing as a standard, where Yb- and Y-concentrations were determined by electron microprobe analysis (EMPA). The c_{Yb}/c_Y element concentration ratios of the samples with unknown composition were obtained by applying the respective $k_{Yb,Y}$ factor to the I_{Yb}/I_Y intensity ratios measured with TEM EDX. The Yb mole fraction was finally calculated as

$$X_{Yb} = \frac{c_{Yb}}{c_{Yb} + c_Y} = \frac{k_{Y,Yb} I_{Yb}}{k_{Y,Yb} I_{Yb} + I_Y}$$

Both the thin-film used for the EMPA sample and for the TEM sample were produced in the same PLD-run using the same target material ($Yb_{1.149}Y_{1.736}Al_{5.115}O_{12}$). The EMPA measurements were carried out on a thin-film coated silicon wafer, where the contribution to the EDX spectrum from the Si substrate can be subtracted and the composition of the thin-film can be determined. Averaging at least 20 measurements yielded a thin-film composition of $Yb_{1.065}Y_{1.578}Al_{5.357}O_{12}$.

The Cliff-Lorimer factor was determined with a relative error of about 1% due

to plural measurements (nine each) with high EDS counting rates (18000 to 28000 counts for the Y peak, 15000 counts for the Yb peaks) of both the initial thin-film composition and the background noise. The stated uncertainty in the mole fraction δX_{Yb} is obtained by propagating the estimated 2σ standard deviations both in the integrated intensities I_{Yb}, I_Y and in the Cliff-Lorimer factor $k_{Y,Yb}$

$$\delta X_{Yb} = X_{Yb}\,(1 - X_{Yb}) \sqrt{\left(\frac{\delta I_{Yb}}{I_{Yb}}\right)^2 + \left(\frac{\delta I_Y}{I_Y}\right)^2 + \left(\frac{\delta k_{Y,Yb}}{k_{Y,Yb}}\right)^2}$$

This yielded total relative errors of 5% at high Yb concentration ($X_{Yb} = 0.96$) and up to 30% when the Yb concentration is low ($X_{Yb} = 0.014$, see Fig. 3.10).

The excitation volume of the specific sample needs to be considered when the profile is fitted (Fiddicke & Oelgart, 1985; Ganguly et al., 1998). In order to simulate the excitation volume we used the Monte Carlo simulation software 'Win X-Ray' version 1.3.2.3. The simulation parameters were as follows: Beam diameter was 3.8 nm, acceleration voltage was 200 keV, 150 nm thick YAG sample, density of 4.55 g/cm^3 and 200 keV acceleration voltage. The extracted excitation volume is conically shaped due to beam broadening arising from interaction with the sample material. The simulated beam size reaches a diameter between 5 and max. 8 nm at the bottom of the TEM-lamella (Fig. 3.7 in z direction). Sample tilt during measurements increases the effective beam size by ∼6% (at 20° sample tilt), which can be neglected for the purpose of our estimation of the spatial resolution. To obtain statistically relevant results from fitting a diffusion model to a composition profile, the profile has to be at least 3 times longer than the spatial resolution of the composition analysis (Ganguly et al., 1998). Our spatial resolution, considering the excitation volume and that the electron beam was scanned over a window of 20×40 nm^2, is about 28 nm in x direction and 48 nm in y direction. The profile considered had a length of about 8 times our spatial resolution. Note that these are conservative estimates, typically our samples are thinner (< 100 nm), which would lead to a final x direction resolution of 22 nm, if 99 % of the incident electrons are considered.

EDS-measurements were used to calibrate Z-contrast-intensity-profiles extracted from STEM-images of the diffusion zone (Fig. 3.8f). To obtain an integrated intensity profile of a STEM-image acquired using Tecnai imaging and analyses software (TIA - FEI), the image was imported into Digital Micrograph (GATAN) where a 460 nm long profile integrated over 350 pixels was extracted. To prevent artefacts from the edge of the sample, where gallium may have been implanted during Pt-deposition prior to the FIB-milling procedure (M. R. Lee et al., 2007; M. R. Lee et al., 2009), the profile starts 20 nm from the sample surface.

The arbitrary intensity units of the Z-contrast-intensity-profile were background corrected by subtracting the minimum intensity from the profile, setting the lowest intensities to zero. The intensity at a certain distance from the original interface was than calibrated using an EDS-measurement at the same distance from the original interface (at -118.7 nm). Both profiles overlap nicely (Fig. 3.10). The error in the EDS-measurement used for the calibration of the Z-contrast-profile can be applied to the Z-contrast-profile.

Rutherford Backscattering (RBS)

The RBS analyses were carried out at the Dynamitron Tandem Accelerator Laboratory of the Ruhr-Universität Bochum. The He^+ beam of 2 MeV was collimated by an aperture of 0.5 mm diameter about 20 cm in front of the sample allowing to analyze samples with a surface as small as 1 mm^2. A beam current between 20 and 50 nA was typically used for the measurements. An Ag-solution was painted onto the sides of the samples to ensure electrical contact to the sample holder to minimize electrical charging of the sample surface. The backscattered particles are detected at an angle of 160° using a silicon particle detector with an energy resolution of about 16–20 keV. The sample surface was tilted by 5° relative to the beam direction to avoid channeling.

The RBS spectra were simulated with the software RBX version 5.18 (Kótai, 1994) using a procedure similar to that of Tirone et al. (2005); Dohmen et al. (2007). Once a best fit is found to calculate the appropriate stopping power, a concentration-depth profile for the rare earth element is extracted. More details

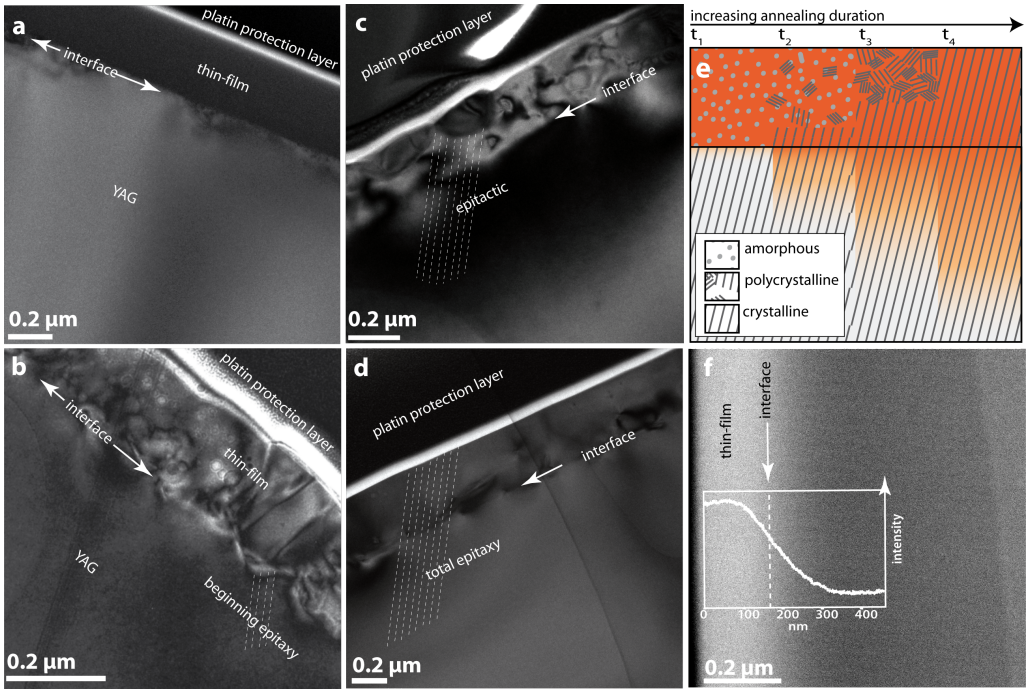

Figure 3.8: (a-d) Bright field (BF) images of the thin-film after different annealing periods at 1450°C. The platinum layer deposited on the surface of the sample prevents gallium ion damage during FIB lamella preparation. Broken lines depict the continuing crystal structure over the initial thin-film/substrate interface. (a) Prior to annealing. The thin-film is amorphous and the interface with the substrate is extremely flat. (b) After 20 minutes. The thin-film became polycrystalline, with crystal diameters ranging from tens to hundreds of nm in diameter. Epitaxy can be observed at the former interface with the substrate, further away no preferential orientation is visible. (c) After 40 minutes. The thin-film starts to copy the orientation of the substrate, but is still polycrystalline at its surface. (d) After 2 hours. The thin-film displays epitaxial growth. The varying diffraction contrast results from small distortions in the crystal lattices. (e) Schematic of the evolution of the thin-film and the diffusion profile with time. (f) STEM Z-contrast image. The brightness, which positively correlates with atomic mass, decreases from the thin-film towards the crystal volume at constant sample thickness, indicating Yb-Y diffusive exchange. At the right side of the image the brightness is compromised by the underlying holy carbon grid which serves as lamellae holder.

on the fitting procedure and the sensitivity of the method in our setup are given elsewhere (Tirone et al., 2005; Dohmen et al., 2007). During the fitting procedure, the thin-film thickness is a parameter adjusted. Therefore the thin-film thickness is obtained with an uncertainty of at least ±5 nm, which results in an uncertainty of the log$D$ value of about ±0.1 orders of magnitude.

Charging and fluorescence reduced the energy resolution to 28 (±1) keV compared to the nominal detector resolution of about 18 keV, which was confirmed using conducting samples like Si-wafers. For the calculated stopping power of YAG, this implies a depth resolution of about 0.418 nm (±10%). The RBX program considers the energy resolution and the density of the sample to deconvolute the concentration profile. However, this numerical procedure might introduce some uncertainties, which are difficult to quantify (see also Hofmann (1998) about the general problem of deconvoluting diffusion profiles).

3.2.4 Results

Thin-film crystallisation

The thin-films were initially amorphous (Fig. 3.8a), but crystallized throughout the diffusion anneal. Thin-film crystallization was monitored at annealing times ranging from several minutes to 25 hours using TEM. Already after 20 min, the films have become polycrystalline with polyhedral crystals approx. 100-200 nm in size (Fig. 3.8b). During further annealing, epitaxial-growth takes place at the interface between the initial crystal and the thin-film, but single grains of Yb:YAG with random orientations form at the surface of the thin-film (fig. 3.8c). With time (already after 40 min), the region occupied by epitaxially grown Yb:YAG expands further into the thin-film and finally (after 2 h), the entire thin-film is fully epitactic with the substrate (Fig. 3.8d). The crystallization process is summarized in figure 3.8e. Diffraction patterns indicate pure garnet phases and lattice fringe images show that lattice planes are defect free. Epitaxy is reached faster in experiments with thinner thin-films. A stronger contribution of the still amorphous starting material is observed in the diffraction pattern of the thin-film for crystals that were treated at lower annealing temperatures and shorter annealing times (less than 30 min). By

the time that full epitaxy is reached, the diffusion front is parallel to the sample surface and the initial thin-film/crystal interface (Fig. 3.8f). This is evidence for the defined geometry and insignificance of any contributions from dislocations.

It is important to note that the physical and chemical characteristics of the thin-film likely change during its crystallization. In particular, its transport properties may change significantly during the diffusion anneal; this potential effect needs to be addressed when extracting volume diffusion data from analyzed concentration profiles.

Concentration profiles

Experimental conditions and the corresponding analytical method as well as the fitting result are given in Table 3.2. Figure 3.10 shows both a diffusion profile measured with TEM and with RBS; both profiles were derived from samples that were annealed at 1450°C. The annealing time and thin-film thicknesses were chosen differently to optimize the length of the resulting diffusion profiles for either TEM (h = 185 nm, annealing time = 1445 min) or RBS (h = 45 nm, annealing time = 132 min) analysis. As we will discuss in the next section, the discrepancy in diffusion coefficients derived from two data sets is nearly 0.5 orders of magnitude.

Data Reduction

In general, one-dimensional diffusion in a crystal/thin-film assembly can be described by the diffusion equation (Crank, 1975) for the Yb mole fraction $c(x,t) = X_{Yb}$, with the diffusion coefficient $D(x,t)$ being a function of position x and time t:

$$\partial_t c(x,t) = \partial_x \left[D\left(x,t\right) \partial_x c\left(x,t\right) \right]. \tag{3.1}$$

The coordinate axis OX is orthogonal to the thin-film (fig. 3.7). In the given planar setting, the dependence of c on transversal coordinates can be ignored. In our model, the thin-film corresponds to the region -$h < x < 0$ and the crystal corresponds to the region $x > 0$ (fig. 3.7). The diffusion flux is assumed to be continuous across

the thin-film/crystal interface at $x = 0$. A no-flux boundary condition is assumed at $x = -h$ and $c(x,t)$ goes to zero at $x \rightarrow +\infty$. The initial distribution of Yb atoms is represented by the step function

$$c(x,0) = \begin{cases} c_0 \ for \ x < 0, \\ 0 \ for \ x > 0. \end{cases}$$

The successive crystallization of the thin-film influences the effective Yb diffusion coefficient in the thin-film D_{film}. As long as the thin-film is amorphous the diffusion coefficient is very large, formally $D_{film} = \infty$. During the polycrystalline stage, D_{film} depends on the microstructure in a complex fashion but it is likely that diffusion in the thin-film remains much faster than in the substrate (Kaur et al. 1995). Based on the TEM observations of the time series (fig. 3.8), we infer a rapid crystallization at $t = t_c$. Once the crystallization of the thin-film is complete, D_{film} equals the diffusion coefficient in the substrate D_{sub}. The latter is a constant for any time. In summary we assume that

$$D(x,t) = \begin{cases} \infty \ for \ x < 0, \ t < t_c, \\ D_{sub} \ for \ x < 0, \ t > t_c, \\ D_{sub} \ for \ x > 0, \ t > 0, \end{cases}$$

where both D_{sub} and t_c are unknown. The problem is illustrated in fig. 3.7. We infer the range of feasible t_c values from direct TEM observations of the crystallization process (Fig. 3.8c). D_{sub} can then be quantified from comparison of numerical solutions to experimental data. To this end, eq. (3.1) was solved numerically using the COMSOL Multiphysics software package for the implementation of the finite elements approach for several reasonable choices of t_c. In each case, the value of D_{sub} was adjusted to obtain the best fit to the experimental measurements. If the influence of crystallization on the thin-film transport properties is ignored ($t_c = 0$), an analytical solution is available for eq. (3.1). The corresponding solution is (Crank, 1975):

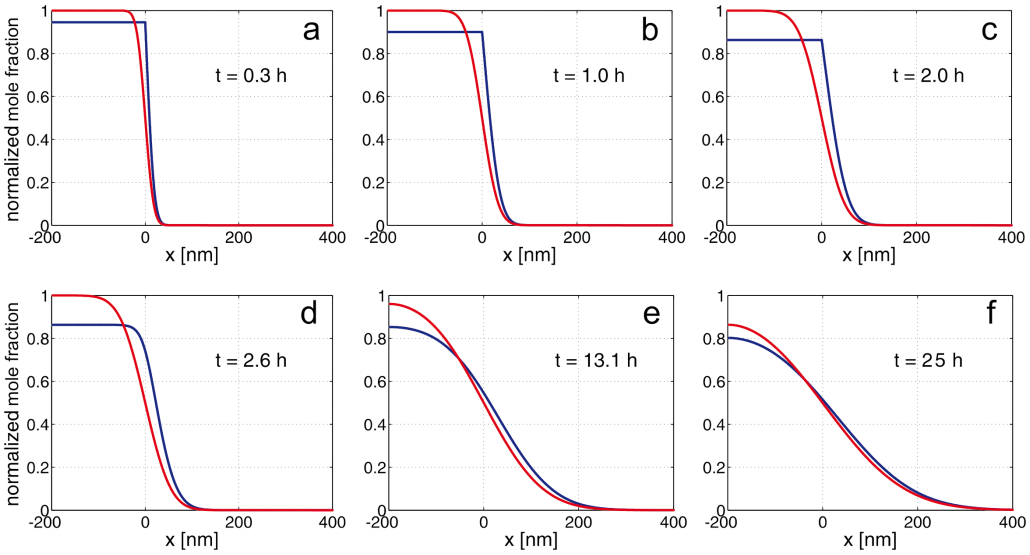

Figure 3.9: Several illustrative numerical solutions to the diffusion equation (3.1) (blue lines) are shown together with the predictions of the approximate analytical solution (3.2) (red lines). Note, that these solutions are considerably different for $t \sim t_c$, the difference decreases for $t >> t_c$. Parameter values are $h = 200$ nm, $D_{sub} = 10^{-19}$ m^2/s, $t_c = 2$ h, and $c_0 = 1$. Successive snapshots of the concentration profiles are shown.

$$c(x,t) = \frac{c_0}{2}\left[erf\left(\frac{x+2h}{2\sqrt{D_{sub}t}}\right) - erf\left(\frac{x}{2\sqrt{D_{sub}t}}\right)\right] \tag{3.2}$$

and can be used to quantify D_{sub}.

The effect of a finite thin-film crystallization time is illustrated in Fig. 3.9. Here, we have used $h = 200\ nm$, $D_{sub} = 10^{-19}\ m^2/s$, $t_c = 2\ h$, $c_0 = 1$ and compared predictions obtained from applying the simplified analytical solution (Eq. 2) with the full numerical solution for a range of annealing times. The obtained diffusion profiles are significantly different when the total annealing time is comparable to t_c. In that case, adjusting the analytical solution to the numerical curve (Fig. 3.9) would lead to an overestimation of D_{sub}. For $t >> t_c$, the differences between the analytical and numerical solutions are less pronounced and eq. (3.2) may serve as an acceptable model for data reduction. In addition, the effect of a finite crystallization time becomes more important with an increase of h. It is difficult to decide beforehand, whether for a given experimental setting, the effect of crystallization needs to be accounted for or not. To resolve the potential influence of changing thin-

film transport properties, both analytical and numerical solutions must be used to cover the feasible range of t_c, which, in turn, must be determined from independent information.

For both the TEM and the RBS data (table 3.2, experiments number 1 and 2), the extracted diffusion coefficient is rather insensitive to the crystallization time; different choices of t_c (from 20 min to 4 h) result in at most 10% differences in the extracted D_{sub}. Taking into account the uncertainties in the measured values of $c(x,t)$, the crystallization effect on the D_{sub}value cannot be traced in the current experiment and therefore the analytical solution (Eq. 2) can be used for data reduction. For the samples that were annealed at 1450°C, the model (Eq. 2) yields log$D$ values of -19.37 ± 0.07 m^2/s (TEM) and -19.84 ± 0.02 m^2/s (RBS). The different values come from individual experiments and the variation is within the statistical error estimated from experimental uncertainties on the temperature and profile measurement. Moreover, the difference is within the reproducibility of diffusion coefficient measurements using the same analytical methods (see e.g. Cherniak (1998); Dohmen et al. (2007) for RBS and Gardés et al. (2007) for TEM). The obtained fitting curves are shown in Fig. 3.10 by solid lines.

3.2.5 Discussion

The reorientation of the crystals within the thin-film can be described as a grain growth process where the substrate is the largest grain and thus dominates the process (Kaur et al., 1995; Humphreys & Hatherly, 1996). Epitaxy is reached faster with decreasing thin-film thickness as it proceeds from the original thin-film/substrate interface into the thin-film.

The potential complications that may arise from the progressive crystallization of the thin-film during the diffusion anneal and the associated change in its transport properties can be evaluated by accounting for transient diffusivities in the data reduction routine. However, for our diffusion experiments the effect of different model assumptions on the derived diffusivities is smaller than the estimated accuracy of the currently available experimental data. We have shown that the effect of successive crystallization of the thin-film is small if the time needed for complete

crystallization is small compared to the total annealing time (Fig. 3.9). In the case of experiment number 1, crystallization was completed after about 1/10 of the total annealing time and the effect of crystallization can be ignored. In the case of experiment 2 (the one analyzed by RBS), the time needed for crystallization is comparable to the total annealing time. However, the model which ignores the crystallization effect still yields a good fit to the analyzed concentration profile, probably because the diffusant source is extremely thin and thus reached epitaxy faster and the crystallization time t_c might be overestimated.

The difference between the diffusion coefficients log$D$ (m^2/s) = -19.37 ± 0.07 and -19.84 ± 0.02 extracted from experiment 1 and experiment 2, respectively, is not surprising given that the estimates are based on two independent experiments and on two different analytical techniques. A potential reason for the observed discrepancy may be due to a systematic error in the determination of profile depth, which is calculated for RBS and is determined more directly with analytical TEM. Otherwise, it could be suspected that it arises from differences in t_c, as the thin-film thicknesses were different.

In comparison to previous studies (Cherniak, 1998; Jiménez-Melendo et al., 2001), the log$D$ values obtained in our study are about 1.5 orders of magnitude lower. There are different potential explanations for this significant difference. First, the interdiffusion coefficient (for instance between Y and Yb) might depend on composition and then is a function of the individual tracer diffusion coefficients of Y and Yb (Lasaga, 1979). The diffusion profiles that are presented here do not indicate a compositional dependence, however, in the previous studies the relative initial concentration of Yb in the source was higher than in our study (pure $Yb_3Al_5O_{12}$ (Cherniak, 1998) and pure Yb_2O_3 (Jiménez-Melendo et al., 2001)). Therefore, an accelerated diffusivity for the endmember/phase can not be excluded. Second, diffusion in single crystals requires point defects such as vacancies or interstitials. A higher concentration of point defects could lead to higher diffusion coefficients. Cation vacancies can for example be produced by Si incorporation (Kuklja & Pandey, 1999; Kuklja, 2000). It can further be speculated that other parameters, such as f_{O2} and especially f_{H2O} might play a role. Also, in the study of Jiménez-Melendo et al. (2001) polycrystals

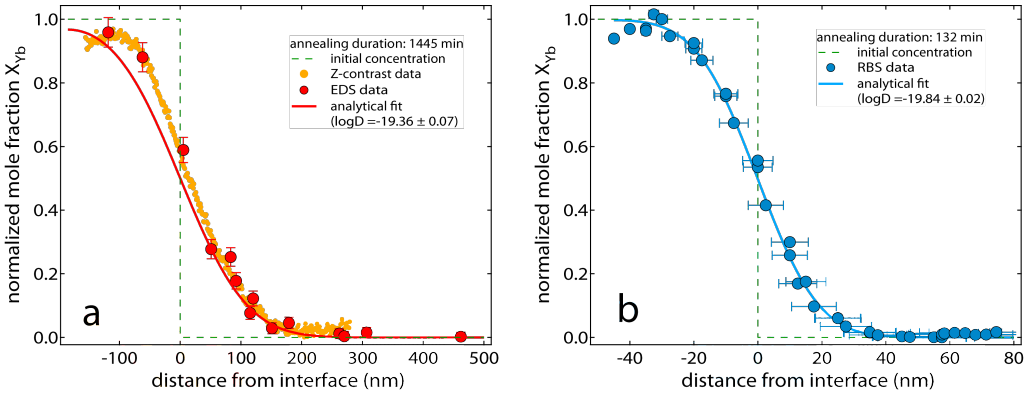

Figure 3.10: Yb diffusion profile in YAG measured by ATEM (a) and RBS (b). The annealing temperature is constant (1450°C), but the time and the thin-film thickness were chosen differently. Note that the abscissas are scaled differently. The interface between thin-film and substrate is at zero. The Yb mole fraction is normalized over c_0 (the initial value in the thin-film) since c_0 slightly varies for the two experiments (0.40 for TEM and 0.42 for RBS). The log$D$ values obtained from the two profiles differ by about 0.5 log units. The uncertainty in x of the TEM data is max ±5 nm, this corresponds to the size of the markers. The lines are least square fits to the experimental data using Eq. (3.2), where the only free parameter was the diffusion coefficient. Additionally, the EDS-scaled Z-contrast data are displayed as yellow dots in (a). Only the EDS data point at -118 nm was used for scaling, this indicates that the intensity of the Z-contrast varies linearly with the composition. The error mentioned is the least square error from fitting.

were used instead of single crystals.

3.2.6 Conclusion

Thin-film/single crystal assemblies are well suited to produce diffusion couples in simple (one-dimensional) miniaturized geometry. Analytical TEM provides a tool for micro-chemical analysis at high spatial resolution to resolve the details of short concentration profiles on the scale of a few μm. Its advantage lies in the capability to obtain structural information on nm^3-sized volumes simultaneously. In this respect it is complementary to RBS, which averages over millimetres. Furthermore, EDS can be used to calibrate Z-contrast images and extract continuous concentration profiles or to calibrate images to obtain concentration maps at constant sample thickness.

Although the observed progressive crystallization of the thin-film does not have a significant influence on the volume diffusion coefficients obtained in this study,

the potential effect of transient transport properties cannot generally be ignored. It might become important if future improvements in analyzing capabilities allow for better resolving element distributions at highest spatial resolution in two and three dimensions. Therefore, model parameters should be chosen as closely as possible to the real scenario in order to give the most reliable diffusion data.

Acknowledgements

The authors like to thank the programmers (H. Demers, P. Horny, R. Gauvin, E. Lifshin) of the Monte Carlo program Win X-Ray, which is an extension of the well known program CASINO. K. M. thanks Hauke Marquardt for extensive discussions.

Grain Boundary and Volume Diffusion Experiments in Yttrium Aluminium Garnet at 1723 K: A Miniaturized Study

by Katharina Marquardt (née Hartmann), Elena Petrishcheva, Emmanuel Gardés, Richard Wirth, Rainer Abart, and Wilhelm Heinrich

submitted to *Contributions to Mineralogy and Petrology*

3.3 Grain Boundary and Volume Diffusion Experiments in Yttrium Aluminium Garnet at 1723 K: A Miniaturized Study

Katharina Marquardt[1]*, Elena Petrishcheva[2], Emmanuel Gardés[1], Richard Wirth[1], Rainer Abart[2,3], Wilhelm Heinrich[1]

[1]*German Research Centre for Geosciences GFZ, Section 3.3, 14473 Potsdam, Germany*

[2]*Freie Universität Berlin, Institute for Geological Sciences, 12249 Berlin, Germany*

[3]*Department for Lithosphere Research, University of Vienna, Vienna, Austria*

**née Hartmann, corresponding author: hartmann@gfz-potsdam.de*

3.3.1 Abstract

Yb-Y interdiffusion along a single *near* Σ grain boundary of a synthetic yttrium aluminium garnet (YAG) bicrystal has been studied using analytical transmission electron microscopy (ATEM). To investigate the diffusion, a thin-film containing Yb as diffusant was deposited perpendicular to the bicrystal grain boundary by pulsed laser deposition (PLD). Structural properties and their change with temperature of both the diffusant source and the grain boundary are reported. The diffusion profiles are incorporated in a numerical diffusion model, which is applied to determine the grain boundary diffusion coefficient D_{gb} at 1723 K to equal 3×10^{-15} m^2/s. We find that grain boundary diffusion is 4.85 orders of magnitude faster than volume diffusion, which was determined from the same diffusion experiment. This difference can be considered as lower bound, because Σ grain boundaries as used here likely exhibit lower diffusion rates than grain boundaries of arbitrary orientation. Finally, we successfully tested the capability of synchrotron-based nano x-ray fluorescence analysis to map micro-chemical patterns in two dimensions with sub-μm resolution.

3.3.2 Introduction

Grain boundary diffusion governs numerous phenomena in solid materials, such as Coble creep, sintering properties, diffusion-induced grain boundary migration, different discontinuous reactions, recrystallization, grain growth and diffusive crack healing (Gupta, 1975; Evans & Charles, 1977; Wanamaker & Evans, 1985; Hailong

& Jun, 2002). Grain boundary diffusion is the dominating atomic transport mechanism at low temperatures while volume diffusion is sluggish. Even if the rates of grain boundary and volume diffusion approach with increasing temperature, it is commonly assumed that grain boundary diffusion is prevailing over volume diffusion during most small-scale transport processes of elements in large portions of the solid Earth. Most solutions to the grain boundary diffusion problem relate to the product of D_{gb} and the *effective* (or chemical) grain boundary width δ (e.g. Fisher, 1951). To obtain D_{gb}, δ is assumed. The *effective* grain boundary width is defined as the zone of enhanced diffusion around a grain boundary (S. White, 1973) and results from strain induced by misfit of the adjacent crystal lattices. In ionic crystals, it is accompanied by a space-charge layer (Lehovec, 1953; Kliewer & Koehler, 1965; Kingery, 1974). The *structural* (or physical) grain boundary width, in contrast, is defined as the distance between two adjacent crystal lattices and is probably smaller than the *effective* grain boundary width.

In a geomaterials' context, previous experimental attempts to exactly quantify grain boundary diffusion are hampered by a number of difficulties such as: (i) Grain boundary diffusion studies are mostly performed on polycrystals with randomly shaped grain boundaries where orientation is not well constrained. Thus, the diffusion geometry is very complex and often impossible to characterize adequately. (ii) The methods commonly used, for example secondary ion mass spectrometry (SIMS), give little or no information about the local defect structure. They also have rather poor lateral resolution. Therefore, grain boundary and volume diffusion are often measured simultaneously and the extraction of the respective diffusion coefficients is based on numerous assumptions. Moreover, it is known from studies on metals and alloys that the diffusivity can vary by orders of magnitude with varying grain boundary orientation (Herbeuval et al., 1973; Klugkist et al., 2001; Guan, 2003), which is a consequence of changing grain boundary energies. This cannot be unequivocally determined, and often an averaged diffusivity is obtained as several grain boundaries with potentially different transport properties are analysed at the same time. (iii) Analytical or numerical solutions to the grain boundary diffusion problem are often oversimplified or they are not well adapted to the experimental

set up, sometimes simply because the samples cannot be characterized well enough.

It may be surprising that diffusion along a single grain boundary has not yet been studied on the nm-scale, even though it has been proposed as early as 1986 (Clarke & Wolf, 1986) and nm-resolved analyses of low-temperature volume diffusion were already performed in 1983 (Nicholls & Jones, 1983). However, site specific sample preparation such as TEM-lamellae using the focused ion beam (FIB) technique became available only in the last decade (Phaneuf, 1999; M. R. Lee et al., 2003; Wirth, 2004). Furthermore, the fabrication of grain boundaries with exactly defined orientations by using wafer direct bonding was developed in geosciences only recently (Heinemann et al., 2001; Heinemann et al., 2005).

Here, we report an innovative alternative approach to quantify grain boundary diffusion by taking advantage of the above methods recently developed in different scientific disciplines. The main improvements of the present study over previous experimental and analytical procedures are the following:

1. Simple geometry: We use bicrystal synthesis by direct wafer bonding to produce a perfectly straight and exactly oriented grain boundary. As diffusant source, a thin-film is deposited perpendicular to the grain boundary using PLD. The resulting experimental geometry is simple and extremely well defined (Fig. 3.11).

2. High resolution analytics: We combine site specific sample preparation by FIB with measurements by TEM. The latter has two main advantages. First, it has a very high spatial resolution and second, it provides information on the local defect structure, without being destructive. The simple diffusion geometry allows for appropriate TEM analyses, because it is possible to orient the grain boundary parallel to the axis of the incident electron beam and the energy dispersive x-ray (EDX) detector, whereby artefacts from planar defect are excluded (e.g. Williams & Carter, 1996). Furthermore, volume and grain boundary diffusion are discriminated and measured on the same sample from one experiment using exactly the same experimental and analytical settings.

3. Numerical modelling: We perform numerical simulations to account for all our experimental observations. We will show that a quantitative evaluation of the diffusion coefficients in our system cannot be performed by applying conven-

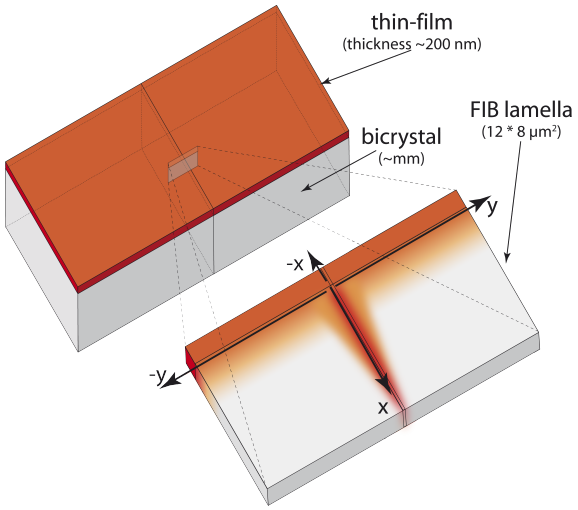

Figure 3.11: Schematic sketch of the sample geometry. The grain boundary of the bicystal is perpendicular to the thin-film (dark grey). The thickness of the thin-film is about 200 nm. The blow-up shows a sketch of the TEM lamella prepared with the FIB technique. The dimensions of the foils are usually 15×10 μm^2 with a thickness of about 100 nm, whereas the bicrystal's size is in the mm-range.

tional analytical solutions, because none would meet the present experimental configuration and our observations on the nm-scale.

We use synthetic yttrium aluminium garnet (YAG) bicrystals as model samples. YAG has several advantages over naturally occurring garnet, particularly the availability of large stoichiometric and highly pure single crystal wafers and its resistance against electron beam damage. Moreover, grain boundary diffusion of rare earth elements in YAG has previously been studied using SIMS (Jiménez-Melendo et al., 2001), which allows to compare the different approaches.

3.3.3 Materials and Methods

Bicrystal synthesis by direct bonding

Starting material for our experiments were high-purity $Y_3Al_5O_{12}$ single crystals (Yin et al., 1998; Lupei et al., 2001; Weber & Abadie, 2001; Dobrzycki et al., 2004) for the bicrystal synthesis (Hartmann et al., 2010) and Yb-doped YAG as precursor for the thin-film, i.e. the diffusant source. YAG bicrystal samples were synthesized by the wafer direct bonding method (Tong et al., 1995; Heinemann et al., 2005; Reiche,

2006; Gösele et al., 1999; Pössl & Kräuter, 1999). The highly polished and ultra clean crystal surfaces are saturated with pure adsorbed water and are brought into contact without force. When contact is established, hydrogen bonds of the opposing crystal surfaces are expected to form. The adsorbed water evaporates at elevated annealing temperatures leaving a grain boundary behind.

A detailed description of the bonding procedure, as well as the specific orientation relationship for the samples used, is given in Hartmann et al. (2010). The contact geometry is close to a tilt boundary of 36.9° about the bicrystals' common [100] direction, this equals a twist boundary of 180° parallel to the (210) plane. Thus, the bicrystals' grain boundary can be considered as a *near* Σ5 (210)/[100] grain boundary.

Diffusion experiments

Diffusion experiments are designed in thin-film geometry, where the grain boundary is covered with the thin-film perpendicular to the surface (Fig. 3.11). PLD (PLD, Dohmen et al., 2002; K. Marquardt et al., in Press) was used to deposit Yb-doped YAG thin-films on the bicrystal. A general review of the method is given by Chrisey and Hubler (2003). As source material (target) for the deposition, we used a Czochralski grown Yb:YAG homogeneous single crystal ($Yb_{1.17}Y_{1.83}Al_5O_{12}$, see H. Marquardt et al. (2009)). Prior to thin-film deposition, the polished bicrystal samples were heated to 893 K in order to desorbe potential organic contamination. The diffusion anneals of different time ranges were done in a gas mixing furnaces at 1723 K and ambient atmosphere. The annealing durations were 5 min, 20 min, 40 min, 2 h, 24.1 h, 48 h and 68 h. Temperature and oxygen fugacity were monitored in situ by a type-B thermocouple and a f_{O2}-sensor. For the determination of the grain boundary diffusion, the 24.1 h anneal was used, because the length of both the volume diffusion profile and the grain boundary diffusion profile were long enough for the analyses, but did not extend over the FIB-foil dimensions.

Transmission Electron Microscopy (TEM)

TEM lamellae ($15\times8\times0.1$ μm^3) were prepared using the FIB technique (Overwijk et al., 1993; Phaneuf, 1999; M. R. Lee et al., 2003; Wirth, 2004). Using this method, samples of constant thickness can be prepared, which is a prerequisite to calculate element ratios directly from Energy Dispersive X-ray Spectroscopy (EDS) data.

We used analytical and energy-filtered high resolution TEM (ATEM, HRTEM) on a Tecnai F20 X-Twin TEM operated at 200 kV with a field emission gun (FEG) as electron source. The TEM is equipped with a post-column Gatan imaging filter (GIF Tridiem). All of the TEM images presented are energy-filtered images, where a 10 eV window was applied to the zero loss peak. The Gatan Digital Micrograph software was used to analyse the transmission electron micrographs.

ATEM was performed with an EDAX X-ray analyzer equipped with an ultra thin window. The intensities were measured during a counting time of 100 s in scanning transmission mode (STEM). The incident electron beam was focused to a diameter of 3.8 nm. We measured in pre-selected windows of 20×40 nm^2. The sample was inclined towards the detector by an angle of 15-20°. The thin-film/substrate interface of the sample was oriented approximately parallel (within 2-5°) to the detector axis and the incident beam. We avoided crystal orientations where strong diffraction occurs, such as two-beam (Bragg) or in-zone-axis orientations, to circumvent potential bias of EDS analysis due to electron channelling. The background was subtracted from each TEM-EDS spectrum using a second-order polynomial, where the parameters were adjusted to obtain the best least-square fit to the background before and after each relevant peak. Furthermore, we measured zero-Yb spectra to obtain an average value for the background noise in our EDS measurements. The noise was then subtracted from each spectrum. Integrated x-ray intensities of Yb ($L_{\alpha,\beta}$) and Y ($L_{\alpha,\beta}$) were used to calculate the intensity ratio I_{Yb}/I_Y. The intensity ratios were converted to concentration ratios using the Cliff-Lorimer equation (Cliff & Lorimer, 1975) to finally calculate the mole fraction of Yb. A more detailed description of the data processing is given in K. Marquardt et al. (in Press). They also provide more details on the error propagation using the Cliff-Lorimer equation and on the estimated excitation volume as well as the resolution due to window measurements.

Nano X-ray fluorescence (XRF) analysis at the ESRF

Qualitative elemental maps of the diffusion zone in the bicrystal have been obtained at the European Synchrotron Radiation Facility (ESRF) in Grenoble, France. Experiments were performed at the nanoprobe beamline ID13, where a hard x-ray nanobeam generated with nanofocusing x-ray lenses (NFLs, Boye (2009)) are used to run fluorescence analyses with a spatial resolution ranging from 200 to 50 nm (Kuwano et al., 1992; Schroer et al., 2005; Hanke et al., 2008). A FIB-cut lamella ($10\times8\times0.25$ μm^3) was mounted on a perforated carbon-film on a 3 mm copper grid, which is a standard procedure to mount TEM-FIB-lamellae. The energy of the x-rays was 24.3 keV. The spatial resolution is basically defined by the spot size, which was determined by gold knife-edge scans to be 165×171 nm^2 in our experiment. The sample is oriented 45° with respect to both the energy-dispersive detector and the incident beam to record maximum fluorescence signals.

3.3.4 Experimental Results

Thin-film crystallisation

The grain boundary produced by direct wafer bonding is thoroughly described in Hartmann et al. (2010) and is used for our grain boundary diffusion experiment. The thin-film, which serves as diffusant source, is oriented perpendicular to the grain boundary (Fig. 3.11). It was initially amorphous (Fig. 3.12a), but crystallized during the diffusion anneal (Fig. 3.12b) and adapted the structure and orientation of the bicrystal. As a result, the grain boundary extends into the homoepitaxially grown thin-film (Fig. 3.12c).

The observed progress of the thin-film crystallization was as follows: After 20 min, the films are polycrystalline with polyhedral crystals ranging from about 100 to 200 nm in size, their diameter exceeds the thin-film thickness (Fig. 3.12b). Some amorphous material still remained between the crystals, at the thin-film/bicrystal interface local epitaxial growth is present. After 40 min, epitaxy and crystallisation are highly advanced (Fig. 3.13). Thin-film and bicrystal substrate are completely homoepitactic after 2 h (Fig. 3.12c). Diffraction patterns designate only the pres-

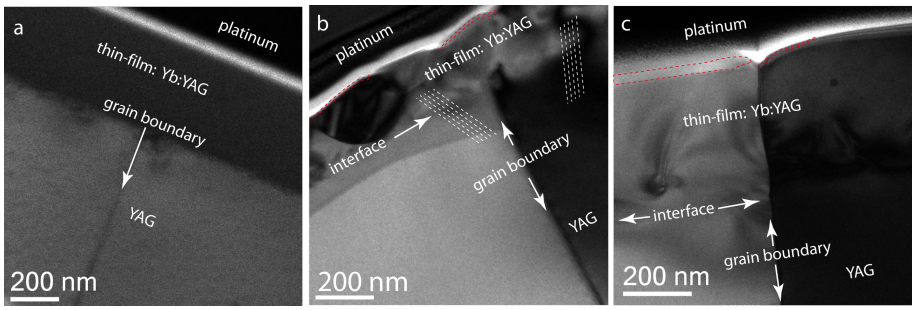

Figure 3.12: Bright field (BF) images of the bicrystal with the thin-film prior to and after annealing. For FIB sample preparation, a protection layer of platinum was deposited on the carbon coating (upper part of the images). (a) The thin-film is initially amorphous and has an excellent contact with the bicrystal. (b) The thin-film after 20 min annealing at 1723 K is partially recrystallized. Some parts of the thin-film are epitactic with the bicrystal, indicated by broken lines. Still, some large crystals are present. The right bicrystal grain is in a strongly diffracting orientation and the lower region of the thin-film has the same orientation. The outermost ~2% of the thin-film are amorphous, illustrated by red dashed lines. The slightly curved contrast change below the thin-film/bicrystal interface on the left part is caused by a hole in the sample-supporting perforated carbon film. (c) Thin-film after 2 h annealing at 1723 K. The diffraction contrast causes a different shading of the opposing crystals. The thin-film grew epitaxially on the bicrystal, thus the grain boundary continues into the thin-film. The thin-film of this specific sample is 380 nm thick; at the surface of the left grain, some portions (up to 13%) are not crystalline (indicated by red dashed lines). Note that the grain boundary produced in the former thin film is slightly curved. Close to the surface, it is inclined with respect to the incident beam. A groove formed during annealing at the surface of the thin-film.

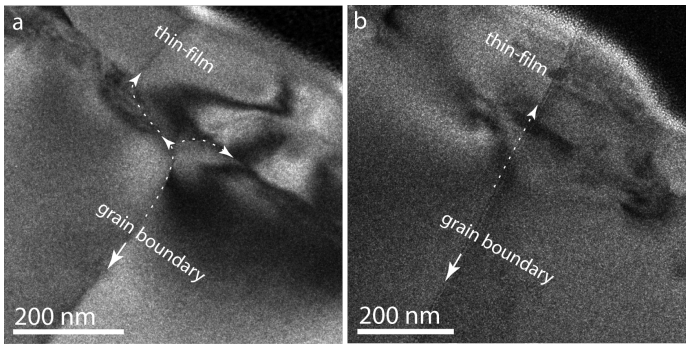

Figure 3.13: BF images of the grain boundary in the thin-film after annealing at 1723 K for a period of 40 min. Images (a) and (b) are acquired using different defocus settings on the same sample, thus different planes of depth were imaged. The sample was about 180 nm thick. (a) The grain boundary of the bicrystal substrate starts to curve towards the thin-film and joins a grain boundary between two grains of the polycrystalline thin-film. (b) At a different image plane of the same sample, the grain boundary of the bicrystal continues straight into the thin-film. The thin-film is close to full epitaxy. The pitted appearance of the images arises from the relatively thick sample.

ence of garnet phases and the grain boundaries are now fully crystalline. In contrast, amorphous material at the surface of the thin-film was still present, even after annealing for 24 h. The thickness of the remaining amorphous layer differs with space, mostly it is in the range of 2% of the entire thin-film thickness, but at one position, it reached 13% of the thin-film thickness (Figs. 3.12 and 3.13).

Grain boundary characteristics in the bicrystal and thin-film

We characterised the grain boundary of the original bicrystal after each anneal. Structural changes, such as orientation relationships between the adjacent grains, rigid body displacements, grain boundary migration, dislocation or step formation were only rarely observed. For example, in one experiment we observed that the orientation and placement of the grain boundary of the bicrystal changed as it became curved towards the interface thin-film/bicrystal (Fig. 3.14). Samples where such phenomena occurred were excluded from further investigation. Lattice fringe images reveal no defects in the lattice planes imaged. Based on high resolution transmission electron micrographs published elsewhere (Fig. 3.5 in Hartmann et al. (2010), we estimate the *structural* grain boundary width to alternate between 0.5

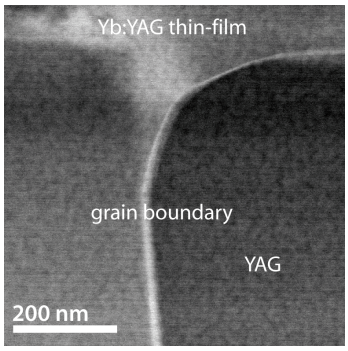

Figure 3.14: STEM image of an experiment where grain boundary migration was observed and which was therefore discarded from further investigation. Grain boundary migration is rather the exception than the rule in these experiments. The image is partially influenced by diffraction contrast, visible due to the chosen camera length.

and 3 nm. It is surrounded by a substantially strained lattice in both of the adjacent grains.

Furthermore, we investigated the grain boundary, which has formed within the thin-film. During the initial stages of annealing (5-40 min), the grain boundary within the thin-film meandered between the crystals of the polycrystalline thin-film and was often inclined with respect to the bicrystal grain boundary (Fig. 3.13a, b). Figure 3.13b, taken after a 40 min anneal, shows that at some parts the grain boundary cuts already straight through the thin-film.

After longer annealings, the grain boundary of the thin-film has the same orientation as in the bicrystal (Figs. 3.12c, 3.15). In some experiments, however, minor changes in orientation occur. Such minor changes are, for example, absence of steps that are normally present at the grain boundary in intervals of 40 nm (Hartmann et al., 2010) or slight curvatures in the newly generated grain boundary. The grain boundary in the thin-film of the sample annealed for 24.1 h displays the same orientation as the grain boundary in the bicrystal (Fig. 3.15). Lattice fringe images reveal no defects in the lattice planes imaged.

Diffusion profiles

Interdiffusion profiles of Yb-Y in the volume and in the grain boundary are plotted as mole fractions of Yb versus distance from the thin-film/bicrystal interface (Fig.

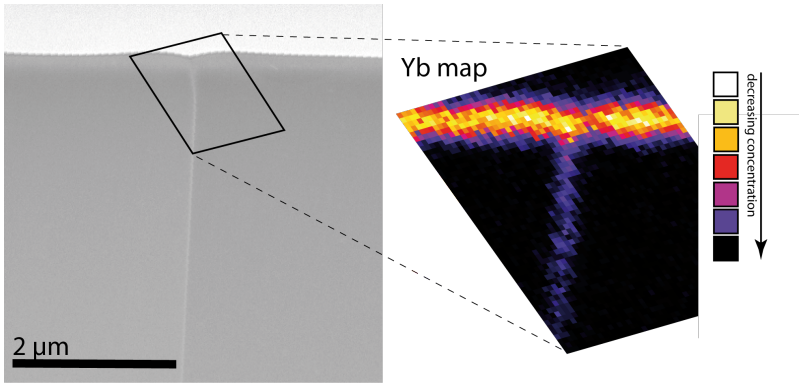

Figure 3.15: STEM image of the sample investigated with nano-XRF (1723 K and 24.1 h). The camera length is chosen to probe a mixture of Z-contrast and diffraction contrast; the thin-film is fully epitactic. The platinum layer corresponds to the brightest grey in the image, the thin-film appears in light grey, and the two parts of the bicrystal are dark grey. The region mapped using the Yb-L_α peak from synchrotron x-ray fluorescence at the ESRF is shown in the enlargement.

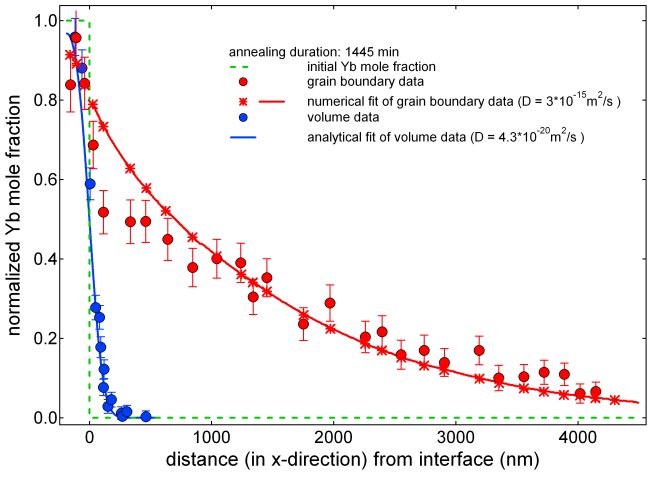

Figure 3.16: Comparison of volume diffusion (blue points, data from K. Marquardt et al. (in Press)) and grain boundary diffusion (red points). Both profiles were measured by EDX-based ATEM on the same lamella cut by FIB. The interface between thin-film and substrate is at zero. The calculated grain boundary diffusion coefficient is 4.85 orders of magnitude higher than the one for volume diffusion. The red stars are the mean values of the calculated mole fraction (averaged over 20×40 nm^2 boxes along the grain boundary of the numerical model).

3.16). An overview map of the Yb distribution along and across the grain boundary is shown in Fig. 3.15.

3.3.5 Numerical Modelling of Grain Boundary Diffusion

Fast diffusion along an isolated grain boundary, accompanied by relatively slow diffusion into the volume of the adjacent crystals, has been considered theoretically in a number of studies starting with the pioneering work of Fisher (1951). The thin-film, which serves as the diffusant source, was, however, only treated very approximately; either it was considered as a constant source (e.g. Fisher, 1951; Whipple, 1954) or as an instantaneous source (Suzuoka, 1961; Suzuoka, 1964). In the present case, the thin-film undergoes a structural change during the diffusion anneal that must be taken into account (see K. Marquardt et al. (in Press)). Therefore the diffusion profiles were modelled with the following working assumptions:

1. The final diffusant distribution inside the thin-film is time-dependent and non-uniform; the Yb mole fraction decreases towards the thin-film/substrate interface. Therefore, a detailed analysis of diffusion inside the thin-film is necessary.
2. The diffusion coefficient in the thin film decreases by several orders of magnitude during annealing, since it is initially amorphous and subsequently crystallized.
3. After crystallization, diffusion is similarly slow in both the thin-film and the bicrystal.
4. As the narrow outer thin-film layer remains amorphous, diffusion therein and at the surface of the thin-film is still fast.
5. After crystallization, the grain boundary cuts through the thin-film; thus it is connected to the outermost layer of the thin-film, where diffusion is fast at any time.

A numerical model that accounts for these characteristics of the diffusion assembly was developed using the COMSOL Multiphysics software package for the implementation of the finite elements approach. The system geometry is shown in Figure 3.17. The OX-axis lies along the grain boundary, the thin-film region corresponds to negative values of x. The OY-axis traces the initial interface between the

thin-film and the bicrystal. In our modelling, we use a two-dimensional setting; the dependence of the diffusant distribution on z is ignored.

The transport of Yb in the YAG bicrystal (blue region in Fig. 3.17) is governed by a linear diffusion equation

$$\frac{\partial c}{\partial t} = D_v \left(\frac{\partial^2 c}{\partial x^2} + \frac{\partial^2 c}{\partial y^2} \right) \tag{3.3}$$

for the Yb mole fraction

$$c\left(x, y, t\right) = \frac{c_{Yb}}{c_{Yb} + c_Y},$$

where c_{Yb} and c_Y are the Y and Yb concentrations, respectively. The parameter D_v denotes the volume interdiffusion coefficient between Yb and Y in the bicrystal. Material transport along the grain boundary is described by a reduced diffusion equation (Fisher, 1951)

$$\frac{\partial u}{\partial t} = D_{gb} \frac{\partial^2 u}{\partial x^2} + \frac{2 D_v}{\delta} \left(\frac{\partial c}{\partial y} \right)_{y=0} \tag{3.4}$$

for the Yb mole fraction $u(x,\ t)$ along the boundary

$$u\left(x, t\right) = c\left(x, y, t\right)|_{y=0} \tag{3.5}$$

The parameter D_{gb} in eq. (3.4) is the grain boundary diffusion coefficient, δ is the *effective* grain boundary width. The last term in eq. (3.4) describes particle loss due to transversal diffusion into the volume of the bicrystal. Equation (3.5) ensures continuity of the mole fraction.

Diffusive transport inside the thin-film is governed by a time-inhomogeneous diffusion equation

$$\frac{\partial c}{\partial t} = D_f\left(t\right) \left(\frac{\partial^2 c}{\partial x^2} + \frac{\partial^2 c}{\partial y^2} \right), \tag{3.6}$$

where the volume diffusion coefficient in the thin-film $D_f(t)$ decreases from some (large) initial value D_∞ to D_v in the course of the structural change of the thin-film from amorphous to crystalline. For simplicity, we assume that $D_f = D_\infty$ for $0 < t < t_{cr}$ (crystallization time) and $D_f = D_v$ afterwards. Initially, Yb is only present in the thin-film, such that

$$c\,(x,y,t)\,|_{t=0} = \begin{cases} c_0 & for \quad -h < x < 0, \\ 0 & for \quad 0 < x < L, \end{cases}$$

where h and L denote the extension of the thin-film and of the bicrystal along the x-axis, respectively. Both mole fraction and diffusive flux are continuous at the thin-film/bicrystal interface, such that

$$c\,|_{x=0-0} = c\,|_{x=0+0} \text{ and } D_f\,(t)\left(\tfrac{\partial c}{\partial x}\right)_{x=0-0} = D_v\left(\tfrac{\partial c}{\partial x}\right)_{x=0+0}.$$

The numerical solution was calculated in two steps. First, eqs. (3.3)-(3.6) were solved for $0 < t < t_{cr}$ for the system shown in figure 3.17a. A no-flux boundary condition was applied at the outer border of the thin-film. During the first stage, the large parameter D_∞ creates a practically uniform mole fraction distribution in the thin-film, which slowly decreases due to loss of Yb into the bicrystal.

Instantaneous crystallization is assumed to occur at $t = t_{cr}$, the corresponding value of the mole fraction for the thin-film is denoted by c_{cr}. For $t > t_{cr}$, the grain boundary extends into the thin-film as shown in Fig. 3.17b, and we replace $D_f = D_\infty$ with $D_f = D_v$ in eq. (3.6). Fast diffusion still occurs at the outer border of the thin-film, an assumption based on the observations described in section *thin-film crystallization*. In contrast, inside the thin-film, the mole fraction distribution is now almost 'frozen', changing only slowly, because $D_v << D_\infty$. Therefore, we assume that for $t > t_{cr}$, the outer border distribution of c is uniform and time-independent, and we applied a Dirichlet boundary condition $c = c_{cr}$ for $x = -h$ accordingly. In a second stage, eqs. (3.3)-(3.6) were solved for $t_{cr} < t < T$, where T is the total annealing time.

The parameter values were chosen to represent the experimental settings. Specifically, $T = 24.1$ h, $t_c = 40$ min, $h = 185$ nm, $\delta = 2$ nm (which is a mean value of the observed variations in the *structural* grain boundary width), $c_0 = 0.403$. The Yb-Y interdiffusion coefficient in the YAG crystal is $D_v = 4.3{\times}10^{-}20$ m^2/s as determined by K. Marquardt et al. (in Press), $D_\infty = 10^5 \times D_v$. For the numerical solution, the bicrystal domain was restricted to $|y| < 2000$ nm and $L = 8000$ nm. Performing calculations for $0 < t < t_{cr}$, we have found that $c_{cr}/c_0 = 0.92$. This value was applied to the Dirichlet boundary condition at the outer border of thin-film for $t_{cr} < t < T$.

Diffusion profiles were simulated for different values of D_{gb}. For each simulation, the resulting mole fraction was evaluated along the grain boundary by averaging c over $20{\times}40$ nm^2 boxes, in order to be comparable with the ATEM measurement procedure (see section *material and methods*). The best fit between the experimental and numerical results (Fig. 3.16) yields the grain boundary diffusion coefficient

$$D_{gb} = 3 \cdot 10^{-15} m^2/s. \tag{3.7}$$

The space distribution of the mole fraction c (normalized over c_0) is shown in Fig. 3.18 for $t = 0$, $t = t_{cr}$, and $t = T$. As expected, the Yb distribution in the thin-film is uniform at $t = t_{cr}$, but differs from that at $t = 0$. For $t = T$, we see a scenario of fast diffusion along the grain boundary accompanied by comparatively slow volume diffusion into the bicrystal from both the grain boundary and the thin-film. Note that within the thin-film, the Yb mole fraction is now decreasing towards the thin-film/bicrystal interface, which is in agreement with the experimental observations.

Figure 3.16 shows the calculated compositions (integrated over $20{\times}40$ nm^2 windows) along the grain boundary versus experimental data. The close agreement suggests, that the model (3.3)-(3.6) and the grain boundary diffusion coefficient (3.7) correctly describe the experimental observations.

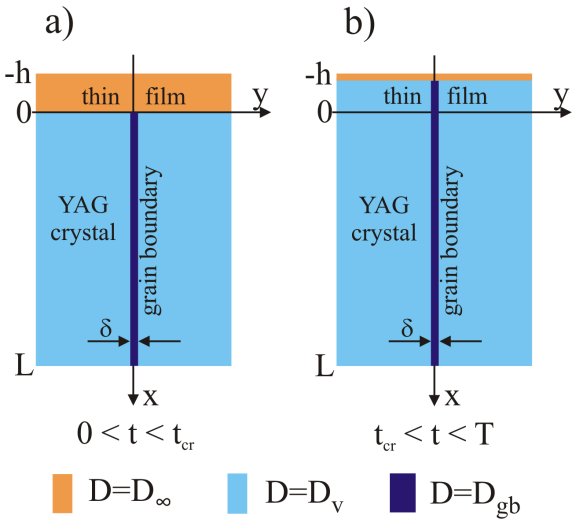

Figure 3.17: System geometry for the numerical model. (a) Initial stage of the system geometry used for modelling. (b) System geometry after $t = t_{cr}$.

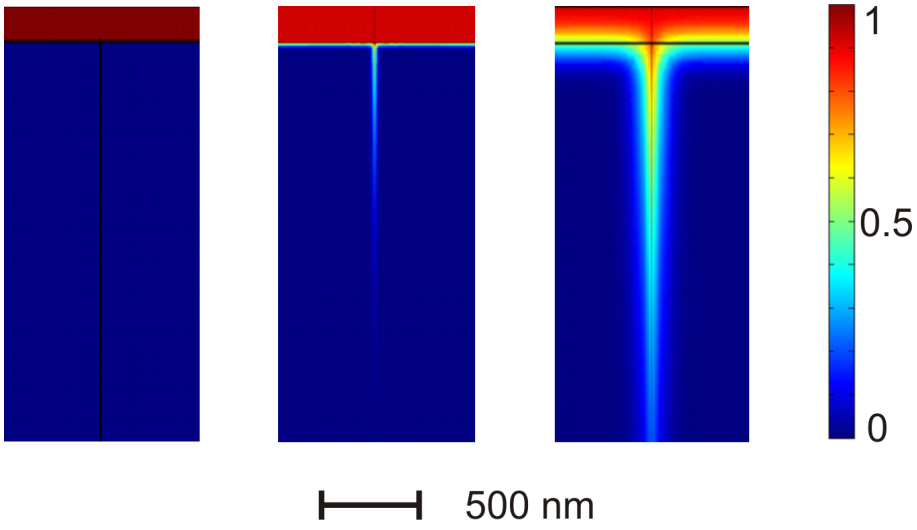

Figure 3.18: Density plots for the mole fraction of Yb $c(x, y, t)$ normalized over the initial value in the thin-film c_0 at different times. Left: the initial distribution, $t = 0$; middle: the distribution at the time of crystallization, $t = t_{cr}$, right: the final distribution at $t = T$, corresponding to the ATEM measurements.

3.3.6 Discussion

Our study was performed on YAG at 1723 K and ambient atmosphere; the experimental conditions of other studies used for comparisons are similar. For the sake of readability we will not repeat the conditions continuously.

Thin-film and grain boundary properties

The observed change of the crystals' orientations within the thin-film is related to a grain growth process, which is dominated by the largest grains, i.e. the bicrystal substrate (Kaur et al., 1995; Humphreys & Hatherly, 1996). It has repeatedly been observed that grain growth in thin-films stagnates when a grain diameter of a size approximately equal to the thin-film thickness is reached (e.g. in gold thin-films, Harris et al. (1998), or olivine and orthopyroxene, Milke et al. (2007)). This is not observed in the present study, probably because epitaxial growth dominates the final thin-film structure.

The nature of the amorphous surface layer is not irrevocably clarified. We suspect that it formed during crystallisation of the thin-film and that it is a nonstoichiometric residue that accumulated at the thin-film surface, because the thin-film crystallisation started at the interface with the substrate. In our case, minor nonstoichiometry can not be detected using TEM-EDS as the composition in the outermost layer of the sample is influenced by gallium implantation during sample preparation (M. R. Lee et al., 2003; M. R. Lee et al., 2007). Alteration of the thin-film‘s surface caused by sample preparation can not be excluded (M. R. Lee et al., 2007), but is improbable because the thickness of the amorphous layer varies randomly on single FIB-foil.

The change in grain boundary orientation and placement as shown in figure 3.13 suggests that grain rotation, grain boundary migration, and/or chemical induced grain boundary migration takes place at the chosen annealing temperatures. It probably influences the kinetics of crystallisation of the thin-film, even though its influence on the original bicrystal grain boundary is only secondary. We believe that grain rotation and grain boundary migration inside the recrystallizing film do not significantly affect the diffusion process inside the grain boundary of the bicrystal,

at least not so as long as the grain boundary diffusion lengths in the bicrystal are significantly higher than that in the thin film, i.e. at sufficiently long run durations. We therefore excluded both mechanisms for the evaluation of the diffusion processes.

Diffusion

The Yb distribution map (Fig. 3.15) obtained with nano-XRF has a relatively poor resolution compared to TEM and can not be interpreted quantitatively. Nevertheless, it is consistent with the numerical simulations (compare Figs. 3.15 and 3.18). The resolution of about 150 nm is revolutionary for synchrotron XRF measurements and is very promising for diffusion studies with profile lengths in the range of a few μm where it could provide an outstanding spatial data coverage.

Our measured diffusion profile yields a grain boundary diffusion coefficient of 3×10^{-15} m^2/s at 1723 K, which significantly differs from the value of about 1.6×10^{-13} m^2/s as reported by Jiménez-Melendo et al. (2001) using SIMS. A similar discrepancy is found for the determined volume diffusion coefficients as determined by Marquardt et al (in Press) and Jiménez-Melendo et al. (2001) and we discuss possible reasons, including different experimental setups and analyses, elsewhere (K. Marquardt et al., in Press). For the detailed comparison, it is disadvantageous that the characteristics of the thin-film diffusant source are not known in the study of Jiménez-Melendo et al. (2001). This lead to the use of a diffusion model, which is not precisely adapted to the experimental conditions. In addition, diffusion profiles measured by SIMS on polycrystals yield average profiles that contain information on volume diffusion and on grain boundary diffusion in many differently oriented grain boundaries. Both studies extracted the grain boundary diffusion coefficient from the product of D_{gb} and δ. For δ, both use a directly measured *structural* grain boundary width, because there is no information about the *effective* grain boundary width. Jiménez-Melendo et al. (2001) used a value of 1 nm, whereas we used a value of 2 nm as determined on the specific grain boundary investigated. However, *structural* and *effective* grain boundary width are not necessarily the same (Farver & Yund, 1991).

We have shown that our well defined experimental geometry has several advan-

tages for the study of grain boundary diffusion. First, it allows for measurements of grain boundary diffusion on a single grain boundary and the investigation of its orientation at the same time. Second, a thorough monitoring of the thin-film's evolution and associated changes of the local defect structure is feasible using TEM. These investigative improvements are the basis for the development of our 2D numerical model, which is well adapted to the experimental observations.

In our study, we find the grain boundary diffusion coefficient to be 4.85 orders of magnitude higher than the determined volume diffusion coefficient. Jiménez-Melendo et al. (2001) report a respective difference of about 5.38 orders of magnitude. Assuming that the two studies are internally consistent, this indicates that the *near* $\Sigma 5$ grain boundary studied in this work would exhibit a lower grain boundary diffusion coefficient than average grain boundaries. This finding is consistent with the common assumption that small angle and Σ grain boundaries have the lowest grain boundary diffusivities (Smoluchowski, 1952; Turnbull & Hoffman, 1954; Joesten, 1991; Kaur et al., 1995; Mishin & Herzig, 1999; Schwarz et al., 2002). Therefore, our finding likely represents a lower bound estimate for the difference between volume and grain boundary diffusion in the studied system.

3.3.7 Conclusion and Outlook

We performed diffusion experiments on a single well characterized grain boundary. In addition, we carefully characterized the time-dependent properties of the diffusant source in our experiments. Based on the observed structural changes of the thin-film and the associated changes of its transport properties, we developed a numerical model to extract the grain boundary diffusion coefficient from the measured diffusion profile. We find that grain boundary diffusion in our system is 4.85 orders of magnitude faster than volume diffusion and conclude that this value is at the lower end of differences between grain boundary and volume diffusion.

We showed that our innovative combination of miniaturized diffusion experiments, high resolution analytical techniques, and numerical simulations is exceptionally well suited to study volume and grain boundary diffusion simultaneoulsy

Furthermore we note, that synchrotron-based nano-XRF to map diffusion in two

dimensions, which we explored in this study, has high potential for systematic diffusion studies, where grain boundary diffusion extends over few-μm-lengths. Finally, we conclude that direct measurements of the *effective* grain boundary width are necessary for a better understanding of its influence on D_{gb}.

Acknowledgements

We would like to express our appreciation to the group of Christian Schroer from the Universität Dresden for measuring the Yb-distribution in our sample using nano-XRF at the European Synchrotron Radiation Facility and we would like to thank Manfred Burghammer and Sebastian Schoeder for assistance in using beamline ID13. Furthermore, the financial support by the section of Georg Dresen is highly acknowledged, as it allowed travelling to Bochum for thin-film deposition. We thank Ralf Dohmen for his support during PLD thin-film production. K. M. thanks Hauke Marquardt for the manifold discussions on the topic and analyses.

Insights into the Effective Grain Boundary Width

by Katharina Marquardt (née Hartmann), Quentin M. Ramasse, Christian Kisielowski, and Richard Wirth

submitted to *American Mineralogist*

3.4 Insights into the Effective Grain Boundary Width for Diffusion

Katharina Marquardt[1,2], Quentin M. Ramasse[2,3], Christian Kisielowski[2], Richard Wirth[1]

[1]*German Research Centre for Geosciences GFZ, Section 3.3, 14473 Potsdam, Germany*

[2]*National Center for Electron Microscopy (NCEM), Berkeley, USA*

[3]*now at: SuperSTEM Laboratory, STFC Daresbury, Keckwick Lane, Daresbury, UK*

3.4.1 Abstract

Atomic diffusion along grain boundaries in solids is a key process in many geological environments and in ceramics research. It is closely related to the *effective* grain boundary width, which is an important parameter in numerous equations describing diffusional or rheological processes, including plastic deformation of polycrystals, intergranular failure, and recrystallization. Here, we studied the effect of diffusion on a single well-characterized *near* Σ5 grain boundary in yttrium aluminum garnet (YAG) using different transmission electron microscopy (TEM) methods at atomic resolution. Focal series in combination with multislice calculations yielded the electron exit wave. This, combined with chemically-sensitive Z-contrast images, shows a ∼20 nm wide zone of enhanced Yb diffusion parallel to the grain boundary, which we assume to be the *effective* grain boundary width for diffusional processes. This width strongly differs from the *structural* grain boundary width of maximal 1 nm in the present study. The combination of miniaturized samples and TEM at atomic resolution are excellent tools to study varying processes at the atomic scale.

3.4.2 Introduction

A large part of the Earth's interior is comprised of solid materials. Individual mineral grains are separated by phase or grain boundaries. Their structure and interface chemistry impact the bulk properties of rocks and thus play a pivotal role in numerous geological disciplines. Diffusional or rheological processes are described using equations, which include the *effective* (or chemical) grain-boundary width δ (Farver & Yund, 1991) as an imperative parameter (Kaur et al., 1995). The *effective*

grain boundary width is defined as the zone of enhanced diffusion around a grain boundary (S. White, 1973) and results from strain, induced by misfit of the adjacent crystal lattices. In ionic crystals, it is accompanied by a space-charge layer (Lehovec, 1953; Kliewer & Koehler, 1965; Kingery, 1974). The *structural* (or physical) grain boundary width, in contrast, is defined as the distance between two adjacent crystal lattices.

Despite its importance, the *effective* grain boundary width has never been measured directly. Instead, it is usually determined in combination with the grain boundary diffusion coefficient (either as product or as quotient). This complicates not only the determination of δ, but also adds considerable uncertainty to the derived diffusion coefficient (Turnbull, 1951; Coble, 1961). Estimates for δ range from 0.04 nm in pure metals such as Ag and Ni, to 10-30 nm in oxides such as Al_2O_3 and BeO, to 1-2 μm in alkali halides and MgO (Mistler & Coble, 1974).

The importance of quantifying the *effective* grain boundary width is further documented in numerous studies encompassing various topics, including grain growth (Joesten & Fisher, 1988; Fan et al., 1997; Moelans et al., 2008), deformation in shear zones, grain boundary sliding (Padmanabhan & Basariya, 2009), grain boundary electrical conductivity (Avila-Paredes et al., 2009), melting (Dillon & Harmer, 2007; Mellenthin et al., 2008; Fensin et al., 2010), segregational processes during sintering (Kuwano et al., 1992; Kaneko et al., 2000; Sato et al., 2007; Sato et al., 2009), intergranular failure (Valiev et al., 2007) and diffusion (Mistler & Coble, 1974; Farver & Yund, 1991). For all its importance, the*effective* grain boundary width is far from being understood.

Element diffusion along grain boundaries is usually orders of magnitude faster compared to volume diffusion (Elliott, 1973; Lasaga, 1979; J. C. White & White, 1981). In general, solid state diffusion is a relatively slow process and consequently miniaturizing samples are favourable, as they allow to obtain concentration profiles on time-scales reasonable for laboratory experiments. Nevertheless, most diffusion studies are macroscopic in the sense that diffusant concentrations and component fluxes are determined on bulk materials without resolving processes on the scale of individual grains/grain boundaries not to mention atoms.

The present contribution has two major intentions. The first aim is to quantify the *effective* grain boundary width δ from direct measurements. The second goal is to demonstrate how essential information on geological processes can be readily obtained from miniaturized samples analysed with TEM at atomic resolution.

To pursuit these goals, we perform a study on a synthetic YAG bicrystal (Hartmann et al., 2010), which was previously used for a grain boundary diffusion study in thin-film geometry (K. Marquardt et al., submitted). The experimental configurations are illustrated in Figure 3.19a. Electron energy loss spectroscopy (EELS) elemental maps were combined with high resolution TEM (HRTEM) phase reconstruction using negative C_s imaging and image simulation. This was complemented with scanning TEM (STEM) for atomic resolved Z-contrast imaging.

3.4.3 Material

The synthesis of the bicrystal and a detailed investigation of the grain boundary structure is given elsewhere (Hartmann et al., 2010; K. Marquardt et al., submitted). The produced *near* $\Sigma 5$ grain boundary orientation is relevant for the understanding of processes that occur along random grain boundaries as they frequently occur in polycrystalline materials (Vonlanthen & Grobety, 2008).

3.4.4 Experimental Methods

EELS

The elemental map of Yb (Fig. 3.19b) was acquired using a Tecnai F20 X-Twin TEM operated at 200 kV with a field emission gun (FEG) Schottky electron source. The TEM is equipped with a post-column Gatan imaging filter (GIF Tridiem). EELS data acquisition focused on the high loss edges of Yb (M_5 1528 eV; M_4 1576 eV edges), because the Yb $N_{4,5}$ edge at 185 eV overlaps unfavourably with the $M_{4,5}$ edge of Y, producing very small peak to background ratios. Collection times of 20 s were needed to obtain sufficient counts; therefore only jump ratio elemental maps of Yb were acquired.

Note that elemental mapping requires extremely thin samples (in the range of 20-60 nm), a demand that cannot generally be satisfied over several hundreds of nm,

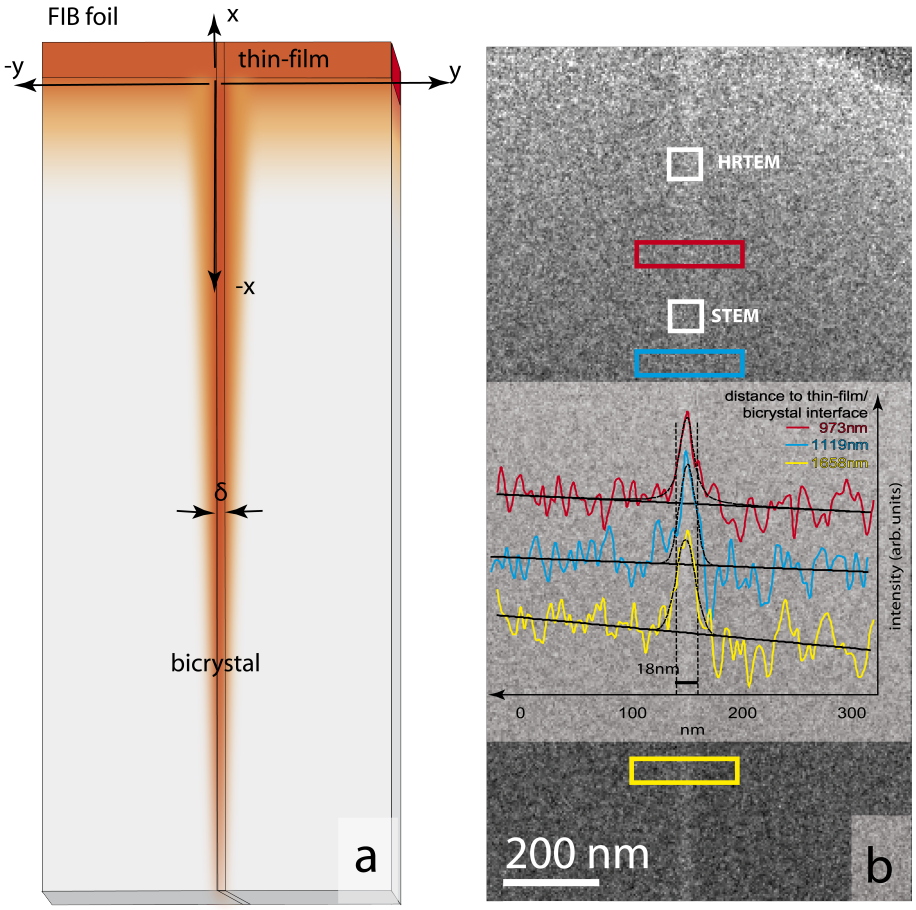

Figure 3.19: Grain boundary diffusion experiment. (a) Scheme of the experimental setup. Perpendicular to the grain boundary, a thin-film with different composition is deposited; red denotes high concentration of the diffusant. Fast diffusion along the grain boundary could result in a concentration distribution as illustrated. (b) Jump ratio map obtained with EELS by using the Yb M_5 1528 eV and M_4 1576 eV edges. A relatively constant zone of increased Yb concentration around the grain boundary compared to the crystal volumes is observed. This becomes evident in the profiles across the grain boundary, which monitor the Yb concentration perpendicular to the grain boundary with increasing distance from the diffusant source (which is located ~100 nm above the top of the figure). The profiles are shifted in intensity with respect to each other for clarity. The white boxes denote the position of the HRTEM (at ~780 nm) and STEM (at ~1050 nm) measurements shown in Figure 3.21.

which corresponds to length-scale of the diffusion process that we intend to study. Thickness correction using a thickness map is relatively unreliable and, therefore, the elemental maps presented here give only qualitative information on the decreasing Yb concentration along the grain boundary. The spatial resolution of EELS elemental maps is influenced by several factors, which are difficult to quantify. It is, for instance, influenced by sample drift during long exposure times, the energies of the characteristic electron energy losses of the element of interest, the peak to background ratio, and finally the quality of the image cross-correlation when the pre-peak and the peak map are subtracted.

HRTEM and Negative C_s imaging (NCSI)

In TEM, information on the atomic structure of a specimen is encoded in the electron wave field after it has passed through the volume of the sample. The varying potentials across the region being probed result in an exit wave field with locally varying phase shifts. Unfortunately, only the amplitude of this complex electron wave can be recorded by detectors and the phase information needs to be recovered through complex processing schemes described below. In order to optimise the phase recovery process an 'artificial phase shift' can be introduced in aberration-corrected instruments by choosing adequate values of spherical aberration and defocus. Negative C_s imaging is widely used to acquire focus series for phase reconstruction (e.g. Jia et al., 2003; Spence, 2003; Urban, 2007) as this method allows for enhanced imaging of low nuclear-charge atoms, such as oxygen. Furthermore, one should note that additional aberration-correction minimizes the point spread function of the microscope (Urban, 2007), so the local crystal site occupancy can be estimated more directly than on non-corrected instruments.

Samples for the HRTEM investigations were prepared using a dual beam FIB (FEI Strata 235), where a focused Ga^+ ion beam (FIB) and a field emission scanning electron column facilitate cutting and imaging from different directions. In situ sample manipulation with an Omniprobe microneedle along with Pt deposition facilitate the transfer and fixation of a chunk of sample material onto an Omniprobe TEM grid. This, in turn, allows for preparing very thin samples (∼30 nm). To

remove the amorphous surface layer produced during FIB milling (M. R. Lee et al., 2003; Song, 2009), the TEM-foils were subsequently thinned using a low angle low energy ion mill (LINDA) operated at 500 V. Additionally, the sample was plasma-cleaned prior to the TEM sessions using a Fishione plasma-cleaner.

The HRTEM investigations were performed on the TEAM0.5 microscope at the National Center for Electron Microscopy (Kisielowski et al., 2008), an improved FEI Titan^3, which can achieve a resolution of 0.5 Å at an acceleration voltage of 300 kV thanks to its two CEOS hexapole-type spherical aberration correctors. Aberration-correction reduces the point spread to very small values and the measured local intensities are determined by the respective atomic site occupation in the specimen (Urban, 2008), therefore interpretation of the local intensity increase in phase images of the electron exit wave is possible (Fig. 3.21a). The microscope is equipped with a high brightness Schottky field emission electron source (XFEG), a gun monochromator, and a high resolution Gatan Tridiem imaging filter. In addition to the gains in resolution, these hardware improvements provide a significantly increased operational flexibility and allow for high resolution imaging at low acceleration voltages. The HRTEM images presented here were thus acquired at 80 kV acceleration voltage to limit any beam damage caused by the high brightness of the electron source. Diffraction patterns and the HRTEM images of the proposed crystal structure were simulated using the MacTempas software package (see www.totalresolution.com for more information).

For the HRTEM image simulations, the following microscope parameters were chosen: accelerating voltage 80 kV, spherical aberration coefficient -0.01 mm, beam convergence 0.15 mrad, spread of defocus 10 Å. The HRTEM simulation was performed on a YAG bicrystal super-cell with the dimensions of $70\times140\times50$ nm^3 (corresponding to about 283600 unit cells of YAG).

Exit wave reconstruction (EWR) and iterative image simulation procedure

High resolution phase-contrast focal series and exit wave reconstruction, combined with image simulation, were used to gain information on the orientation of the two crystals with respect to each other (Fig. 3.20). A rotation of 36.9° around

the common <100> direction (Fig. 3.20d) of the bicrystal is read directly from the diffraction pattern. In order to minimize beam irradiation damage, convergent beam diffraction analysis was avoided. The diffraction pattern, which is relatively insensitive to slight misorientations (if Kikuchi lines are absent), served instead as a starting point for the iterative image simulations using the following procedure:

First, the exit wave was reconstructed from a focal series of sub-Ångstrom phase-contrast high resolution transmission electron micrographs (Fig. 3.20a). Then the orientation of the two crystals forming the grain boundary was built, and a super-unit-cell of the grain boundary structure was generated using the software KristalKit (Fig. 3.20 inset). The super-unit-cell was used to simulate the image using the parameters obtained from the exit wave reconstruction. Iteratively, we approached the real crystal to crystal orientation by comparing the simulated images (Fig. 3.20b) with the phase images (Fig. 3.20c) of the exit wave and adjusting the super-unit-cell of the grain boundary structure. Both exit wave reconstruction and image simulations were carried out using the software 'MacTempas'. We found that one crystal is rotated by about 12° (counterclockwise) around the <210> direction and about 6.5° perpendicular to this direction with respect to the second crystal. A change of up to 3° in the orientation of the lower crystal in our simulated bicrystal structure is negligible for the result.

In ideal imaging conditions and assuming single-scattering only at atomic sites, it is possibly to show that the intensity in phase images of the reconstructed exit wave depends on the atomic number Z as approximately $Z^{2/3}$ (Jinschek et al., 2004; Kisielowski et al., 2009). Note that this contrast also strongly depends on focus, which must be very accurately controlled and estimated to interpret the images correctly. The Z dependence can be used to obtain (qualitative) chemical information from a carefully reconstructed phase image of the exit wave and this has been done in the present study.

STEM using Z-contrast imaging

In contrast to the parallel beam used in HRTEM, in scanning transmission mode (STEM), a very fine electron probe is rastered serially across the region of interest

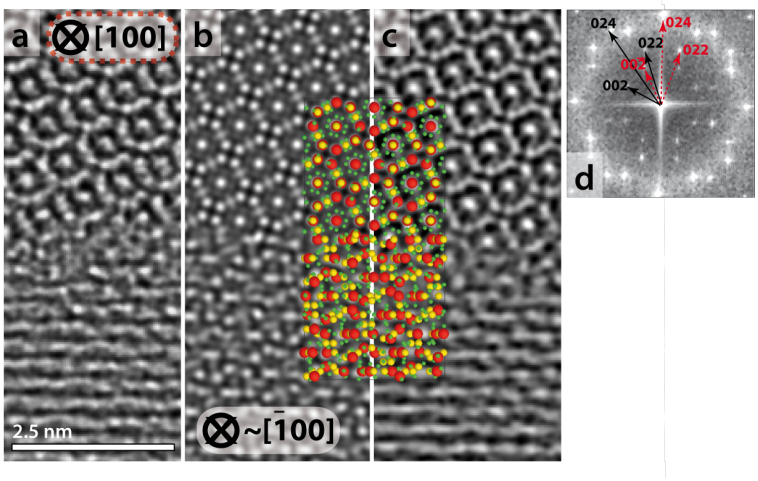

Figure 3.20: (a) HRTEM image at Scherzer defocus. The *structural* grain boundary width is less than 1 nm. (b) Simulated image, the bicrystal structure used for simulation is also shown. Y atoms are colored red, Al atoms are yellow and oxygen atoms are green. The oxygen atoms are drawn to a smaller scale for clarity. A near $\Sigma 5$ (210)/[100] grain boundary was simulated; from the diffraction pattern in (d), the rotation of 36.9° around the <100> direction was obtained. Two additional misorientations were needed to simulate the image correctly. First, a rotation of about 12° around the y-axis of the image (corresponding to the <210> direction of both crystals), and second a 6.5° rotation around the x-axis of the image. (c) Imaginary part of the reconstructed electron exit wave. (d) Diffraction pattern of the experimental image (a). The red arrows indicate the diffraction spots that correspond to the upper crystal, whereas the black arrows point at diffraction spots from the lower crystal.

to produce an image. An annular-shaped detector is employed to collect electrons that have been scattered to high angles by quasi-elastic interactions with inner shell electrons (K+L) or atomic nuclei in the specimen (Pennycook, 1989). It has been shown that, at sufficiently high angles, the scattering process is mostly Rutherford-like, so that the intensity integrated across a high angle annular dark field detector (HAADF) is directly related to the n-th power (n = 1.5-2) of the average atomic number Z of the column, on which the electron probe was positioned (Crewe & Wall, 1970; Pennycook, 1989). STEM-HAADF images are thus often referred to as Z-contrast images and can be directly used as a guide for chemical identification. Full direct quantitative comparison with simulations can also be achieved when all experimental parameters are carefully characterized (LeBeau et al., 2008).

STEM-HAADF images were acquired here on the TEAM0.5 microscope at 300 kV with a 30 mrad beam limiting aperture, resulting in an aberration-corrected probe size of about 0.7 Å. With the camera length settings used, the HAADF detector inner and outer angles were calibrated at 85 mrad and 350 mrad, respectively, ensuring that the recorded contrast was as devoid as possible of diffraction effects arising from medium to low angle diffraction (Hartel et al., 1996).

When evaluating single profiles extracted from either the phase image of the exit wave or the Z-contrast STEM image, it is notable that often sudden changes of intensity are observed. At such high resolution, just one additional Y-atom exchanged by an Yb-atom can result in higher intensities. This is expected, because the studied sample was only about 20 nm thick, corresponding to about 60 atoms in the atom column of interest. In pure YAG, Y would alternate with Al. Thus 30 Y (Z = 39) atom sites are available for Yb (Z = 70) exchange. As the atomic mass of Yb is ∼1.8 times the mass of Y, just one additional Yb atom changes the average atomic number of the atomic column by 2%. The contrast in a STEM image, assuming a dependence of $Z^{1.5}$, increases by about 4%. Assuming a dependence of Z^2, the intensity would increase already by 6.7%. Averaging over 10 profiles leads to smooth profiles (Fig. 3.21). To exclude potential bias by contamination or beam damage, we monitored the sample while measuring. In cases where this was not functional, we imaged the sample prior to and after measuring.

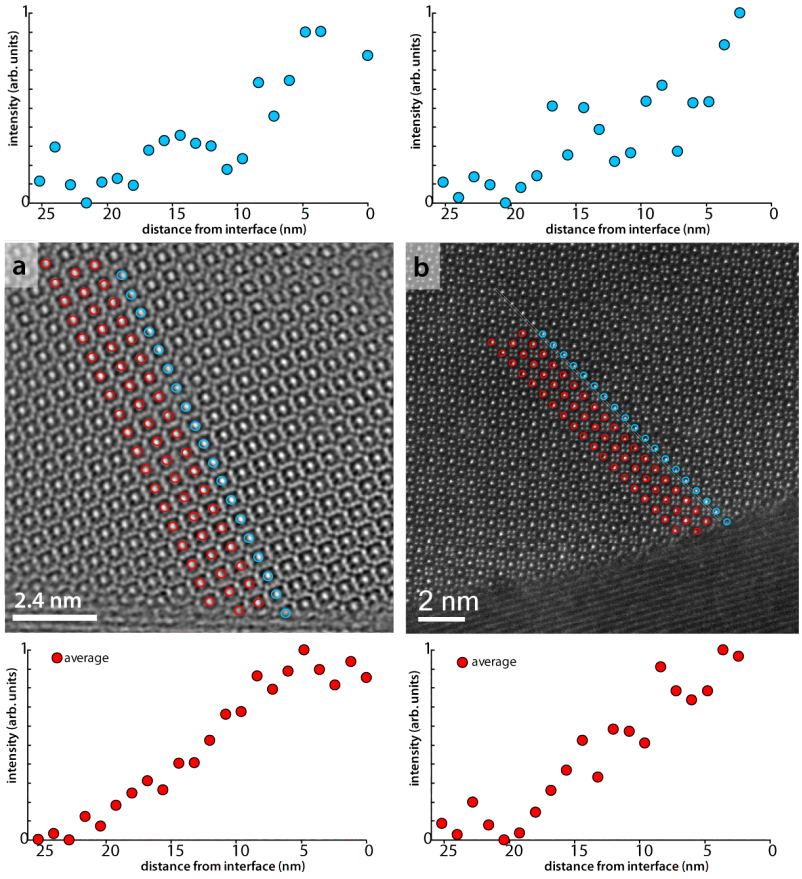

Figure 3.21: Intensity profiles in (a) the imaginary part of the reconstructed electron exit wave and (b) STEM Z-contrast image of the same grain boundary about 400 nm further away from the initial thin-film. The strong Z-contrast makes heavier atoms appear brighter. The aligned red circles refer to example profiles taken at the atom columns of interest with an integration width of about 0.1 nm. The profiles run along the [010] direction. The profiles above the images are single profiles, whereas the profiles below the images are averages over ten profiles. The intensity increases towards the grain boundary. In both images, the sample is oriented with its [100] direction parallel to the incident beam, as in Fig. 3.20. The approximate locations of the images are indicated in Fig. 3.19.

Profile extraction

The Gatan Digital Micrograph software was used for the analyses of the STEM and the energy filtered transmission electron micrographs (EFTEM). The profiles were aligned thoroughly to prevent any falsification by angular (with respect to a specific crystallographic direction) analyses. The profiles are aligned along the crystallographic direction [010] to obtain the intensity change in the atom columns normally occupied by Y and Al. Therefore, the profiles are not perpendicular to the grain boundary. The atomic resolved profiles extend from the interface in only one crystal, because in an asymmetric bicrystal only one crystal can be aligned parallel to the incident electron beam. Therefore the profiles were mirrored at the interface to extract the FWHM, which facilitates comparison to the EELS profiles. Subsequent curve fitting using the software PEAKFIT yields the full widths at half maximum (FWHM) of a fitted Gaussian shaped peak, the stated uncertainty represents the 2σ least square error as obtained from the fit.

3.4.5 Results

The elemental jump ratio map using the high loss edges of Yb (M_5 1528 eV; M_4 1576 eV) (Fig. 3.19b) shows the high concentration of Yb at the grain boundary. Even though the elemental map gives only qualitative information on the Yb-Y interdiffusion, the profiles perpendicular to the grain boundary (Fig. 3.19b) show that the signal from the diffusant (Yb) is relatively constant with increasing distance from the diffusant source (compare the profiles in Fig. 3.19b). The three profiles are taken at distances of 973 nm, 1173 nm, and 1654 nm from the thin-film/bicrystal interface. The fitted profiles have a mean FWHM of 17.9($\pm$3) nm. This width is confirmed by the two atomic imaging methods (HRTEM-EWR and STEM). In both images the intensity increases towards the grain boundary (Fig. 3.21). The intensity scatters significantly (the intensity results from only 60 atoms, see *methods*) in individual profiles (Fig. 3.21 upper profiles), but gets smoother when 10 profiles are averaged (Fig. 3.21 lower profiles).

The FWHM obtained from the HRTEM-EWR (at 780 nm, see Fig. 3.19) and the STEM profile (at 1050 nm, see Fig. 3.19) are both about 20 nm, even though

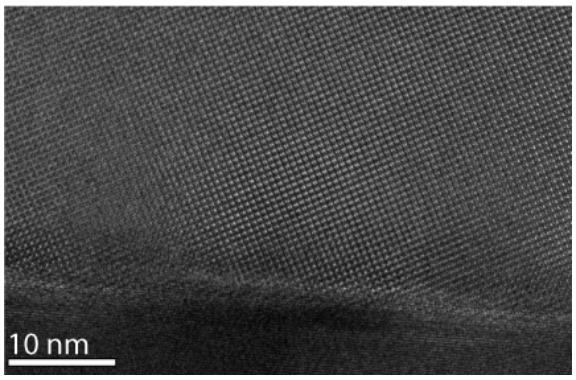

Figure 3.22: Lattice fringe image of the grain boundary at a relatively thick part of the sample. The upper crystal is aligned with the [100] direction parallel to the incident beam. Above the grain boundary, two distorted lattice parts (left and right from the image centre) are visible. They coincide with steps at the grain boundary plane. They extend about 10 to 15 nm into the perfect crystal lattice.

they where acquired approximately 400 nm apart. The averaged profile extracted from the phase image of the exit wave has a FWHM of 24.5(±2.9) nm (3.21). The similar obtained profile of the Z-contrast intensity shows a FWHM of 22.7(±3.6) nm (Fig. 3.21). If one corrects for the inclination of the profiles with respect to the EELS profiles, the FWHM are 21.2 nm and 19.7 nm for the EWR and STEM profiles, respectively.

The image of the crystal lattice adjacent to the grain boundary is blurred over a range of 10-15 nm (Fig. 3.22).

3.4.6 Discussion

The EELS Yb elemental maps show higher intensities along the grain boundary compared to the crystal volume. To verify that this corrpesonds to a real increase of Yb concentration in the grain boundary region, we must exclude a preferentially thinned grain boundary and bias during data processing. Both can be excluded as HRTEM-EWR and STEM also show an intensity increase of comparable dimensions in the boundary region. These are independent methods and complementary with respect to constrast formation, excluding a thinner grain boundary region. Furthermore, the STEM data are unprocessed, thus artefacts arising from data processing are impossible.

All three chemically sensitive imaging methods show that the width (FWHM) of the chemically altered region is homogenous over several μm. However, the concentration of Yb along this slab of constant thickness decreases as shown in an EDS profile published elsewhere (K. Marquardt et al., submitted).

Figure 3.22 shows blurred parts in the upper crystal lattice parallel to the grain boundary, which extend over 8 to 12 nm. We surmise that these parts are distorted due to lattice misfit at the grain boundary in accordance with Hartmann et al. (2010), who studied the same bicrystal. We interpret this strained area as the reason for locally enhanced diffusion, because it incidences well with the chemically altered region ($\sim$20 nm, i.e. $\sim$10 nm in each crystal). Therefore, we infer that these $\sim$20($\pm$3) nm correspond to the *effective* grain boundary width δ. This is in agreement with the recent observation of strain fields at dislocation cores (and therefore defects) that lead to chemical alteration and local diffusion (Arredondo et al., 2010). The *effective* grain boundary width is a highly permeable slab of $\sim$20 nm surrounding the *structural* grain boundary (about 1 nm). Our observations imply that the *effective* grain boundary width is about 40 times larger than common assumptions of 0.5 nm (Chadwick & Smith, 1976).

We agree with the speculation of Mistler and Coble (1974), that the *effective* grain boundary width probably depends on temperature. Furthermore, we think that the *effective* grain boundary width depends on the extension of the strain field of the grain boundary. This lead us surmise that the *effective* grain boundary width is a function of misorientation. Consequently, this could imply that grain boundary diffusivities D_{gb} are less variable than previously proposed, because the change in the product of D_{gb} and δ could be partially accounted for by the proposed large variations in δ. This implication remains to be experimentally tested.

In that respect, new developments in aberration corrected transmission microscopy, which focus on lower acceleration voltage and gentle imaging modes (Sader et al., 2010), are particularly promising as they will allow a more systematic study of the variations in *effective* grain boundary width with enhanced precision on the chemical variations thanks to atomically resolved EELS at low effective electron dose.

3.4.7 Conclusion

Our study results in three major findings. First, we show that the *effective* grain boundary width can experimentally be determined. Second, the *effective* grain boundary width in YAG at the present conditions is 20($\pm$3) nm, which is $\sim$40 times larger than the standard assumption of 0.5 nm used to calculate grain boundary diffusion coefficients (Kaur et al., 1995). Third, we illustrate directly that the chemically altered grain boundary region corresponds to the strained/distorted region around the structural grain boundary, which is expected based on theoretical considerations (S. White, 1973; Kingery, 1974; Pond & Vlachavas, 1983). Our experimental assemblage of bicrystal and thin-film is gathered in a cuboid of focused ion beam (FIB) foil dimensions (10$\times$12$\times$0.02-0.06 μm^3). This minuscule volume contains the total of our far-reaching results and shows the enormous capabilities of miniaturized samples for geological studies.

Acknowledgments

This work was partially carried out at the National Centre for Electron Microscopy, Lawrence Berkeley National Laboratory, and was supported by the Department of Science, Department of Basic Energy Sciences, of the US Department of Energy, under Contract No. DE-AC02- 05CH11231. K. M. acknowledges financial support for her research stay at NCEM Berkeley from the German Research Foundation (DFG) and thanks Emmanuel Gardés for his thoughtful comments on the problematic of the grain boundary width. Furthermore, the productive discussions with Hauke Marquardt are highly appreciated. K. M. highly appreciates the financial support from the Christiane Nüsslein Volhard (CNV) foundation.

Chapter 4

Outlook

During the wafer direct bonding experiments, I observed that the features that occur during the progress of bonding strongly resemble those that are attributed to crack healing. This observation led to the idea that wafer direct bonding might be a promising technique to study crack healing with well defined geometries. Crack healing properties of materials are important for industrial applications (Takahashi et al., 2006) and are crucial for the understanding of shear zone dynamics and deep crust earthquakes, to name just a few geological relevant scenarios. The healing processes have been in the focus of research for many decades, but are far from being fully understood and further research with new approaches seems very fruitful. Well characterized surfaces, in addition to defined geometries, could facilitate the comparison to computer simulations. This combination could be the key to understand the physico-chemical properties that govern crack healing processes. In rocks, healing-structures (Olgaard & Fitz Gerald, 1993) are often observed in connection with microcracks (Richter & Simmons, 1977; Sprunt & Nur, 1979; Shirey et al., 1980) and it is interesting to note that also the morphology of intergranular films often shows features comparable to those accompanying crack healing (Lange & Clarke, 1982). This might indicate that similar processes are involved in rearranging thin films and crack healing. Laboratory studies on crack healing processes are complicated by the large amount of uncontrolled variables that influence the healing process, including well defined surfaces.

I conclude that better experimental constraints are needed to understand and model crack healing processes. As part of this thesis, I conducted a suite of experiments on geometrically simple crack geometries (Fig. 4.1). Two atomically flat wafers of YAG single crystals were brought into contact at room conditions. Subsequent annealing at 400°C under vacuum led to the initial geometry (only area 1 present). This geometry needs to be characterized and then is the basis for the following healing process (Fig. 4.1). Such experiments are a promising approach to study crack healing using simple geometries as a fundament to prove and extend the theory of crack healing, in combination with computer simulations, to the more complicated geometries and chemical environments found in the Earth. I suggest that studies using well characterized starting materials and precisely defined healing

geometries should be performed. This could be realized using the principle of the wafer bonding method, which would also facilitate that the experimental setup is reproducible. Elevated temperature annealing could be performed in different atmospheres with controlled oxygen or hydrogen fugacity. To investigate the healing process, a combination of conventional light microscopy, interference microscopy, atomic force microscopy, computer simulations, and TEM seems most gainful.

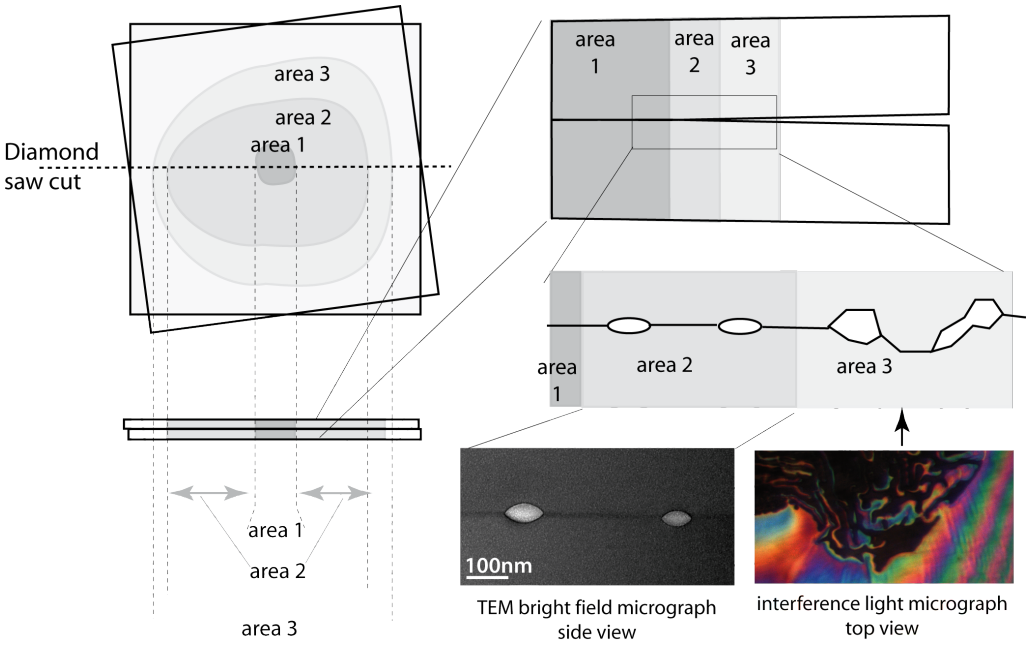

Figure 4.1: Scheme of the healing process and the evolution of healing structures. Left is a top view of the two wafers and the regions of healing that form during annealing at elevated temperatures. Below is a side view. Area 1 is the region where wafer bonding is initiated. This area is free of any inclusions, bubbles, etc. Area 2 often contains bubbles, sometimes with inverse crystal morphology. It formes during high temperature annealing ($T > 0.6 \times T_m$). Area 3 develops either during long annealings and/or at high temperatures. It shows vermicular structures. On the right hand side, subsequent enlargements of the healing structures are shown. Observations were done with TEM and interference light microscopy. The TEM micrograph shows a side view of the healed crack, two bubbles formed at the interface. The image on the right is is a top view, obtained by interference light microscopy. The dark grey area is bonded and the different colored circles are rings of Newton, which formed due to interference in the wedge of air between the two crystal plates. This simple geometry facilitates crack healing studies, where the starting material is well characterized and geometry can be controlled.

Bibliography

Abart, R., Kunze, K., Milke, R., Sperb, R. Heinrich, W. (2004). Silicon and oxygen self diffusion in enstatite polycrystals; the Milke et al. (2001) rim growth experiments revisited. *Contributions to Mineralogy and Petrology*, *147*(6), 633-646.

Abart, R., Petrishcheva, E., Fischer, F. D. Svoboda, J. (2009). Thermodynamic model for diffusion controlled reaction rim growth in a binary system; application to the forsterite-enstatite-quartz system. *American Journal of Science*, *309*(2), 114-131.

Arredondo, M., Ramasse, Q. M., Weyland, M., Mahjoub, R., Vrejoiu, I., Hesse, D. et al. (2010). Direct evidence for cation non-stoichiometry and cottrell atmospheres around dislocation cores in functional oxide interfaces. *Advanced Materials*, *22*, 1-5.

Avila-Paredes, H. J., Choi, K., Chen, C.-T. Kim, S. (2009). Dopant-concentration dependence of grain-boundary conductivity in ceria: A space-charge analysis. *Journal of Materials Chemistry*, *19*, 4837-4842.

Balluffi, R. W. Sutton, A. (1996). Why should we be interested in the atomic structure of interfaces? *Materials Science Forum: Intergranular and Interphase Boundaries in Materials*, *207-209*, 1-12.

Barmak, K., Kim, J., Kim, C. S., Archibald, W. E., Rohrer, G. S., Rollett, A. D. et al. (2006). Grain boundary energy and grain growth in Al films: Comparison of experiments and simulations. *Scripta Materialia*, *54*(6), 1059-1063.

Béjina, F., Jaoul, O. Liebermann, R. C. (2003). Diffusion in minerals at high pressure: a review. *Physics of The Earth and Planetary Interiors*, *139*(1-2), 3-20.

Bons, A. J., Drury, M. R., Schryvers, D. Zwart, H. J. (1990). The nature of grain boundaries in slates; implications for mass transport processes during low temperature metamorphism. *Physics and Chemistry of Minerals*, *17*(5), 402-408.

Bosman, M., Keast, V. J., García-Muñoz, J. L., D'Alfonso, A. J., Findlay, S. D. Allen, L. J. (2007). Two-dimensional mapping of chemical information at atomic resolution. *Physical Review Letters*, *99*(8), 086102.

Boye, P. (2009). *Nanofocusing refractive x-ray lenses.* Unpublished doctoral dissertation, Technische Universität Dresden.

Brandon, D. G. (1966). The structure of high-angle grain boundaries. *Acta Metallurgica*, *14*, 1479-1484.

Brown, K. R. Bonnell, D. A. (1998). Cation segregation to yttrium aluminum garnet (111) surfaces. *Surface Science*, *414*(3), 341-352.

Budke, E., Surholt, T., Prokofjev, S. I., Shvindlerman, L. S. Herzig, C. (1999). Tracer diffusion of Au and Cu in a series of near Σ=5 (310)[001] symmetrical Cu tilt grain boundaries. *Acta Materialia*, *47*(2), 385-395.

Byerly, G. R. Vogel, T. A. (1973). Grain boundary processes and development of metamorphic plagioclase. *Lithos*, *6*(2), 183-202.

Campbell, G. H. (1996). Σ5 (210)/[001] symmetric tilt grain boundary in yttrium aluminum garnet. *Journal of the American Ceramic Society*, *79*(11), 2883-2891.

Campbell, G. H., Plitzko, J. M., King, W. E., Foiles, S. M., Kisielowski, C. Duscher, G. J. M. (2004). Copper segregation to the Σ5 (310)/[001] symmetric tilt grain boundary in aluminum. *Interface Science*, *12*(2), 165-174.

Carter, C. B. Föll, H. (1978). The contrast from incoherent twin interfaces observed using the weak-beam technique. *Scripta Metallurgica*, *12*(12), 1135-1139.

Carter, C. B., Föll, H., Ast, D. G. Sass, S. L. (1981). Electron diffraction and microscopy studies of the structure of grain boundaries in silicon. *Philosophical Magazine A*, *43*(2), 441-467.

Caslavsky, J. L. Viechnicki, D. J. (1980). Melting behaviour and metastability of yttrium aluminium garnet (YAG) and $YAlO_3$ determined by optical differential thermal analysis. *Journal of Materials Science*, *15*(7), 1709-1718.

Chadwick, G. A. Smith, D. A. (1976). *Grain boundary structure and properties.* Academic Press, London.

Chen, D., Jordan, E. H., Renfro, M. W. Gell, M. (2009). Dy:YAG phosphor coating using the solution precursor plasma spray process. *Journal of the American Ceramic Society*, *92*(1), 268-271.

Chen, Z.-h., Li, J.-t., Xu, J.-j. Hu, Z.-g. (2008). Fabrication of YAG transparent ceramics by two-step sintering. *Ceramics International*, *34*(7), 1709-1712.

Cherniak, D. J. (1998). Rare earth element and gallium diffusion in yttrium aluminum garnet. *Physics and Chemistry of Minerals*, *26*(2), 156-163.

Cho, J., Chan, H. M., Harmer, M. P. Rickman, J. M. (1998). Influence of yttrium doping on grain misorientation in aluminum oxide. *Journal of the American Ceramic Society*, *81*(11), 3001-3004.

Chrisey, D. B. Hubler, G. K. (Eds.). (2003). *Pulsed laser deposition of thin films.* Wiley VCH.

Christophersen, M., Carstensen, J., Rönnebeck, S., Jäger, C., Jäger, W. Föll, H. (2001). Crystal orientation dependence and anisotropic properties of macropore formation of p- and n-type

silicon. *Journal of The Electrochemical Society*, *148*(6), E267-E275.

Chung, Y.-C., Kim, C. K. Wuensch, B. J. (2000). Calculation of the contribution to grain boundary diffusion in ionic systems that arises from enhanced defect concentrations adjacent to the boundary. *Journal of Applied Physics*, *87*(6), 2747-2752.

Clarke, D. R. Wolf, D. (1986). Grain boundaries in ceramics and at ceramic-metal interfaces. *Materials Science and Engineering*, *83*(2), 197-204.

Cliff, G. Lorimer, G. (1975). The quantitative analysis of thin specimens. *Journal of Microscopy*, *103*, 203-207.

Coble, R. L. (1961). Sintering crystalline solids. I. intermediate and final state diffusion models. *Journal of Applied Physics*, *32*(5), 787-792.

Constable, S. Duba, A. (2002). Diffusion and mobility of electrically conducting defects in olivine. *Physics and Chemistry of Minerals*, *29*(7), 446-454.

Crank, J. (1975). *The mathematics of diffusion*. Oxford University Press, New York.

Crewe, A. V. Wall, J. (1970). A scanning microscope with 5 Å resolution. *Journal of Molecular Biology*, *48*(3), 375-393.

Cunningham, B., Strunk, H. P. Ast, D. G. (1982). High resolution electron microscopy of a $\Sigma = 27$ boundary in silicon. *Scripta Metallurgica*, *16*(4), 349-352.

Czochralski, J. (1918). Ein neues Verfahren zur Messung der Kristallisationsgeschwindigkeit der Metalle. *Zeitschrift für physikalische Chemie*, *92*, 219-221.

Dillon, S. J. Harmer, M. P. (2007). Multiple grain boundary transitions in ceramics: A case study of alumina. *Acta Materialia*, *55*(15), 5247-5254.

Dillon, S. J. Rohrer, G. S. (2009a). Characterization of the grain-boundary character and energy distributions of yttria using automated serial sectioning and EBSD in the FIB. *Journal of the American Ceramic Society*, *92*(7), 1580-1585.

Dillon, S. J. Rohrer, G. S. (2009b). Mechanism for the development of anisotropic grain boundary character distributions during normal grain growth. *57*(1), 1-7.

Divinski, S., Ribbe, J., Schmitz, G. Herzig, C. (2007). Grain boundary diffusion and segregation of Ni in Cu. *Acta Materialia*, *55*(10), 3337-3346.

Divinski, S. Wilde, G. (2008). Diffusion in ultrafine grained materials. In *Materials science forum* (Vol. 587-586, p. 1012-1017). Trans Tech Publications, Switzerland.

Dobrzycki, L., Bulska, E., Pawlak, D. A., Frukacz, Z. Wozniak, K. (2004). Structure of YAG crystals doped/substituted with erbium and ytterbium. *Inorganic Chemistry*, *43*, 7656-7664.

Dobson, D. P., Dohmen, R. Wiedenbeck, M. (2008). Self-diffusion of oxygen and silicon in $MgSiO_3$ perovskite. *Earth and Planetary Science Letters*, *270*(1-2), 125-129.

Dohmen, R., Becker, H.-W. Chakraborty, S. (2007). Fe–Mg diffusion in olivine I: experimental determination between 700 and 1,200°C as a function of composition, crystal orientation and

oxygen fugacity. *Physics and Chemistry of Minerals*, *34*(6), 389-407.

Dohmen, R., Becker, H.-W., Mei"sner, E., Etzel, T. Chakraborty, S. (2002). Production of silicate thin films using pulsed laser deposition (PLD) and applications to studies in mineral kinetics. *European Journal of Mineralogy*, *14*, 1155-1168.

Duffy, D. M. Tasker, P. W. (1984). A calculation of the formation energies of intrinsic defects near grain boundaries in NiO. *Philosophical Magazine A*, *50*(2), 143-154.

Elliott, D. (1973). Diffusion flow laws in metamorphic rocks. *Geological Society of America Bulletin*, *84*(8), 2645-2664.

Ernst, F., Kienzle, O. Rühle, M. (1999). Structure and composition of grain boundaries in ceramics. *Journal of the European Ceramic Society*, *19*(6-7), 665-673.

Evans, A. G. Charles, E. A. (1977). Strength recovery by diffusive crack healing. *Acta Metallurgica*, *25*(8), 919-927.

Fabris, S. Elsässer, C. (2001). $\Sigma 13$ $(10\bar{1}4)$ twin in α-Al_2O_3: A model for a general grain boundary. *Physical Review B*, *64*(24), 245117.

Fan, D., Chen, L.-Q. Chen, S. P. (1997). Effect of grain boundary width on grain growth in a diffuse-interface field model. *Materials Science and Engineering A*, *238*(1), 78-84.

Farver, J. R. Yund, R. A. (1991). Measurement of oxygen grain boundary diffusion in natural, fine-grained, quartz aggregates. *Geochimica et Cosmochimica Acta*, *55*(6), 1597-1607.

Feldman, L. C. Mayer, J. W. (1986). *Fundamentals of surface and thin film analysis*. Prentice Hall.

Fensin, S. J., Olmsted, D., Buta, D., Asta, M., Karma, A. Hoyt, J. J. (2010). Structural disjoining potential for grain-boundary premelting and grain coalescence from molecular-dynamics simulations. *Physical Review E*, *81*(3), 031601.

Fick, A. (1855). Über Diffusion. *Annalen der Physik und Chemie*, *94*, 95-86.

Fiddicke, J. Oelgart, G. (1985). The importance of the excitation volume for the determination of the minority carrier diffusion length. *Physica status solidi (a)*, *87*(1), 383-389.

Fisher, J. (1951). Calculations of diffusion penetration curves for surface and grain boundary diffusion. *Journal of Applied Physics*, *22*(1), 74-77.

Föll, H. Ast, D. (1979). TEM observations on grain boundaries in sintered silicon. *Philosophical Magazine A*, *40*(5), 589-610.

Frank, F. C. (1951). LXXXIII. crystal dislocations – elementary concepts and definitions. *Philosophical Magazine Series 7*, *42*(331), 809-819.

Frolov, T. Mishin, Y. (2009). Molecular dynamics modeling of self-diffusion along a triple junction. *Physical Review B*, *79*(17), 174110.

Ganguly, J., Cheng, W. Chakraborty, S. (1998). Cation diffusion in aluminosilicate garnets: experimental determination in pyrope-almandine diffusion couples. *Contributions to Mineralogy*

and Petrology, *131*(2), 171-180.

Gardés, E., Jaoul, O., Montel, J.-M., Seydoux-Guillaume, A.-M. Wirth, R. (2006). Pb diffusion in monazite; an experimental study of Pb^{2+} + Th^{4+} –>$2Nd^{3+}$ interdiffusion. *Geochimica et Cosmochimica Acta*, *70*(9), 2325-2336.

Gardés, E. Montel, J.-M. (2009). Opening and resetting temperatures in heating geochronological systems. *Contributions to Mineralogy and Petrology*, *158*(2), 185-195.

Gardés, E., Montel, J.-M., Seydoux-Guillaume, A.-M. Wirth, R. (2007). Pb diffusion in monazite; an experimental study of Pb^{2+} <–> Ca^{2+} interdiffusion. *Geochimica et Cosmochimica Acta*, *71*, 4036-4043.

Gemming, T., Nufer, S., Kurtz, W. Ruhle, M. (2003). Structure and chemistry of symmetrical tilt grain boundaries in α-Al_2O_3: I. Bicrystals with "clean" interface. *Journal of the American Ceramic Society*, *86*(4), 581-589.

Geusic, J. E., Marcos, H. M. Van Uitert, L. G. (1964). Laser oscillations in Nd-doped yttrium aluminum, yttrium gallium and gadolinium garnets. *Applied Physics Letters*, *4*(10), 182-184.

Gifkins, R. (1976). Grain-boundary sliding and its accommodation during creep and superplasticity. *Metallurgical and Materials Transactions A*, *7*(7), 1225-1232.

Gleiter, H. Chalmers, B. (1972). *High-angle grain boundaries*. Pergamon Press, Oxford.

Gösele, U., Tong, Q. Y., Schumacher, A., Kräuter, G., Reiche, M., Plö"sl, A. et al. (1999). Wafer bonding for microsystems technologies. *Sensors and Actuators A: Physical*, *74*(1-3), 161-168.

Guan, Z. (2003). *Korngrenzstrukturen, Fremdatomdiffusion und Homogenität in nanokristallinen Metallen und Legierungen*. Unpublished doctoral dissertation, Universität des Saarlandes.

Gupta, T. K. (1975). Crack healing in thermally shocked MgO. *Journal of the American Ceramic Society*, *58*(3-4), 143-143.

Hailong, Z. Jun, S. (2002). Morphological evolution during diffusive healing of internal cracks within grains of α-iron. *Acta Mechanica Sinica*, *18*(5), 516-527.

Haisma, J., Spierings, B. A. C. M., Biermann, U. K. P. Gorkum, A. A. van. (1994). Diversity and feasibility of direct bonding: a survey of a dedicated optical technology. *Applied Optics*, *33*(7), 1154-1168.

Hanke, M., Dubslaff, M., Schmidbauer, M., Boeck, T., Schoder, S., Burghammer, M. et al. (2008). Scanning x-ray diffraction with 200 nm spatial resolution. *Applied Physics Letters*, *92*(19), 193109.

Harendt, C., Graf, H.-G., Höfflinger, B. Penteker, E. (1992). Silicon fusion bonding and its characterization. *Journal of Micromechanics and Microengineering*, *2*, 113-116.

Harris, K. E., Singh, V. V. King, A. H. (1998). Grain rotation in thin films of gold. *Acta Materialia*, *46*(8), 2623-2633.

Harrison, L. G. (1961). Influence of dislocations on diffusion kinetics in solids with particular

reference to alkali halides. *Transactions of the Faraday Society*, *57*, 1191-1199.

Hartel, P., Rose, H. Dinges, C. (1996). Conditions and reasons for incoherent imaging in STEM. *Ultramicroscopy*, *63*(2), 93-114.

Hartmann, K., Wirth, R., Dohmen, R., Dresen, G. Heinrich, W. (2008). Diffusion in synthetic grain boundaries. In S. Richter A. Schwedt (Eds.), *EMC 2008 materials science* (Vol. 2, p. 817). Springer, Berlin.

Hartmann, K., Wirth, R. Heinrich, W. (2010). Synthetic *near* Σ5 (210)/[100] grain boundary in YAG fabricated by direct bonding: structure and stability. *Physics and Chemistry of Minerals*, *37*(5), 291-300.

Haynes, C. W. Smoluchowski, R. (1955). Grain boundary diffusion in a body-centered cubic lattice. *Acta Metallurgica*, *3*(2), 130-134.

Heinemann, S., Wirth, R. Dresen, G. (2001). Synthesis of feldspar bicrystals by direct bonding. *Physics and Chemistry of Minerals*, *28*(10), 685-692.

Heinemann, S., Wirth, R. Dresen, G. (2003). TEM study of a special grain boundary in a synthetic K-feldspar bicrystal: Manebach twin. *Physics and Chemistry of Minerals*, *30*(3), 125-130.

Heinemann, S., Wirth, R., Gottschalk, M. Dresen, G. (2005). Synthetic [100] tilt grain boundaries in forsterite: 9.9 to 21.5°. *Physics and Chemistry of Minerals*, *32*(4), 229-240.

Herbeuval, I., Biscondi, M. Goux, C. (1973). Influence of intercrystalline structure on the diffusion of zinc in symmetrical bending boundaries of aluminum. *Mem. Sci. Rev. Met.*, *70*(1), 39-46.

Hofmann, S. (1998). Sputter depth profile analysis of interfaces. *Reports on Progress in Physics*, *61*(7), 827-888.

Hondros, E. D. (1976). Grain boundary segregation: assessment of investigative techniques. In G. A. Chadwick D. A. Smith (Eds.), *Grain boundary structure and properties.* Academic Press, London.

Humphreys, F. J. Hatherly, M. (1996). *Recrystallization and related annealing phenomena.* Pergamon, Oxford.

Ikesue, A. Aung, Y. L. (2006). Synthesis and performance of advanced ceramic lasers. *Journal of the American Ceramic Society*, *89*(6), 1936-1944.

Ikesue, A., Kamata, K. Yoshida, K. (1996). Effects of neodymium concentration on optical characteristics of polycrystalline Nd:YAG laser materials. *Journal of the American Ceramic Society*, *79*(7), 1921-1926.

Ikesue, A., Kinoshita, T., Kamata, K. Yoshida, K. (1995). Fabrication and optical properties of high-performance polycrystalline Nd:YAG ceramics for solid-state lasers. *Journal of the American Ceramic Society*, *78*(4), 1033-1040.

Jaoul, O. Béjina, F. (2005). Empirical determination of diffusion coefficients and geospeedometry. *Geochimica et Cosmochimica Acta*, *69*(4), 1027-1040.

Jaoul, O., Sautter, V. Abel, F. (1991). Nuclear microanalysis; a powerful tool for measuring low atomic diffusivity with mineralogical applications. *Advances in Physical Geochemistry*, *8*, 198-220.

Jia, C. L., Lentzen, M. Urban, K. (2003). Atomic-resolution imaging of oxygen in perovskite ceramics. *Science*, *299*(5608), 870-873.

Jiménez-Melendo, M., Haneda, H. Nozawa, H. (2001). Ytterbium cation diffusion in yttrium aluminum garnet (YAG) - implications for creep mechanisms. *Journal of the American Ceramic Society*, *84*(10), 2356-2360.

Jinschek, J. R., Erni, R., Gardner, N. F., Kim, A. Y. Kisielowski, C. (2004). *Local indium segregation and band structure in high efficiency green light emitting InGaN/GaN diodes.* LBNL Paper 56655.

Joesten, R. (1991). Grain-boundary diffusion kinetics in silicate and oxide minerals. In *Diffusion, atomic ordering, and mass transport; selected topics in geochemistry* (Vol. 8, p. 345-395). Springer, New York.

Joesten, R. Fisher, G. (1988). Kinetics of diffusion-controlled mineral growth in the Christmas Mountains (Texas) contact aureole. *Geological Society of America Bulletin*, *100*(5), 714-732.

Johnson, C. L., Hßtch, M. J. Buseck, P. R. (2004). Nanoscale waviness of low-angle grain boundaries. *Proceedings of the National Academy of Sciences*, *101*(52), 17936-17939.

Kaiser, D. L., Holtzberg, F., Chisholm, M. F. Worthington, T. K. (1987). Growth and microstructure of superconducting $YB_2Cu_3O_x$ single crystals. *Journal of Crystal Growth*, *85*(4), 593-598.

Kaneko, K., Kawasaki, M., Nagano, T., Tamari, N. Tsurekawa, S. (2000). Determination of the chemical width of grain boundaries of boron- and carbon-doped hot-pressed β-SiC by HAADF imaging and ELNES line-profile. *Acta Materialia*, *48*(4), 903-910.

Kaur, I., Mishin, Y. Gust, W. (1995). *Fundamentals of grain and interphase boundary diffusion* (3 ed.). Wiley and Sons, Chichester.

Keller, L. M., Wirth, R., Rhede, D., Kunze, K. Abart, R. (2008). Asymmetrically zoned reaction rims: assessment of grain boundary diffusivities and growth rates related to natural diffusion-controlled mineral reactions. *Journal of Metamorphic Geology*, *26*(1), 99-120.

Kim, C.-S., Rollett, A. D. Rohrer, G. S. (2006). Grain boundary planes: New dimensions in the grain boundary character distribution. *Scripta Materialia*, *54*(6), 1005-1009.

Kim, M. J. Carpenter, R. W. (2002). Heterogeneous silicon integration by ultra-high vacuum wafer bonding. In *3rd international conference on alternative substrate technology (ICAST)* (p. 849-854).

Kimoto, K., Asaka, T., Nagai, T., Saito, M., Matsui, Y. Ishizuka, K. (2007). Element-selective imaging of atomic columns in a crystal using STEM and EELS. *Nature*, *450*(7170), 702-704.

Kimura, S., Yasuda, E., Sakaki, M., Kim, H. J. Moriyoshi, Y. (1986). Grain boundaries of MgO bicrystals. *The Ceramic Society of Japan*, *94*(8), 795-800.

Kingery, W. D. (1974). Plausible concepts necessary and sufficient for interpretation of ceramic grain-boundary phenomena: II, solute segregation, grain-boundary diffusion, and general discussion. *Journal of the American Ceramic Society*, *57*(2), 74-83.

Kisielowski, C., Freitag, B., Bischoff, M., Lin, H. van, Lazar, S., Knippels, G. et al. (2008). Detection of single atoms and buried defects in three dimensions by aberration-corrected electron microscope with 0.5-Å information limit. *Microscopy and Microanalysis*, *14*(5), 469-477.

Kisielowski, C., Specht, P., Alloyeau, D., Erni, R. Ramasse, Q. (2009). Aberration-corrected electron microscopy imaging for nanoelectronics applications. In D. Seiler et al. (Eds.), *Frontiers of characterization and metrology for nanoelectronics* (Vol. 1173, p. 231-241). American Institute of Physics Conference Proceedings.

Kliewer, K. L. Koehler, J. S. (1965). Space charge in ionic crystals. I. General approach with application to NaCl. *Physical Review*, *140*(4A), A1226.

Klugkist, P., Aleshin, A. N., Lojkowski, W., Shvindlerman, L. S., Gust, W. Mittemeijer, E. J. (2001). Diffusion of Zn along tilt grain boundaries in Al: pressure and orientation dependence. *Acta Materialia*, *49*(15), 2941-2949.

Kótai, E. (1994). Computer methods for analysis and simulation of RBS and ERDA spectra. *Nuclear Instruments and Methods in Physics Research Section B: Beam Interactions with Materials and Atoms*, *85*(1-4), 588-596.

Kuklja, M. M. (2000). Defects in yttrium aluminium perovskite and garnet crystals: atomistic study. *Journal of Physics: Condensed Matter*, *12*(13), 2953-2967.

Kuklja, M. M. Pandey, R. (1999). Atomistic modeling of native point defects in yttrium aluminum garnet crystals. *Journal of the American Ceramic Society*, *82*(10), 2881-2886.

Kuwano, H., Ouyang, H. Fultz, B. (1992). A Mössbauer spectrometry study of nanophase Cr–Fe synthesized by mechanical alloying: A measurement of grain boundary width. *Nanostructured Materials*, *1*(2), 143-148.

Lange, F. F. Clarke, D. R. (1982). Morphological changes of an intergranular thin film in a polycrystalline spinel. *Journal of the American Ceramic Society*, *65*(10), 502-506.

Lartigue-Korinek, S., Liagege, S., Kisielowski, C. Serra, A. (2008). Disconnection arrays in a rhombohedral twin in α-alumina. *Philosophical Magazine*, *88*(10), 1569-1579.

Lasaga, A. C. (1979). Multicomponent exchange and diffusion in silicates. *Geochimica et Cosmochimica Acta*, *43*, 455-469.

LeBeau, J. M., Findlay, S. D., Allen, L. J. Stemmer, S. (2008). Quantitative atomic resolution scanning transmission electron microscopy. *Physical Review Letters*, *100*(20), 206101.

Le Claire, A. D. (1951). Grain boundary diffusion in metals. *Philosophical Magazine A*, *42*(328), 468-474.

Le Claire, A. D. (1963). The analysis of grain boundary diffusion measurements. *British Journal of Applied Physics*, *14*(6), 351-356.

Lee, M. R., Bland, P. A. Graham, G. (2003). Preparation of TEM samples by focused ion beam (FIB) techniques; applications to the study of clays and phyllosilicates in meteorites. *Mineralogical Magazine*, *67*(3), 581-592.

Lee, M. R., Brown, D. J., Hodson, M. E., MacKenzie, M. Smith, C. L. (2009). Weathering microenvironments on feldspar surfaces: implications for understanding fluid-mineral reactions in soils. *Mineralogical Magazine*, *72*(6), 1319-1328.

Lee, M. R., Brown, D. J., Smith, C. L., Hodson, M. E., MacKenzie, M. Hellmann, R. (2007). Characterization of mineral surfaces using FIB and TEM: A case study of naturally weathered alkali feldspars. *American Mineralogist*, *92*, 1383-1394.

Lee, S. B., Sigle, W., Kurtz, W. Rühle, M. (2003). Temperature dependence of faceting in $\Sigma 5(310)[001]$ grain boundary of $SrTiO_3$. *Acta Materialia*, *51*(4), 975-981.

Lehovec, K. (1953). Space-charge layer and distribution of lattice defects at the surface of ionic crystals. *The Journal of Chemical Physics*, *21*(7), 1123-1128.

Levine, H. S. MacCallum, C. J. (1960). Grain boundary and lattice diffusion in polycrystalline bodies. *Journal of Applied Physics*, *31*(3), 595-599.

Li, J., Dillon, S. J. Rohrer, G. S. (2009). Relative grain boundary area and energy distributions in nickel. *Acta Materialia*, *57*(14), 4304-4311.

Ljungberg, K., Grey, F. Bengtsson, S. (1997). Formation of directly bonded Si/Si interfaces in ultra-high vacuum. *Applied Surface Science*, *117-118*, 813-819.

Lojkowski, W. Fecht, H.-J. (2000). The structure of intercrystalline interfaces. *Progress in Materials Science*, *45*(5-6), 339-568.

Lozovoi, A. Y., Paxton, A. T. Finnis, M. W. (2006). Structural and chemical embrittlement of grain boundaries by impurities: A general theory and first-principles calculations for copper. *Physical Review B*, *74*, 155416.

Lu, J., Prabhu, M., Song, J., Li, C., Xu, J., Ueda, K. et al. (2000). Optical properties and highly efficient laser oscillation of Nd:YAG ceramics. *Applied Physics B: Lasers and Optics*, *71*(4), 469-473.

Lu, J., Ueda, K.-i., Yagi, H., Yanagitani, T., Akiyama, Y. Kaminskii, A. A. (2002). Neodymium doped yttrium aluminum garnet ($Y_3Al_5O_{12}$) nanocrystalline ceramics–a new generation of solid state laser and optical materials. *Journal of Alloys and Compounds*, *341*(1-2), 220-225.

Lupei, V., Lupei, A., Pavel, N., Taira, T. Ikesue, A. (2001). Comparative investigation of spectroscopic and laser emission characteristics under direct 885-nm pump of concentrated

Nd:YAG ceramics and crystals. *Applied Physics B: Lasers and Optics*, *73*(7), 757-762.

Mah, T.-I., Parthasarathy, T. Leea, H. D. (2004). Polycrystalline YAG; structural or functional? *Journal of Ceramic Processing Research*, *5*(4), 369-379.

Mao, W. (2001). Analysis of misorientation distribution in polycrystalline aluminum sheet by using ODF data. *Materials Science and Engineering A*, *300*(1-2), 80-84.

Marquardt, H., Ganschow, S. Schilling, F. (2009). Thermal diffusivity of natural and synthetic garnet solid solution series. *Physics and Chemistry of Minerals*, *36*(2), 107-118.

Marquardt, K., Petrishcheva, E., Abart, R., Gardés, E., Wirth, R., Dohmen, R. et al. (in Press). Volume diffusion of ytterbium in YAG: thin-film experiments and combined TEM–RBS analysis. *Physics and Chemistry of Minerals*.

Marquardt, K., Petrishcheva, E., Gardés, E., Wirth, R., Abart, R. Heinrich, W. (submitted). Grain boundary and volume diffusion experiments in yttrium aluminium garnet bicrystals at 1723 K: A miniaturized study. *Geochimica et Cosmochimica Acta*.

Maszara, W. P. (1991). Silicon-on-insulator by wafer bonding - a review. *Journal of the Electrochemical Society*, *138*(1), 341-347.

Maszara, W. P., Jiang, B. L., Yamada, A., Rozgonyi, G. A., Baumgart, H. Dekock, A. J. R. (1991). Role of surface-morphology in wafer bonding. *Journal of Applied Physics*, *69*(1), 257-260.

Meissner, E., Sharp, T. G. Chakraborty, S. (1998). Quantitative measurement of short compositional profiles using analytical transmission electron microscopy. *American Mineralogist*, *83*(5-6), 546-552.

Mellenthin, J., Karma, A. Plapp, M. (2008). Phase-field crystal study of grain-boundary premelting. *Physical Review B*, *78*(18), 184110.

Merkle, K. L., Thompson, L. Phillipp, F. (2004). In-situ HREM studies of grain boundary migration. *Interface Science*, *12*, 277-292.

Metsch, P., Spit, F. H. M. Bakker, H. (1986). Computer simulation of simultaneous bulk, grain-boundary, and surface diffusion. *physica status solidi (a)*, *93*(2), 543-547.

Milke, R., Abart, R., Kunze, K., Koch, M., Lier, M., Schmid, D. et al. (2009). Matrix rheology effects on reaction rim growth I: evidence from orthopyroxene rim growth experiments. *Journal of Metamorphic Geology*, *27*, 71-82.

Milke, R., Dohmen, R., Becker, H.-W. Wirth, R. (2007). Growth kinetics of enstatite reaction rims studied on nano-scale, part I: Methodology, microscopic observations and the role of water. *Contributions to Mineralogy and Petrology*, *154*(5), 519-533.

Mishin, Y. Herzig, C. (1995). Diffusion in fine-grained materials: Theoretical aspects and experimental possibilities. *Nanostructured Materials*, *6*(5-8), 859-862.

Mishin, Y. Herzig, C. (1999). Grain boundary diffusion: recent progress and future research.

Materials Science and Engineering: A, *260*(1-2), 55-71.

Mistler, R. E. Coble, R. L. (1974). Grain-boundary diffusion and boundary widths in metals and ceramics. *Journal of Applied Physics*, *45*(4), 1507-1509.

Mitzi, D. B., Lombardo, L. W., Kapitulnik, A., Laderman, S. S. Jacowitz, R. D. (1990). Growth and properties of oxygen- and ion-doped $Bi_2Sr_2CaCu_2O_{8+\delta}$ single crystals. *Physical Review B*, *41*(10), 6564-6574.

Moelans, N., Blanpain, B. Wollants, P. (2008). Quantitative phase-field approach for simulating grain growth in anisotropic systems with arbitrary inclination and misorientation dependence. *Physical Review Letters*, *101*(2), 025502.

Nicholls, A. W. Jones, I. P. (1983). Determination of low temperature volume diffusion coefficients in an Al-Zn alloy. *Journal of Physics and Chemistry of Solids*, *44*(7), 671-676.

Noort, R. van, Spiers, C. Peach, C. (2007). Effects of orientation on the diffusive properties of fluid-filled grain boundaries during pressure solution. *Physics and Chemistry of Minerals*, *34*(2), 95-112.

Okabe, M., Koda, M. Mori, T. (1981). Diffusion species in pipe diffusion for orowan loop climb in a Cu-SiO_2 alloy. *Scripta Metallurgica*, *15*(5), 555-558.

Olgaard, D. L. Fitz Gerald, J. D. (1993). Evolution of pore microstructures during healing of grain boundaries in synthetic calcite rocks. *Contributions to Mineralogy and Petrology*, *115*(2), 138-154.

Overwijk, M. H. F., Heuvel, F. C. van den Bulle-Lieuwma, C. W. T. (1993). Novel scheme for the preparation of transmission electron microscopy specimens with a focused ion beam. *Journal of Vacuum Science and Technology B*, *11*(6), 2021-2024.

Padmanabhan, K. A. Basariya, M. R. (2009). Mesoscopic grain boundary sliding as the rate controlling process for high strain rate superplastic deformation. *Materials Science and Engineering: A*, *527*(1-2), 225-234.

Pavel, N., Lupei, V., Saikawa, J., Taira, T. Kan, H. (2006). Neodymium concentration dependence of 0.94-, 1.06- and 1.34-μm laser emission and of heating effects under 809- and 885-nm diode laser pumping of Nd:YAG. *Applied Physics B: Lasers and Optics*, *82*(4), 599-605.

Pennock, G., Coleman, M., Drury, M. Randle, V. (2009). Grain boundary plane populations in minerals: the example of wet NaCl after low strain deformation. *Contributions to Mineralogy and Petrology*, *158*(1), 53-67.

Pennycook, S. J. (1989). Z-contrast STEM for materials science. *Ultramicroscopy*, *30*(1-2), 58-69.

Peters, M. I. Reimanis, I. E. (2003). Grain boundary grooving studies of yttrium aluminum garnet (YAG) bicrystals. *Journal of the American Ceramic Society*, *86*(5), 870-872.

Phaneuf, M. W. (1999). Applications of focused ion beam microscopy to materials science specimens. *Micron*, *30*(3), 277-288.

Pond, R. C. (1989). Line defects in interfaces. In F. Nabarro (Ed.), *Dislocations in solids* (Vol. 8, p. 1-66). Elsevier, Amsterdam.

Pond, R. C. Vlachavas, D. (1983). Bicrystallography. *Proceedings of the Royal Society of London. Series A, Mathematical and Physical Sciences*, *386*(1790), 95-143.

Pradère, P., Revol, J. F., Nguyen, L. St. John Manley, R. (1988). Lattice imaging of poly-4-methyl-pentene-1 single crystals; use and misuse of fourier averaging techniques. *Ultramicroscopy*, *25*(1), 69-80.

Pradère, P. Thomas, E. L. (1990). Image processing of partially periodic lattice images of polymers: The study of crystal defects. *Ultramicroscopy*, *32*(2), 149-167.

Pössl, A. Kräuter, G. (1999). Wafer direct bonding: tailoring adhesion between brittle materials. *Materials Science and Engineering. Reports*(25), 1-88.

Raj, R., Pavinich, W. Ahlquist, C. N. (1975). On the sintering rate of cleavage cracks. *Acta Metallurgica*, *23*(3), 399-403.

Randle, V. Davies, H. (2002). A comparison between three-dimensional and two-dimensional grain boundary plane analysis. *Ultramicroscopy*, *90*, 153-162.

Randle, V., Hu, Y. Coleman, M. (2008). Grain boundary reorientation in copper. *Journal of Materials Science*, *43*(11), 3782-3791.

Randle, V., Rohrer, G. S. Hu, Y. (2008). Five-parameter grain boundary analysis of a titanium alloy before and after low-temperature annealing. *Scripta Materialia*, *58*(3), 183-186.

Reiche, M. (2006). Semiconductor wafer bonding. *Physica Status Solidi a*, *203*(4), 747-759.

Richter, D. Simmons, G. (1977). Microscopic tubes in igneous rocks. *Earth and Planetary Science Letters*, *34*(1), 1-12.

Rohrer, G. S. (2007). The distribution of grain boundary planes in polycrystals. *JOM*, *59*(9), 38-42.

Rohrer, G. S., El Dasher, B. S., Miller, H. M., Rollett, A. D. Saylor, D. M. (2004). Distribution of grain boundary planes at coincident site lattice misorientations. *Materials Research Society*, *N7.2*.

Sader, K., Schaffer, B., Vaughan, G., Brydson, R., Brown, A. Bleloch, A. (2010). Smart acquisition EELS. *Ultramicroscopy*, *In Press*.

Sato, Y., Mizoguchi, T., Shibata, N., Yamamoto, T., Hirayama, T. Ikuhara, Y. (2009). Atomic-scale segregation behavior of Pr at a ZnO [0001] Σ49 tilt grain boundary. *Physical Review B*, *80*(9), 094114.

Sato, Y., Yamamoto, T. Ikuhara, Y. (2007). Atomic structures and electrical properties of ZnO grain boundaries. *Journal of the American Ceramic Society*, *90*(2), 337-357.

Saylor, D. M., El Dasher, B. S., Rollett, A. D. Rohrer, G. S. (2004). Distribution of grain boundaries in aluminum as a function of five macroscopic parameters. *Acta Materialia*,

52(12), 3649-3655.

Schmid, D. W., Abart, R., Podladchikov, Y. Y. Milke, R. (2009). Matrix rheology effects on reaction rim growth ii: coupled diffusion and creep model. *Journal of Metamorphic Geology*, *27*, 83-91.

Schroer, C. G., Kurapova, O., Patommel, J., Boye, P., Feldkamp, J., Lengeler, B. et al. (2005). Hard x-ray nanoprobe based on refractive x-ray lenses. *Applied Physics Letters*, *87*(12), 124103.

Schuh, C., Kumar, M. King, W. (2005). Universal features of grain boundary networks in FCC materials. *Journal of Materials Science*, *40*(4), 847-852.

Schwarz, S. M., Kempshall, B. W., Giannuzzi, L. A. Stevie, F. A. (2002). Utilizing the SIMS technique in the study of grain boundary diffusion along twist grain boundaries in the Cu(Ni) system. *Acta Materialia*, *50*(20), 5079-5084.

Shan, Z., Stach, E. A., Wiezorek, J. M. K., Knapp, J. A., Follstaedt, D. M. Mao, S. X. (2004). Grain boundary-mediated plasticity in nanocrystalline nickel. *Science*, *305*(5684), 654-657.

Shannon, R. (1976). Revised effective ionic radii and systematic studies of interatomic distances in halides and chalcogenides. *Acta Crystallographica Section A*, *32*, 751-767.

Shirey, S. B., Simmons, G. Padovani, E. R. (1980). Angular, oriented microtubes in metamorphic plagioclase. *Geology*, *8*(5), 240-244.

Siegel, D. J. Hamilton, J. C. (2005). Computational study of carbon segregation and diffusion within a nickel grain boundary. *Acta Materialia*, *53*(1), 87-96.

Smoluchowski, R. (1952). Theory of grain boundary diffusion. *Physical Review*, *87*(3), 482-487.

Sommer, J., Herzig, C., Muschik, T. Gust, W. (1995). Temperature dependence and anisotropy of grain boundary self-diffusion along $\Sigma = 5$ <001> tilt boundaries in Ag. *Acta Metallurgica et Materialia*, *43*(3), 1099-1107.

Song, C. (2009). *Low energy argon ion source for the NCEM FIB.* Conference Presentation.

Spence, J. C. H. (2003). Oxygen in crystals-seeing is believing. *Science*, *299*(5608), 839-841.

Sprunt, E. S. Nur, A. (1979). Microcracking and healing in granites: New evidence from cathodoluminescence. *Science*, *205*(4405), 495-497.

Stöckhert, B. Duyster, J. (1999). Discontinuous grain growth in recrystallised vein quartz – implications for grain boundary structure, grain boundary mobility, crystallographic preferred orientation, and stress history. *Journal of Structural Geology*, *21*(10), 1477-1490.

Sun, C. P. Balluffi, R. W. (1982). Secondary grain boundary dislocations in [001] twist boundaries in MgO: II extrinsic structures. *Philosophical Magazine A*, *46*(1), 63-73.

Surholt, T., Molodov, D. A. Herzig, C. (1998). Orientation dependence of Ge diffusion along symmetrical [111] tilt grain boundaries in Al. *Acta Materialia*, *46*(15), 5345-5355.

Sutton, A. Balluffi, R. W. (1995). *Interfaces in crystalline materials.* Clarendon Press.

Suzuki, A. Mishin, Y. (2005). Atomic mechanisms of grain boundary diffusion: Low versus high temperatures. *Journal of Materials Science*, *40*(12), 3155-3161.

Suzuoka, T. (1961). Lattice and grain boundary diffusion in polycrystals. *Transactions of the Japan Institute of Metals*, *2*, 25-33.

Suzuoka, T. (1964). Exact solutions of two ideal cases in grain boundary diffusion problem and the application to sectioning method. *Journal of the Physical Society of Japan*, *19*, 839.

Takahashi, K., Mizobe, Y., Ando, K. Saito, S. (2006). Effects of frequency on the crack-healing behavior of Si_3N_4/SiC composite under cyclic stress. *JSME International Journal Series A Solid Mechanics and Material Engineering*, *49*(3), 307-313.

Tirone, M., Ganguly, J., Dohmen, R., Langenhorst, F., Hervig, R. Becker, H.-W. (2005). Rare earth diffusion kinetics in garnet: Experimental studies and applications. *Geochimica et Cosmochimica Acta*, *69*(9), 2385-2398.

Tong, Q. Y. Gösele, U. (1999). *Semiconductor wafer bonding: science and technology.* John Wiley, New York.

Tong, Q. Y., Gösele, U., Martini, T. Reiche, M. (1995). Ultrathin single-crystalline silicon on quartz (SOQ) by 150°C wafer bonding. *Sensors and Actuators A*, *48*(2), 117-123.

Tsu, I. F., Wang, J.-L., Kaiser, D. L. Babcock, S. E. (1998). A comparison of grain boundary topography and dislocation network structure in bulk-scale [001] tilt bicrystals of $Bi_2Sr_2CaCu_2O_{8+x}$ and $YBa_2Cu_3O_{7\text{-}d}$. *Physica C: Superconductivity*, *306*(3-4), 163-187.

Turnbull, D. (1951). Theory of grain boundary migration rates. *Journal of Metals*, *3*, 661-5.

Turnbull, D. Hoffman, R. E. (1954). The effect of relative crystal and boundary orientations on grain boundary diffusion rates. *Acta Metallurgica*, *2*(3), 419-426.

Urban, K. W. (2007). The new paradigm of transmission electron microscopy. *MRS Bulletin - Multiscale Modeling in Advanced Materials Research*, *32*(11), 946-952.

Urban, K. W. (2008). Studying atomic structures by aberration-corrected transmission electron microscopy. *Science*, *321*(5888), 506-510.

Valiev, Y. P., Zukov, M., I.M., Z., Timoshevskii, A., Mikhailow, B. Desyatkov, G. (2007). *Grain boundary diffusion and properties of nanostructured materials.* CISP Cambridge International Science Publishing.

Vargas, J. L., Zhang, N., Kaiser, D. L. Babcock, S. E. (1997). Systematic copper concentration variations along grain boundaries in bulk-scale $YBa_2Cu_30_{7\text{-}d}$ bicrystals. *Physica C: Superconductivity*, *292*(1-2), 1-16.

Vonlanthen, P. Grobety, B. (2008). CSL grain boundary distribution in alumina and zirconia ceramics. *Ceramics International*, *34*(6), 1459-1472.

Wanamaker, B. J. Evans, B. (1985). Experimental diffusional crack healing in olivine. In R. N. Schock (Ed.), *Point defects in minerals* (Vol. 31, p. 194-210). American Geophysical Union,

Washington.

Weber, R. Abadie, J. (2001). Processing and optical properties of YAG- and rare-earth-aluminum oxide-composition glass fibers. *Materials Research Society*, *702*, 193-204.

Whipple, R. T. P. (1954). Concentration contours in grain boundary diffusion. *Philosophical Magazine*, *45*(371), 1225-1236.

White, J. C. White, S. H. (1981). On the structure of grain boundaries in tectonites. *Tectonophysics*, *78*(1-4), 613-628.

White, S. (1973). Syntectonic recrystallization and texture development in quartz. *Nature*, *244*(5414), 276-278.

Williams, D. B. Carter, B. C. (Eds.). (1996). *Transmission electron microscopy*. Springer, New York.

Wirth, R. (2004). Focused ion beam (FIB): a novel technology for advanced application of micro- and nanoanalysis in geosciences and applied mineralogy. *European Journal of Mineralogy*, *16*(6), 863-876.

Wolf, D. Yip, S. (Eds.). (1992). *Materials interfaces - atomic-level structure and properties* (1 ed.). Chapman and Hall, Cambridge.

Wuensch, B. J. Tuller, H. L. (1994). Lattice diffusion, grain boundary diffusion and defect structure of ZnO. *Journal of Physics and Chemistry of Solids*, *55*(10), 975-984.

Yin, H., Deng, P. Gan, F. (1998). Defects in YAG:Yb crystals. *Journal of Applied Physics*, *83*(7), 3825-3828.

Young Chul, S., Bum Jun, K., Dong Hoon, K., Young Min, K. Tae Geun, K. (2006). Investigation of Zn diffusion by SIMS and its effects on the performance of AlGaInP-based red lasers. *Semiconductor Science and Technology*, *21*, 35-39.

Appendix

Danksagung

Diese Arbeit wäre ohne die Unterstützung von Freunden, Arbeitskollegen und nicht zuletzt meiner Familie nicht zustande gekommen. Ihnen möchte ich im Folgenden meinen Dank aussprechen. An erster Stelle danke ich den Betreuern meiner Arbeit, Richard Wirth und Wilhelm Heinrich, die diese Arbeit stetig unterstützten und für Fragen jederzeit bereit standen. Beide haben Tagungs- und Fortbildungsvorhaben immer bestens unterstützt. Darüber hinaus bin ich Wilhelm Heinrich für seinen Einsatz meine Stelle zu beantragen und zu verlängern zu großem Dank verpflichtet. Richard Wirth danke ich für sein Vertrauen, mich allein das TEM bedienen zu lassen und für vielerlei Hilfe und Ratschläge. Ihr Einverständnis, dass ich sowohl meine Kinder zur Arbeit mitbringen, als auch daheim arbeiten zu dürfen, ermöglichte es, die Arbeit in diesem Zeitrahmen anzufertigen. Vielen Dank für diese Offenheit und Toleranz! Georg Dresen danke ich für das Bereitstellen der 'Bikristall-Synthese-Ausrüstung' und das Ermöglichen der kurzfristigen Exkursionen an die Ruhr-Universität Bochum zur Dünnfilmerstellung. Stefan Heinemann gilt mein Dank für die fortwährende Bereitschaft, mir Fragen zur Bikristall-Synthese zu beantworten. Christian Schroer, Pit Boye, Sandra Stephan sowie dem gesamten Dresdener Team danke ich für die Einblicke in ihre Arbeit am ESRF in Grenoble und für die Messungen meiner Probe. Des Weiteren danke ich Beate Hein für ihre immerwährende Unterstützung, Anja Schreiber für die Präparation von TEM-Lamellen mit der FIB. Für die Unterstützung bei der Durchführung der Heizexperimente bin ich Reiner Schulz und Max Wilke zu Dank verpflichtet. Gerhard Berger danke ich für die Durchführung ausgefallener Probenpräparationswünsche. Danke auch an die Sektion 3.3, das nette Kollegium sorgt für Freude an Diskussionen. Die Manuskripte konnten durch das Mitwirken aller Koautoren und durch hilfreiche Gutachten der Editoren und Rezensenten der Zeitschrift *Physics and Chemistry of Minerals* verbessert werden. Gar nicht genug kann ich meiner Familie (Hauke, Kaspar und Rasmus), sowie meinen Eltern und Geschwistern danken. Saskia und Friedel bewegten mich in schweren Phasen dazu, durchzuhalten. Ihnen und Anka, Willi, Hanna, Mara, Neli und Peter danke ich für die vielen Stunden die sie mit Kaspar und Rasmus verbracht haben! Tausend Dank, liebster Hauke, für all die Stunden, die wir abendlich über

Rechnungen, deren Umsetzungen, Programme, Resultate, Implikationen - und so könnte es ewig fortgehen... - diskutierten. Finanziell wurde meine Arbeit am NCEM in Berkeley von der DFG unterstützt, die Präsentation der Arbeit auf der IMC in Aachen wurde unter anderem durch eine Reisekostenbeihilfe der *American Microscopy Society* unterstützt. Vielmals danke ich Christiane Nüsslein-Volhard für das Erschaffen der CNV-Stiftung. Ihre monatliche finanzielle Unterstützung ermöglichte mir, neben Hilfe im Haushalt, vor allem den Forschungsaufenthalt in Berkeley durch das Engagieren einer privaten Nanny sehr effektiv zu gestalten.

Angaben zum Eigenanteil

Diese Arbeit wäre ohne die Unterstützung Dritter so nicht möglich gewesen. Dennoch ist sie eigenständig durchgeführt, geplant und organisiert worden. Schon die Idee des Promotionsthemas stammte in Anlehnung an einen nicht verwirklichten DFG-Antrag (Urheber Prof. Wilhelm Heinrich, Prof. Georg Dresen und Dr. Richard Wirth) von mir. Gemeinsam mit Prof. Wilhelm Heinrich plante ich, die Untersuchung synthetischer Korngrenzen mit Diffusionsexperimenten zu kombinieren. Ich schlug YAG als Material für die Experimente vor. Planung und Umsetzung der Experimente erfolgten eigenständig, wobei ich jedoch wiederholt die Diskussion mit Prof. Wilhelm Heinrich und Dr. Richard Wirth suchte. Auch den Kontakt zu den Kooperationspartnern baute ich auf. Ebenso wandte ich mich bei spezifischen Fragestellungen an Personen mit Expertisen zum jeweiligen Problem.

Die meisten TEM-Folien, die ich während der Doktorandenzeit am GFZ untersuchte, habe ich an der Focussed Ion Beam Maschine präpariert; als Anja Schreiber angestellt wurde übernahm Sie die Routinepräparation. Zwei Proben wurden extern angefertigt (FEI, ZEISS).

Die gesamten Messungen am TEM entstanden unter initialer Einweisung durch Dr. Richard Wirth, der auch im Weiteren immer für Fragen zur Verfügung stand.

Es folgen Angaben zu den vier Publikationen, die aus meiner Arbeit hervorgegangen sind:

Kapitel 3.1: Planung und Durchführung der 'Bonding-Experimente' gestaltete ich. Dr. Stefan Heinemann stand mir telefonisch für Fragen zur Verfügung. Idee und Ausarbeitung des Manuskripts für die Publikation in PCM erfolgte in Einzelarbeit. Sowohl Dr. Richard Wirth als auch Prof. Wilhelm Heinrich machten Vorschläge zum Aufbau und zur Struktur, die den Inhalt jedoch nicht betrafen.

Kapitel 3.2: Die Planung und Durchführung der Experimente für das zweite Manuskript übernahm ich ebenfalls. In Bochum wurde ich von Dr. Ralf Dohmen in die Nutzung der 'Pulsed Laser Deposition' Maschine eingewiesen. Ebenso ermöglichte er mir einen kleinen Einblick in die Grundlagen der Diffusion (Literaturhinweise etc.). Bei der Umsetzung der Auswertungsroutine half mir Dr. Emmanuel Gardés, indem er mir den Einstieg in die Verwendung von Matlab ermöglichte. Fragen zur Fehler-

fortpflanzung und zur Cliff-Lorimer-Korrektur beantworteten mir Dr. Richard Wirth und Dr. Sandro Jahn. Bei der Wiederinbetriebnahme des vertikalen Gasmischofen und dessen Kalibrierung stand mir Dr. Max Wilke zur Seite.

Nach ausführlicher Diskussion der Beobachtungen mit Prof. Rainer Abart und Dr. Elena Petrishcheva, entwickelte ich zusammen mit Dr. Elena Petrishcheva ein numerisches Model, welches die Eigenschaftsänderungen in der Diffusionsquelle berücksichtig. Das Manuskript entwarf ich, der Teil der das numerische Modell betrifft entstand in enger Zusammenarbeit mit Dr. Elena Petrishcheva. Die verschiedenen Koautoren hatten sehr unterschiedliche Vorstellungen von Formulierung, Aufbau und Länge der Ausführungen – diese zur Zufriedenheit aller zu kombinieren war eine Herausforderung.

Kapitel 3.3: Planung und Experimente führte ich durch. Durch die Optimierung des Messverfahrens minimierte ich unerwünschte Nebeneffekte, die die Messungen negativ beeinflussen könnten. Dr. Elena Petrishcheva und ich erweiterten das numerische Model, so dass es auf Korngrenzdiffusion angewandt werden konnte. Wir probierten gemeinsam verschiedene Lösungsansätze aus und feilten an den Parametern für das zweidimensionale Modell. Alle Koautoren bekamen das von mir angefertigte Manuskript. Ich erhielt nur wenige Änderungsvorschläge; die konstruktive Kritik von Dr. Emmanuel Gardés und Prof. Wilhelm Heinrich ermöglichten es, den Aufbau der Einleitung und der Diskussion deutlich zu verbessern.

Kapitel 3.4: Die Idee die Proben auf atomarer Ebene zu untersuchen, stammt von mir. Ich bewarb mich in Eigeninitiative um einen Kooperationsaufenthalt am National Center for Electron Microscopy (NCEM) in Berkeley, Kalifornien. Nachdem mein Kooperationsvorschlag durch Gutachter am dortigen Institut befürwortet worden war, bewarb ich mich um finanzielle Unterstützung durch die Deutsche Forschungsgemeinschaft (DFG). Da es Doktoranden verwehrt ist, sich um derartige Unterstützung zu bewerben, reichte Prof. Wilhelm Heinrich den Antrag für mich ein. Während des sechsmonatigen Aufenthaltes in Berkeley arbeitete ich mit Dr. Christian Kisielowski und Dr. Quentin Ramasse zusammen. Dr. Christian Kisielowski erklärte mir das Prinzip und die Durchführung der 'exit wave reconstruction' sowie der Bildsimulation. Am TEAM0.5 Mikroskop half mir ChengYu Song. Dr.

Quentin Ramasse und ich führten die STEM-Messungen am VG gemeinsam durch. Für die Datenauswertung erklärte er mir die Routinen und erläuterte mir die Software. Die EELS-Messungen entstanden am GFZ in Zusammenarbeit mit Dr. Wirth. Idee und Manuskript stammen von mir, die Koautoren kommentierten lediglich die Formulierungen. Der Aufbau des Manuskripts, die Auswertung der Daten, die wissenschaftlichen Implikationen der Ergebnisse stammen von mir.

Ich verfasste die Antwortbriefe auf die Kommentare der Rezensenten und Editoren für alle akzeptierten Publikationen. Für die Präsentation von Ergebnissen auf Tagungen (IMC 2008 in Aachen (Dreiländertagung)) beantragte ich erfolgreich Reisekostenzuschüsse der *American Microscopy Society*. Diesen Reisekostenzuschuss beantragte ich auch für die IMC 17 2010 in Rio de Janeiro erfolgreich, auch die Ergänzung durch einen Reisekostenzuschuss der *Deutschen Gesellschaft für Elektronenmikroskopie* wurde mir zugesagt. Des Weiteren bewarb ich mich eigenständig und erfolgreich um ein Stipendium der *Christiane-Nüsslein-Volhard-Stiftung*.

Curriculum vitae

Katharina Marquardt

Aus Datenschutzgründen wurde der Lebenslauf in der digitalen Version dieser Arbeit gelöscht.

Aus Datenschutzgründen wurde der Lebenslauf in der digitalen Version dieser Arbeit gelöscht.

Aus Datenschutzgründen wurde der Lebenslauf in der digitalen Version dieser Arbeit gelöscht.

Aus Datenschutzgründen wurde der Lebenslauf in der digitalen Version dieser Arbeit gelöscht.

Aus Datenschutzgründen wurde der Lebenslauf in der digitalen Version dieser Arbeit gelöscht.

Aus Datenschutzgründen wurde der Lebenslauf in der digitalen Version dieser Arbeit gelöscht.

Eidesstattliche Erklärung

Hiermit versichere ich, Katharina Marquardt (geb. Hartmann), die vorliegende Arbeit ohne unzulässige Hilfe Dritter und ohne Benutzung anderer, als der angegebenen Hilfsmittel, angefertigt zu haben. Die Stellen der Arbeit, die anderen Werken wörtlich oder inhaltlich entnommen sind, wurden durch entsprechende Quellenangabe kenntlich gemacht.

Diese Arbeit hat in gleicher oder ähnlicher Form noch keiner Prüfungsbehörde vorgelegen.